Magnetic Investigations of Thin Films of Oxides

by

Ahmad Mohammad A Saeedi

Thesis

Submitted to the University of Sheffield for the degree of

Doctor of Philosophy

Department of Physics and Astronomy

September 2019

To the kindest and most supportive figure in my life; my mother, *Seham Bashmakh*

To my father who motivated me along this journey, *Mohammad Saeedi*

To my loving wife who is supporting me during my hardest time, *Ghaida Mukhles*

To my two little boys *Abdulmalik* and *Faris*

To my brothers and my sister who have been waiting for me to complete my PhD successfully,

I devote this thesis to you.

Preface

This thesis in its entirety has been submitted to the University of Sheffield for the fulfilment of the degree of Doctor of Philosophy. The research was performed during the period from 2014 to 2019 with Professor Gillian Gehring as the first advisor and Professor Mark Fox as a second advisor in the Department of Physics and Astronomy. My original research, along with the results, is described in this thesis accompanied by the work of our collaborators from around the world.

The samples of O-polar and Zn-polar ZnO films were made by our collaborators Dr Zengxia Mei and Prof Xiaolong Du at the Beijing National Laboratory for Condensed Matter Physics, Institute of Physics, Chinese Academy of Sciences. Another set of samples were produced from commercial polar ZnO single wafers purchased from Hefei Kejing Materials Technology Co. Ltd. High-quality krypton ions were then inserted in the ZnO films and wafers using the ion implantation method by our collaborator Dr Minju Ying at the College of Nuclear Science and Technology, Beijing Normal University, Beijing, China.

Some of the samples of pure ZnO films were grown using PLD by our collaborator Dr Marzook Alshammari at the National centre for Laser and Optoelectronic, King Abdulaziz City for Science and Technology, KACST, Riyadh, Saudi Arabia. The implantation of Co and Eu in ZnO films were performed by our collaborator Dr Nianhua Peng at Surrey Ion Beam Centre, Surrey University, Surrey UK. EXAFS measurements and analysation were taken by Dr Steve Heald from Advanced Photon Source, Argonne National Laboratory, Argonne, IL, USA. Most of the XRD, Raman spectroscopy measurements, and all the magnetic and magneto-optical measurements of the thin films were taken by myself at the University of Sheffield.

Part of the research in this thesis has already been published recently in 2019 in several scientific journals [1,2]. I hereby certify that this work has not been submitted to any other university or institution for any degree.

Ahmad M.A. Saeedi
Hicks Building, Sheffield

Acknowledgements

I would like to especially thank my first supervisor Professor Gillian Gehring, for her guidance, support, useful discussions, and kindness throughout my 4 years of study. It was an honour to be the last experimental student and to complete my PhD under her supervision. I would also like to take this opportunity to acknowledge my second supervisor, Professor Mark Fox, for his helpful suggestions and comments during my study. I am grateful to Dr Harry Blythe for his expert assistance and valuable suggestions during the experimental works undertaken in the lab. My sincere thanks go to Dr Lisa Hollands who is the Quarrell Laboratory team leader in The Materials Science and Engineering Department at The University of Sheffield, for allowing me to use the facilities there for the some of the annealing processes.

I would like to acknowledge my financial sponsor Umm Al-Qura University and the Saudi Arabia Cultural Bureau in London who have supported me financially and funded the entire duration of my study at the University of Sheffield. Thanks to all the previous members of the magnetic oxide group in The University of Sheffield; Dr Hassan Albargi, Dr Wala Dizayee, Dr Aliaa Zaki, Dr Fatma Gerriu for their help and support. Many thanks to Mr William Fall and Dr Khaled Alhazmi for their support and kindness during the most difficult time of life when I was in chemotherapy. For their encouragement and support provided for the duration of my PhD studies, I thank our academic, administrative and technical staff.

Finally, my sincere appreciation goes to my parents, wife, children, brothers and sister, and friends for all prayers, trust, love, and support over the years and particularly during my PhD study.

Abstract

This thesis describes ZnO thin films that were doped with a variety of dopants including transition metals (TMs) and rare earth elements (RE) but also non TM-dopants. These so-called d^0 magnetic materials were investigated because they are promising emerging candidates for the development of spintronics. The aim was to enhance and investigate the origin of ferromagnetism in these materials by analysing and studying the structure, magnetic and magneto-optic properties.

The large magnetisation produced by the implantation of Krypton ions in ZnO is found to be dependent on the polarity of ZnO films. This result was obtained after evaluating the Kr implantation into different systems, O and Zn polar thin films and a ZnO wafer. Raman scattering was used to evaluate the crystalline damaged due to implantation and distinguish the scattering from amorphous regions in grain boundaries and the scattering from point defects. The effects on the structure and the magnetic properties of Co and Eu implanted ZnO thin films, made by pulsed laser deposition (PLD), are experimentally investigated. The large magnetisation was found to arise due to defects after implantation. However, the defects were recovered after annealing the films at 600° C in air, and another type of magnetisation was observed, where no clusters or any related oxide phases have been detected.

The structural and magnetic properties of Co-doped ZnO thin films, made by PLD, with either metallic Co, CoO or Co_3O_4 precursors have been investigated. These films were made at base pressure 2×10^{-5} Torr, and further higher oxygen pressures of 1×10^{-4} Torr, 1×10^{-3} Torr, 1×10^{-2} Torr, and 1×10^{-1} Torr. There were certain features of the films for which, films made from the metallic Co target, behave quite differently to those made from CoO and Co_3O_4 targets.

Publications

- Minju Ying, **Ahmad M. A. Saeedi**, Miaomiao Yuan, Xia Zhang, Bin Liao, Xu Zhang, Zengxia Mei, Xiaolong Du, Steve M. Heald, A. Mark Fox and Gillian A. Gehring " Extremely large d^0 magnetism in Krypton implanted polar ZnO films", *Journal of Materials Chemistry C* **7**, 1138 (January 2019)[1].
- Hasan Al-bargi, Marzook Alshammari, Kadi Y Museery, Fung-Xian Jiang, **Ahmad M.A. Saeedi**, Mark Fox, Steve M. Heald, Gillian Gehring "Relevance of the preparation of the target for PLD on the magnetic properties of films of iron-doped indium oxide", *Coatings* 2019, *9*, 381. (June 2019)[3]
- Miaomiao Yuan , Xia Zhang , **Ahmad M.A. Saeedi** , Wei Cheng, Chungang Guo, Bin Liao, Xu Zhang, Minju Ying, Gillian A. Gehring "Study of the radiation damage caused by ion implantation in ZnO and its relation to magnetism", *Nuclear Inst. and Methods in Physics Research*, B 455 (2019) 7-12 (June 2019)[2]
- **Ahmad M.A. Saeedi,** Fatma M. Gerriu, Minju Ying, Marzook S. Alshammari, Steve M. Heald, Xiaoli Li, Harry J. Blythe, Mark Fox Gillian A. Gehring "Competing magnetic effects due to the incorporation of oxygen in thin films of (ZnCo)O" *RSC Advances*, 2019, **9**, 38001 – 38010 (November 2019).
- **Ahmad M.A. Saeedi,** Nianhua Peng, Yutaka Adachi, Steve M. Heald, Amal F. Alanazi, Marzook S. Alshammari and Gillian A. Gehring "Magnetism of Co and Eu implanted into ZnO". *Applied Surface Science*, submitted (November 2019).

Conferences and Workshops

- IOP Magnetism 2015, University of Leeds, Leeds, UK (March 2015)

- IOP postgraduate magnetism techniques workshop, University of York, York, UK (December 2015).

- **Ahmad Saeedi**, Harry Blyth, A. Mark Fox and Gillian A. Gehring *"Pulsed laser deposition growth of zinc oxide films for Magnetic Materials*"**,** IOP Magnetism 2016, University of Sheffield, Sheffield, UK (April 2016)

- **Ahmad Saeedi**, Minju Ying, Tao Duan, Miaomiao Yuan, A. Mark Fox and Gillian A. Gehring "*Magnetic properties of Krypton and Argon implanted ZnO films prepared by molecular beam epitaxy*", IOP Magnetism 2017, University of York, York, UK (April 2017).

- Poster I**: Ahmad Saeedi**, Minju Ying, Tao Duan, Miaomiao Yuan, Steve Heald, A. Mark Fox and Gillian A. Gehring "*Krypton doped polar ZnO films by ion implantation gives enormous magnetisation*".
  Poster II**: Ahmad Saeedi**, Nianhua Peng, Marzooq Alshammari, Steve Heald, A. Mark Fox and Gillian A. Gehring "*Investigation of magnetic properties for both Cobalt and Europium implanted ZnO films prepared by pulsed laser deposition".* IOP Magnetism 2018, University of Manchester, Manchester, UK (April 2018).

- Poster I**: Ahmad Saeedi**, Nianhua Peng, Marzook Alshammari, Steve M. Heald, Yutaka Adachi, A. Mark Fox and Gillian A. Gehring "*Effect of annealing on structural and magnetic properties for both Co and Eu implanted ZnO films".*
  Poster II: **Ahmad Saeedi**, Steve M. Heald, A. Mark Fox and Gillian A. Gehring **"***The dependence of the magnetic properties of ZnCoO on the target preparation***"** IOP Magnetism 2019, University of Leeds, Leeds, UK (April 2019).

Permission letters 1

Steve M. Heald
Spectroscopy Group Leader

X-ray Science Division
Advanced Photon Source
Argonne National Laboratory
9700 South Cass Avenue, Bldg. 435E
Argonne, IL 60439

1-630-252-9795 phone
1-630-252-0580 fax
1-630-456-1742 mobile
heald@aps.anl.gov

June 7, 2019

To whom it may concern,

I am pleased to grant permission to Ahmad Mohammad A. Saeedi to use all the data and figures related to X-Ray Absorption Fine Structure (XAFS), X-Ray Near Edge Structure (XANES) and Extended X-Ray Absorption Fine Structure (EXAFS) in his thesis. The figures are 4.12, 5.4, 5.5, 6.7, and 6.8.

Sincerely yours,

Steve Heald

Steve Heald

Permission letter 2

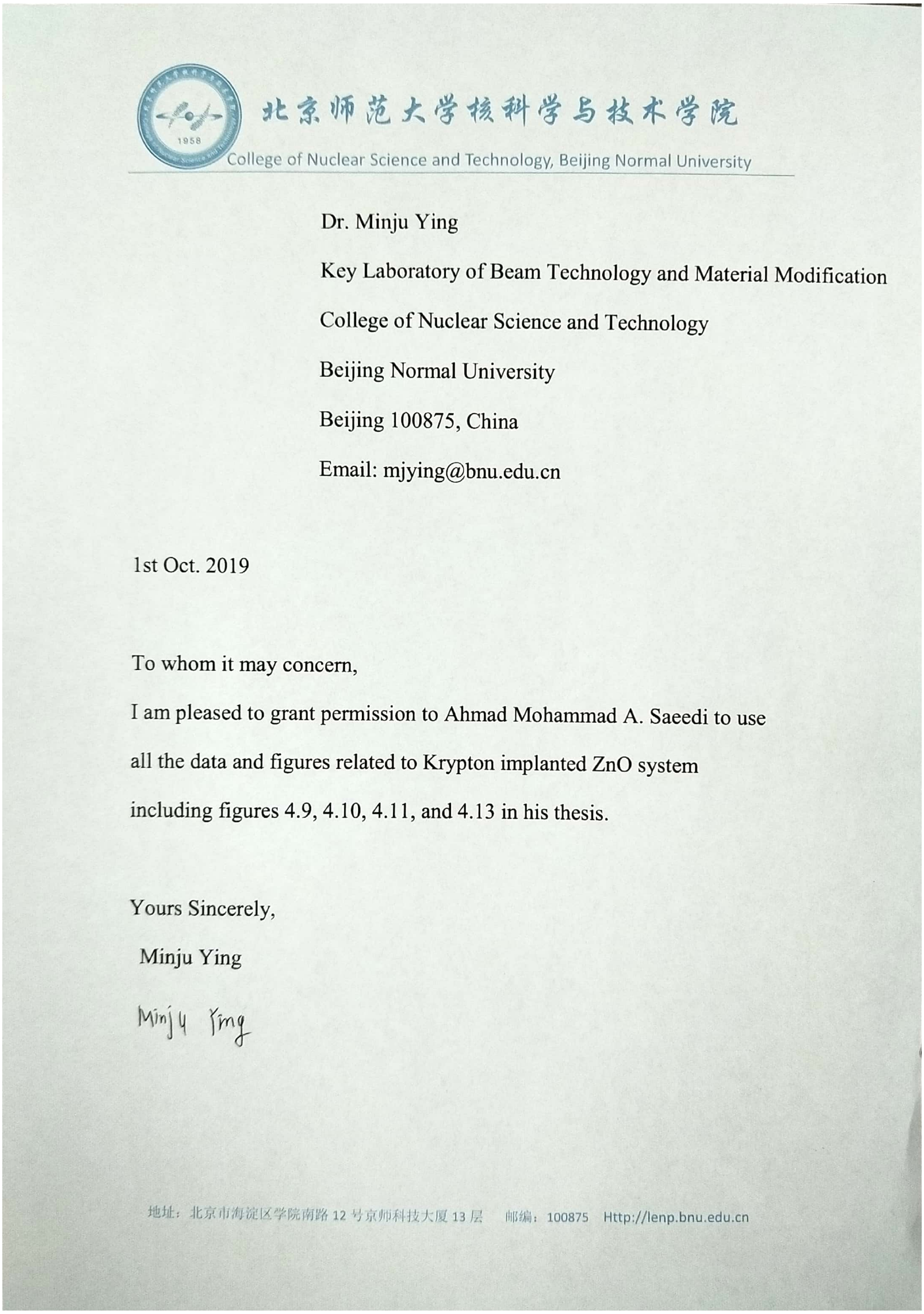

北京师范大学核科学与技术学院
College of Nuclear Science and Technology, Beijing Normal University

Dr. Minju Ying
Key Laboratory of Beam Technology and Material Modification
College of Nuclear Science and Technology
Beijing Normal University
Beijing 100875, China
Email: mjying@bnu.edu.cn

1st Oct. 2019

To whom it may concern,

I am pleased to grant permission to Ahmad Mohammad A. Saeedi to use all the data and figures related to Krypton implanted ZnO system including figures 4.9, 4.10, 4.11, and 4.13 in his thesis.

Yours Sincerely,
Minju Ying
Minju Ying

地址：北京市海淀区学院南路 12 号京师科技大厦 13 层 邮编：100875 Http://lenp.bnu.edu.cn

Permission letter 3

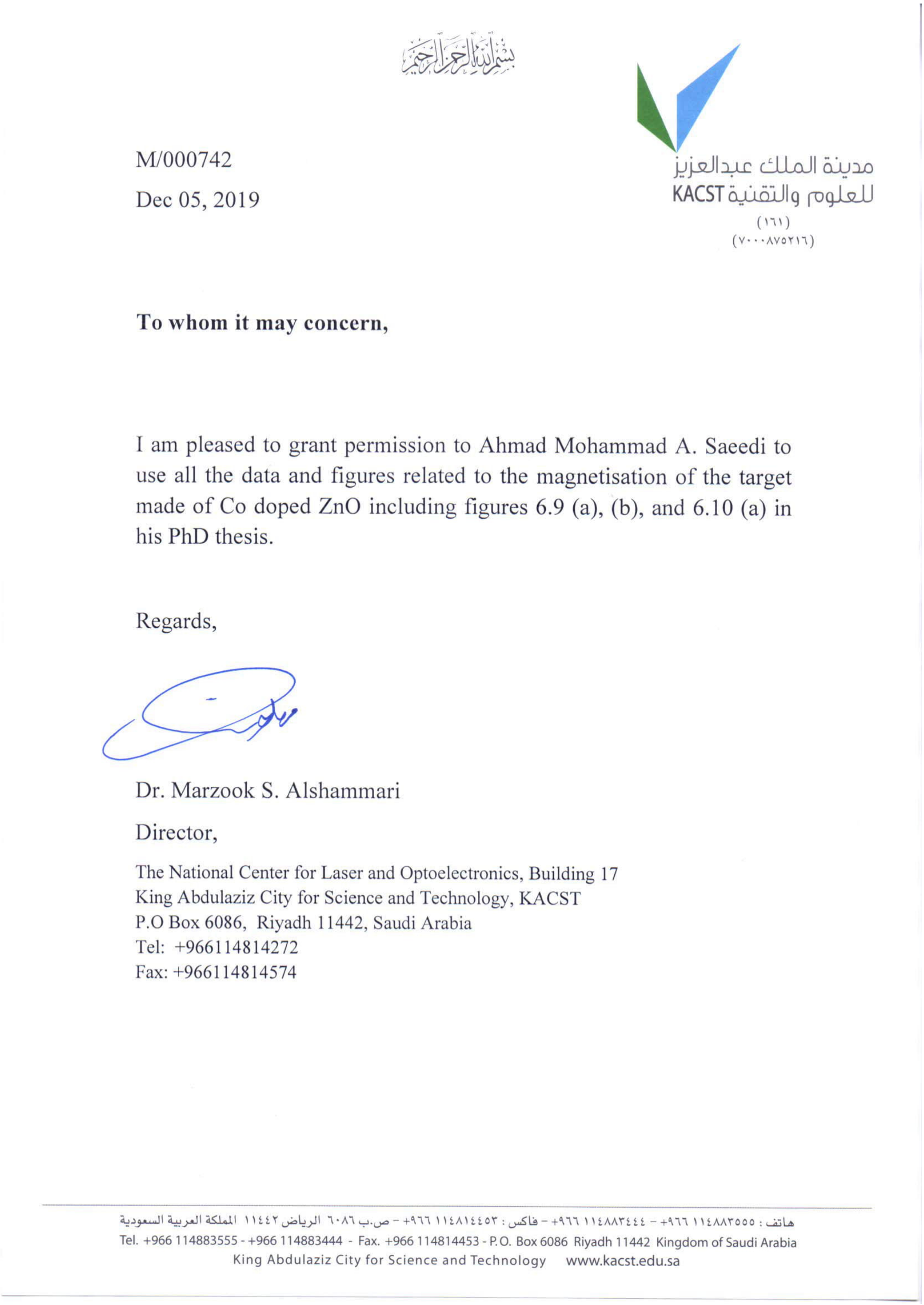

بسم الله الرحمن الرحيم

مدينة الملك عبدالعزيز
للعلوم والتقنية KACST
(١٦١)
(٧٠٠٠٨٧٥٢١٦)

M/000742
Dec 05, 2019

To whom it may concern,

I am pleased to grant permission to Ahmad Mohammad A. Saeedi to use all the data and figures related to the magnetisation of the target made of Co doped ZnO including figures 6.9 (a), (b), and 6.10 (a) in his PhD thesis.

Regards,

Dr. Marzook S. Alshammari

Director,

The National Center for Laser and Optoelectronics, Building 17
King Abdulaziz City for Science and Technology, KACST
P.O Box 6086, Riyadh 11442, Saudi Arabia
Tel: +966114814272
Fax: +966114814574

هاتف : ١١٤٨٨٣٥٥٥ +٩٦٦ - ١١٤٨٨٣٤٤٤ +٩٦٦ - فاكس : ١١٤٨١٤٤٥٣ +٩٦٦ - ص.ب ٦٠٨٦ الرياض ١١٤٤٢ المملكة العربية السعودية
Tel. +966 114883555 - +966 114883444 - Fax. +966 114814453 - P.O. Box 6086 Riyadh 11442 Kingdom of Saudi Arabia
King Abdulaziz City for Science and Technology www.kacst.edu.sa

Table of contents

List of Abbreviations, Symbols and Physical Constants

Abbreviations

AFM	Antiferromagnetic
CB	Conduction Band
CBM	Conduction Band Minimum
CVD	Chemical Vapour Deposition
DC	Direct Current
Dektak	Profilometer for thin film thickness measurements
DMS	Dilute magnetic semiconductors
EXAFS	Extended X-ray Absorption Fine Structure
FM	Ferromagnetic
FR	Faraday rotation
FWHM	Full width at half maximum
GB	Grain boundaries
KAUST	King Abdullah University of Science and Technology
M	Magnetisation
MBE	Molecular Beam Epitaxy
MCD	Magnetic Circular Dichroism
PEM	Photoelastic modulator
PDOS	Phonon density of states
PLD	Pulsed Laser Deposition
PDR	Phonon dispersion relation
PM	Paramagnetic
PMT	Photomultiplier tube detector
RE	Rare-earth elements

RF	Radio Frequency
RKKY	Ruderman-Kittel-Kasuya-Yosida interaction
RT	Room temperature
RTFM	Room temperature ferromagnetism
SQUID	Superconducting Quantum Interference Device
SRIM	Stopping and Range of Ions in Matter
TM	Transition metal
TMs	Transition metals
TMO	Transition metal oxides
TMP	Turbo-molecular pump
UHV	Ultra-high vacuum
XAFS	X-ray Absorption Fine Structure
XANES	X-ray Absorption Near Edge Structure
XRD	X-ray Diffraction
VBM	Valance Band Maximum
ZFC/FC	Zero-field-cooled and field-cooled

Symbols

I	Electric current
ω	Angular velocity
r	Radius
$\boldsymbol{\mu}$	Magnetic moment
A	Area
$\boldsymbol{J}$	Total angular momentum
$\boldsymbol{L}$	Orbital angular momentum
$\boldsymbol{S}$	Spin angular momentum
m	Electron mass
g	Landé g-factor
C	Curie constant
$\boldsymbol{B}$	Magnetic induction
$\boldsymbol{H}$	Magnetic field
$H\mathrm{c}$	Coercive field

$M\mathrm{r}$	Remnant Magnetisation
$M\mathrm{s}$	Magnetisation saturation
Oe	Oersted
P_{eff}^{2}	Effective magnetic moment
P_{O_2}	Oxygen partial pressure
T_C	Curie temperature
T_N	Néel temperature
χ	Magnetic susceptibility
μ	Magnetic permeability
K	Magnetic anisotropy
V	Particle volume
T_B	Blocking temperature
R	Reflection coefficient
ρ	The density
T	Transmission coefficient
α	Absorption coefficient
E_g	Band gap
XeCl	Excimer laser

Physical Constants

c	Velocity of light in free space (2.998×10^{8} m s^{-1})
e	Electronic charge (1.6022×10^{-19} C)
h	Planck's constant (6.63×10^{-34} J s)
$\hbar$	Reduced Planck's constant (1.05×10^{-34} J s)
k_B	Boltzmann constant (1.38×10^{-23} J K^{-1})
N_A	Avogadro’s number (6.022×10^{23} mol^{-1})
μ_B	Bohr magneton (9.27×10^{-24} J T^{-1})
Φ_0	Magnetic quantum flux (2.06×10^{-15} T m^{-2})
μ_0	Magnetic permeability of free space ($4\pi \times 10^{-7}$ H m^{-1})

This page intentionally left blank

Chapter 1 **Introduction and Thesis Overview**

1.1 Introduction

Conventional electronic devices rely strictly on the transport of electrical charge to carry information. It is possible however, not only to make use of the electronic charge, but also the spin of the charge carriers themselves. This new class of processes is known as spintronics or magneto-electronics. There is the potential then, for new technologies and a new class of devices [4-7], with reduced size, increased data-processing speed, and more efficient power consumption [6,8,9].

For this purpose, there is increasing interest in the development of these ‘spin utilising’ materials, called diluted magnetic semiconductors (DMS) [6,10,11]. These semiconductor materials exhibit ferromagnetism (FM), upon doping with a small quantity of transition metals (TM) [12]. One of the major criteria to be considered when choosing materials for use as DMSs is that they should be ferromagnetic at room temperature; in order to exploit spin polarisation in practical electronic devices. Thus, a variety of DMS candidates are being developed and studied widely with the aim of obtaining materials that demonstrate room temperature ferromagnetism (RTFM).

Many researchers have reported that the introduction of magnetic ions from TM, such as Fe, Co, or Mn, in ZnO results in RTFM [6,11,13-16]. This RTFM was initially attributed to the substitutional TM atoms in the Zn lattice sites. These experimental studies attempt to understand the effects of a variety of different parameters, such as various growth techniques and conditions, TM dopants, compositional variations and post-annealing treatments.

However, the results achieved are often contrasting and are not reproducible across different research groups. It appears that most of the difficulties arise when determining if the material ultimately produced is a real DMS, where TM atoms stochastically substitute cations on lattice sites, or if the ferromagnetism found actually results from secondary phases. The semiconductor community is yet to achieve a universally well understood picture of the actual mechanism of ferromagnetic ordering in DMS and it remains controversial to this day.

X-ray magnetic circular dichroism (XMCD) measurements of the Co-doped ZnO sample reveal no detection of the ferromagnetic moment arising from the Co dopants [17,18]. The result has shown that all substitutional Co ions are paramagnetic with no sign of metallic Co and, therefore, it is implied that the observed FM is due to native defects created in the material such as oxygen vacancies[19] or Zn vacancies [20]. It was noticed that RTFM could be observed in undoped ZnO [21,22] or even with non TM-doped ZnO [23] samples due to defects. Others, like Straumal *et al* [24] suggested that the observed RTFM in ZnO is due to the grain boundaries [24-26]. These results have led to a special class of DMS materials, which exhibit what is referred to as d^0 ferromagnetism because they do not contain any transition metal ions. This d^0 ferromagnetism can be developed by suitable control of defects that can avoid the problems of phase segregation and clustering encountered in conventional magnetically doped semiconductors.

Two models can describe the intrinsic nature of ferromagnetism in DMS. First, Dietl *et al* predicted a model in which the ferromagnetic ordering is mediated through spin-polarised charge carriers in order to achieve RTFM in Mn-doped ZnO p-type semiconductors [27]. On the other hand, the majority of experimental studies thus far show that doped ZnO was n-type (electron as carriers). A different theoretical model of ferromagnetism in DMS materials was predicted by Coey *et al* [28]. The proposal was based on a spin-split donor impurity band where the defect states of the material cause ferromagnetism. The defects of ZnO can originate from the overlapping of the electronic states originating from a large number of oxygen vacancies or Zn interstitials, leading to an impurity band. The ferromagnetism occurs when the impurity band interacts with the electrons in the d-levels of the magnetic dopant.

ZnO has drawn large attention, because of its outstanding optical properties, and its potential for use in spintronic materials [29]. ZnO has a wide direct band gap ~3.4 eV as well as a large excitation binding energy so that it can operate at high power and high temperature. This renewed interest in ZnO and its potential use in spintronics motivates the work in this thesis and it is the main semiconducting oxide material focused on throughout. Specifically, the primary subject of this thesis is to investigate the structural and magnetic properties of ZnO thin films that are doped with different dopants and grown using different methods. The aim is to understand the origin of the magnetism in oxides and to understand the role of the defects in causing the magnetism.

1.2 Thesis Overview

This thesis has been divided into seven chapters: **Chapter One** contains a description of the thesis introduction so that the reader can have a general overview of the research area.

Chapter Two includes a discussion of the important basic principles of the magnetism, such as the Pauli exclusion principle and Hund’s rules. It also includes a brief explanation of the different types of magnetic materials such as diamagnetic, paramagnetic, ferromagnetic, antiferromagnetic and ferrimagnetic. Finally, several kinds of exchange interactions, band magnetism and the useful properties of ZnO for DMS are discussed briefly.

Chapter Three contains the experimental techniques that were used in this thesis along with a brief discussion of each method. PLD was used to make our pure ZnO thin films, a Dektak surface profiler was used to measure the thin film thickness and a SQUID magnetometer was used to measure the magnetic properties. XRD, Raman Spectroscopy, XANES, and EXAFS were also used to study the structural properties. MCD was used to measure the magneto-optics properties of the films.

Chapter Four includes a report of the studies associated with the recent interest in the observed RTFM in doped and undoped ZnO. This chapter focuses on d^0 magnetism which is due to defects. Large RTFM was observed in ZnO thin films implanted with Krypton (Kr). Since Kr is an inert element, the magnetisation must arise due to the radiation damage generated during the implantation process and any distortion around the Kr ion. The effect of the dopant concentration in Kr implanted ZnO, along with the type of the polarity of the film of ZnO, is discussed with reference to structural and magnetic properties. The value of RTFM was extremely large in comparison to previous works of As implanted ZnO [30].

Chapter Five contains an experimental investigation of the structure and magnetic properties in 4% of mono Co, Eu, and codoped CoEu implanted ZnO thin films made by PLD. In addition, the effects of both post annealing temperature and environments on the structural and magnetic properties of ZnCoO, ZnEuO, ZnCoEuO films have been investigated in detail.

Chapter Six includes an investigation of the dependence of the structural and magnetic properties of Co-doped ZnO thin films on the target preparation. The films were grown from three different targets containing ZnO with 5% of either metallic Co, CoO, or Co_3O_4 as the precursor. The films were then grown with different oxygen pressures in the PLD chamber; at a base pressure of 2×10^{-5} Torr and further higher oxygen pressures of 1×10^{-4}, 1×10^{-3}, 1×10^{-2}, and 1×10^{-1} Torr. The aim of this work is to compare the changes in the structural and magnetic properties of the films, when changing the oxygen content of the target and changing the oxygen pressure, during the PLD growth process.

Chapter Seven is divided into two sections; the first section contains a summary of the works undertaken in the previous chapters and the main conclusions drawn from them. The second section includes a discussion of possible future work.

1.3 References

[1] M. Ying, A. M. A. Saeedi, M.Yuan, X. Zhang, B.Liao, X. Zhang, Z. Mei, X. Du, S. Heald, and M. Fox and G. Gehring, *Journal of Materials Chemistry C* **7**, 1138 (2019).

[2] M. Yuan, X. Zhang, A. M. A. Saeedi, W. Cheng, C. Guo, B. Liao, X. Zhang, M. Ying, and G. Gehring, *Nuclear Inst. and Methods in Physics Research, B* **455**, 7 (2019).

[3] H. Albargi, M. Alshammari, K. Museery, S.Heald, F. Jiang, A. M. A. Saeedi, A. M. Fox, and G. Gehring, *Coatings* **9**, 381 (2019).

[4] I. Zutic, J. Fabian, and S. Das Sarma, *Reviews of Modern Physics* **76**, 323 (2004).

[5] Y. Xu, *Current Opinion in Solid State & Materials Science* **10**, 81 (2006).

[6] S. Wolf, D. Awschalom, R. Buhrman, J. Daughton, S. Molnar, M. Roukes, A. Chtchelkanova, and D.Treger, *Science* **294**, 1488 (2001).

[7] Y. Xu, S.Thompson , *Spintronic Materials and Technology* (*Taylor & Francis Group, New York,* 2007).

[8] M. Bibes and A. Barthelemy, *IEEE Transactions on Electron Devices* **54**, 1003 (2007).

[9] J. Coey, *Solid State Sciences* **7**, 660 (2005).

[10] H. Ohno, *Science* **281**, 951 (1998).

[11] T. Dietl, *Nature Materials* **9**, 965 (2010).

[12] J. Furdyna, *Journal of Applied Physics* **64**, R29 (1988).

[13] S. Pearton, W. Heo, M. Ivill, D. Norton, and T. Steiner, *Semiconductor Science and Technology* **19**, R59 (2004).

[14] T. Dietl and H. Ohno, *Mrs Bulletin* **28**, 714 (2003).

[15] S.Yoon, S. Cho, S. We, S. Yoon, B. Suh, H. Song, and Y. Shin, *Journal of Applied Physics* **93**, 7879 (2003).

[16] S. Mandal, A. Das, T. Nath, D. Karmakar, and B. Satpati, *Journal of Applied Physics* **100**, 104315 (2006).

[17] T. Tietze, M. Gacic, G. Schuetz, G. Jakob, S. Brueck, and E. Goering, *New Journal of Physics* **10**, 055009 (2008).

[18] A. Ney, K. Ollefs, S. Ye, T. Kammermeier, V. Ney, T. Kaspar, S. Chambers, F. Wilhelm, and A. Rogalev, *Physical Review Letters* **100**, 4, 157201 (2008).

[19] Z. Weng, J. Zhang, Z. Huang, and W. Lin, *Chinese Physics B* **20**, 027103 (2011).

[20] M. Ying, H. Blythe, W. Dizayee, S. Heald, F. Gerriu, M. Fox, and G. Gehring, Applied *Physics Letters* **109**, 5, 072403 (2016).

[21] P. Zhan, W. Wang, C. Liu, Y. Hu, Z. Li, Z. Zhang, P. Zhang, B. Wang, and X. Cao, *Journal of Applied Physics* **111**, 033501 (2012).

[22] N. Hong, J. Sakai, and V. Brize, *Journal of Physics-Condensed Matter* **19**, 036219 (2007).

[23] J. Coey, *Solid State Sciences* **7**, 660 (2005).

[24] B. Straumal, S. G. Protasova, A. Mazilkin, E. Goering, G. Schutz, P. Straumal, and B. Baretzky, *Beilstein Journal of Nanotechnology* **7**, 1936 (2016).

[25] B. Straumal, A. Mazilkin, S. Protasova, A. Myatiev, P. Straumal, G. Schutz, P. Aken, E. Goering, and B. Baretzky, *Physical Review B* **79**, 205206 (2009).

[26] B. Straumal, A. Mazilkin, S. Protasova, P. Straumal, A. Myatiev, G. Schutz, E. Goering, T. Tietze, and B. Baretzky, *Philosophical Magazine* **93**, 1371 (2013).

[27] T. Dietl, H. Ohno, F. Matsukura, J. Cibert, and D. Ferrand, *Science* **287**, 1019 (2000).

[28] J. Coey, M. Venkatesan, and C. Fitzgerald, *Nature Materials* **4**, 173 (2005).

[29] U. Ozgur, Y. Alivov, C. Liu, A. Teke, M. Reshchikov, S. Dogan, V. Avrutin, S. Cho, and H. Morkoc, *Journal of Applied Physics* **98**, 041301 (2005).

[30] M. Ying, H. Blythe, W. Dizayee, S. Heald, F. Gerriu, M. Fox, and G. Gehring, *Materials Letters* **171**, 121 (2016).

Chapter 2 **Overview of Magnetism**

2.1 Introduction

Magnetic materials are greatly used in our daily life as some essential modern applications include data storage, power generation and medical devices. The magnetism present in these materials results from two important mechanisms, the magnetic moment of the atoms and the interactions between them, in order to produce magnetic order.

This chapter contains a description of the principal origins of magnetism and properties of magnetic materials, and it includes a discussion of exchange interactions, particularly direct and indirect types; the indirect types include super-exchange, double-exchange and Ruderman-Kittel-Kasuya-Yosida (RKKY) interactions. It also contains a discussion of the band theory of ferromagnetism. Finally, it contains a discussion of the overview of ZnO and its role as DMS material. Understanding these principles of magnetism is necessary to help us investigate the origin of magnetism in the materials discussed in this work. The overview presented here regarding the origin of magnetism and exchange interactions was found in the following textbooks: *Magnetism and Magnetic Materials* by J. Coey [1]; *The Magnetic Properties of Solids* by J. Crangle [2]; *Magnetic Materials Fundamentals and Device Applications* by N. Spaldin [3]*; Introduction to Magnetic Materials* by B. Cullity [4]; and *Introduction to Solid State Physics* by C. Kittel [5].

2.2 Fundamentals of Magnetism

2.2.1 Isolated Atoms

The fundamental unit of magnetism is the magnetic moment. In isolated atoms, the orbital and the spin angular momentum are considered in order to have a better understanding of the origin of magnetic moments.

In the Bohr atomic model, the negatively charged electron revolves in a circular orbit of radius, *r,* around the positive charge of the nucleus as shown in Fig 2.1. The electron effectively produces a current:

$$I = \frac{-e}{T} \tag{2.1}$$

Where -*e* is the electron charge, and *T* is the period of revolution of the electron:

$$T = \frac{2\pi\, r}{\mathrm{v}} \tag{2.2}$$

Where v is the speed of the electron. By substituting equation 2.2 into equation 2.1, the following can be obtained:

$$I = \frac{-e\, v}{2\,\pi\, r} \tag{2.3}$$

Magnetism is found where the current is present and the magnetic moment, $\boldsymbol{\mu}$, is perpendicular to the current loop and can be written classically in terms of the current loop *I* with an area *A* as the following:

$$\boldsymbol{\mu} = I\,A \tag{2.4}$$

The magnetic moment is given in A.m^2 in SI units or emu in cgs units. The cgs units were the only units used throughout the description of experimental work in this thesis. However, SI and {cgs} units are used in this chapter. By substituting equation 2.3 into equation 2.4, the magnitude of the magnetic moment $\boldsymbol{\mu}$ of an electron with mass, m and charge, $-e$, can be written as the following:

$$|\boldsymbol{\mu}| = I|\boldsymbol{A}| = \left(\frac{-e\,v}{2\,\pi\,r}\right)(\pi\,r^2) = \frac{-e\,v\,r}{2} \tag{2.5}$$

The orbital angular momentum $\boldsymbol{l}$ of the electron is directed in a direction that is antiparallel to the magnetic moment, as shown in Fig 2.1. It may be written classically as:

$$|l| = m|\boldsymbol{r} \times \boldsymbol{v}| = m\,v\,r \tag{2.6}$$

Where $\boldsymbol{r}$ and $\boldsymbol{v}$ are perpendicular to each other. Thus, the magnetic moment can be written, in terms of the angular momentum, as follows:

$$\boldsymbol{\mu} = \frac{-e}{2m_e}\boldsymbol{l} \tag{2.7}$$

Removed

by the author

for copyright reasons

Figure 2.1: The negatively charged electron e^- revolves in a circular orbit where the electron moves anticlockwise, leading to the current being in a clockwise direction. The magnetic moment μ and the angular momentum l in opposite directions [6].

However, quantum mechanics states that the orbital angular momentum eigenvalue is quantised in term of $\hbar$. Hence, the minimum amount of the orbital angular momentum l_{qm} is equal to $\hbar$ $(h/2\pi)$ where h is Planck's constant. The lowest value of the magnetic moment that is non zero for the electron is given by the Bohr magneton, μ_B which is used widely as a unit to express the magnetic moments:

$$\mu_{\mathrm{B}} = \frac{e\hbar}{2m} = 9.27\times10^{-24} J\,T^{-1} \qquad \{\mu_{\mathrm{B}} = \frac{e\hbar}{2mc} = 9.27\times10^{-21}\ erg.G^{-1}\} \tag{2.8}$$

The quantised orbital momentum is proportional to that of the magnetic moment, and hence the magnetic moment itself can be quantised in terms of μ_B:

$$\boldsymbol{\mu}_l = -\,g_l\,\mu_{\mathrm{B}}\,\boldsymbol{l} \tag{2.9}$$

Where g_l is the orbital g- factor with value $g_l = 1$. The magnetic moment component in the direction of the field can be written in terms of the external magnetic field in the z-direction as:

$$\mu_{lz} = -\,\mu_{\mathrm{B}}\,m_l \tag{2.10}$$

Here m_l represents the component of the orbital momentum $\boldsymbol{l}$, which is parallel to the applied field. This magnetic quantum number m_l is allowed to take an integer value from $(-l\ ,-l+1,..,0,..,\ l-1,\ +l)$.

Another kind of angular momentum for the electron is the spin angular momentum. The spin angular momentum is related to the spin magnetic moment $\boldsymbol{\mu}_s$, which makes an additional contribution to the magnetic moment, according to the following expression:

$$\boldsymbol{\mu}_S = -\,g_s\,\mu_B\boldsymbol{s} \tag{2.11}$$

Where g_s is the g-factor of the spin of the free electron, with a value twice as large as the orbital g_l factor, where experimentally g_s is approximated to be ~ 2 [7].

The parallel component of the field from the magnetic moment similarly to the orbital contribution can be written:

$$\mu_{sz} = -\, g_s \, \mu_B m_s \qquad (2.12)$$

The spin magnetic quantum number, m_s, describes the electron spin and may take two possible values $+\frac{1}{2}, -\frac{1}{2}$ corresponding to spin-up or spin-down respectively. Thus, the single electron includes one spin magnetic moment, which equals one Bohr magneton $\pm\mu_B$ along the field direction. The nucleus, similar to an atom, also has a magnetic moment related to its angular momentum. The mass of a nucleus is approximately 2000 times bigger than the electronic mass; hence, the magnetic moment of nuclear spin can be usually neglected because it is tiny.

For atoms with multiple electrons, the total spin angular moment, $\boldsymbol{S}$, and the total orbital angular momenta, $\boldsymbol{L}$, are considered, and the interaction with each other is essential when describing the origin of magnetism. Thus, the total spin angular moment and total orbital angular momentum are given by the vector summation over all the electronic states:

$$\boldsymbol{S} = \sum_i \boldsymbol{s}_i \text{ and } \boldsymbol{L} = \sum_i \boldsymbol{l}_i \qquad (2.13)$$

The summation over full shells is zero because, for a fixed $\boldsymbol{l}$, the overall sum values of the component of the magnetic quantum number $\boldsymbol{m_l}$ inside a shell is also zero. Hence, any non-zero contribution arises only from uncompleted shells. Furthermore, the combination of the total spin angular momentum and total orbital angular momentum leads to the total angular momentum $\boldsymbol{J}$ that occurs through the spin-orbit coupling as given by:

$$\boldsymbol{J} = \boldsymbol{L} + \boldsymbol{S} \qquad (2.14)$$

The spin-orbit coupling is generated when the spin magnetic moment couples with the magnetic field that was created by the orbital motion. Thus, weak relativistic effects are generated, which will be explained later in Section 2.3.

Two possible cases arise from this interaction between the two angular momenta; First, the spin-orbit coupling is weak compared to the residual electrostatic interactions, which usually happens in the elements that have a small or medium atomic number. This kind of interaction, involving the coupling between $\boldsymbol{L}$ and $\boldsymbol{S}$, is called the Russell-Saunders coupling or the LS coupling. The values of the total angular momentum quantum number, $\boldsymbol{J}$, may range from $|L - S|$, $|L - S + 1|, \ldots$, $|L + S - 1|$, $|L + S|$. The magnitude of the total angular momentum is determined by:

$$|J| = \sqrt{J(J+1)}\,\hbar \tag{2.15}$$

The atom has a total magnetic moment which can be obtained as it is given by:

$$\boldsymbol{\mu}_J = -g_J\,\mu_B\,\sqrt{J(J+1)} \tag{2.16}$$

Here g_J is the Landé g-factor as determined by the following:

$$g_J = 1 + \frac{J\,(J+1) + S\,(S+1) - L(L+1)}{2J\,(J+1)} \tag{2.17}$$

The second type of coupling occurs particularly for heavy elements and termed the *jj* interaction, where the interaction between the spin and orbital angular momenta for an individual electron is strong when compared that of different electrons. Therefore, the spin-orbit coupling occurs in all individual electrons first. The final value of $\boldsymbol{J}$ is calculated by summing over the $\boldsymbol{j}$ values of every valance electron as there are given by:

$$\boldsymbol{j}_i = \boldsymbol{l}_i + \boldsymbol{s}_i \tag{2.18}$$

$$\boldsymbol{J} = \sum_i \boldsymbol{j}_i \tag{2.19}$$

2.2.2 Pauli Exclusion and Hund's Rules for Atoms

The Pauli Exclusion Principle states that no two electrons can share the same values for the quantum numbers; n, l, m_l and m_s in an atom. These quantum numbers describe the energy of a single electron. For instance, if two electrons share the same atomic orbital with the same values of n, l, m_l then m_s must be different and have the reversed spin. This principle is particularly important in discussing the exchange interaction energy from atoms and overlapping electronic orbitals. In addition, Hund's rules are essential in order to characterise the lowest-energy configuration or the states of multi-electron atoms, which are listed in the following:

First of all, the overall total spin angular momentum, *S,* has to be maximised. This means that for each orbital the empty shell must first be occupied by unpaired electrons until the orbital half shell is filled, so the spins are parallel in direction to each other. The remaining electrons can then be paired and shared with the same orbital, but with the opposite spin direction as long as the Pauli Exclusion Principle is valid. Secondly, the value of the total orbital angular momentum, *L,* has to be maximised without conflicting with the previous rule. If the orbits of the electrons have identical directions and hence a large total orbital angular momentum, then the electrons meet less often than when they orbit in opposite directions. Thus, the average electron-electron repulsion energy is minimised when L is large.

Thirdly, when the atomic shell is less than half-full, the lowest energy is given by:

$$\boldsymbol{J} = |\boldsymbol{L} - \boldsymbol{S}| \tag{2.20}$$

When the atomic shell is more than half-full, the lowest energy is given by

$$\boldsymbol{J} = |\boldsymbol{L} + \boldsymbol{S}| \tag{2.21}$$

However, when the atomic shell is half-full, then $\boldsymbol{L} = 0$ and $\boldsymbol{J} = \boldsymbol{S}$ and no spin-orbit coupling is involved. The ground state energy depends on the magnitude of $\boldsymbol{J}$. An excellent illustration of typical examples of this are shown in Fig 2.2, where the values of $\boldsymbol{S}$, $\boldsymbol{L}$, and $\boldsymbol{J}$ are compared for the ground state for the less half-filled electron shell of vanadium V^{3+} and more than half-filled electron shell of Fe^{2+}.

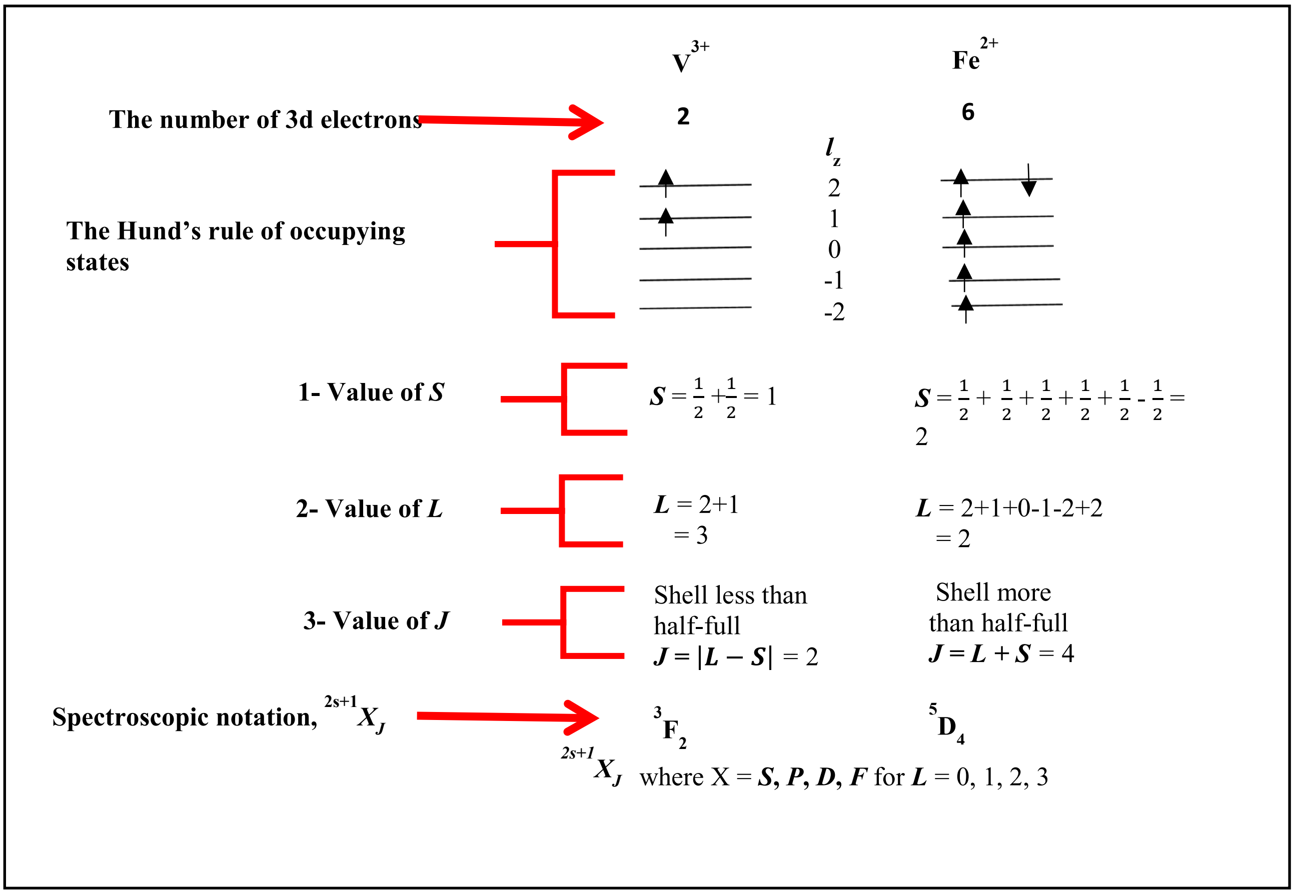

Figure 2.2: The determination of the ground states by the Hund's rules for the less half-filled electron shell of V^{3+} and more than half-filled electron shell of Fe^{2+}.

2.3 Ions and Atoms in Solids

After considering how the magnetic moment arises in an isolated atom, it is therefore understood how the magnetic moment arises. In a crystal, on the other hand, it is necessary to discuss what changes occur because there are many atoms or ions in the crystal and how these affect the magnetism. Both the crystal symmetry and orbital shape determine the electronic distribution of the material. This will modify the electronic and optical properties of the materials. It can be seen from Fig 2.3 that the electron density for p and d-orbitals depend on the distance from the nucleus as well as the direction. The symmetry of the s-orbital is spherical, whereas p-orbitals are not spherically symmetric and have three possible electronic distributions which point towards the x, y, or z-axes. In addition, the d-orbitals are more complex shapes than the p-orbitals. The d-orbitals have two different groups called t_{2g} and e_g; the first points between the Cartesian axes called d_{xy}, d_{yz}, and d_{xz} orbitals. The second group orbitals include $d_{x^2-y^2}$ orbitals point towards x and y-axes, and d_{z^2} orbitals point towards z-axes.

Removed
by the author
for copyright reasons

Figure 2.3: The sketch of the angular distribution shown in the shading for s,p and d-orbitals including e_g and t_{2g} that describe the d-orbitals, which is taken from [8].

Crystal Field

The crystal field energy arises from an electric field produced by the neighbouring atoms in the crystal acting on a TM or RE ion. The crystal field theory states that the orbitals of the neighbouring atoms can be represented as negative charges and depend on the symmetry of the local environment, which then determines the distribution type and strength of the field. This theory is useful to understand how the d-orbitals behave in metallic oxides.

For example, in magnetite a metal ion sits in the centre of an octahedron with an oxygen ion at each vertex, the crystal field energy depends on the type of d-orbitals, i.e. t_{2g} or e_g. The preferred type of orbital minimises the electrostatic repulsion interaction between p-orbitals of the oxygen ion and the d-orbitals of the metal ion. Fig 2.4 (a) shows the crystal field splitting, Δ, which is the energy by which the two metal d-orbital types raise or lower the configuration energy. Of the two d-orbital groups, e_g raises the energy by $3\Delta/5$ whereas t_{2g} lowers the energy by $2\Delta/5$ since the surrounding oxygen p-orbitals have less overlap with d-orbitals. On the other hand, in a tetrahedral environment, as shown in Fig 2.4(b) [8], the opposite is true and the metal ion prefers the e_g orbitals over t_{2g} orbitals configuration.

For a partially filled d-shell, with an octahedral configuration, for example, electrons fill the lower levels before any other. There is a distribution though of the electrons in the orbital depending on the competition of two important energies: they are the energy of the spin pairing and crystal-field. Two different situations can occur with four or more electrons available to fill the orbitals: The first one is called the weak field case, where the electrons singly would occupy all the orbitals, resulting in a parallel alignment of spins. Then, the electrons are allowed to doubly occupy the orbitals. This arises for pairing energy higher than that of the crystal field energy. The week field is assumed in the materials discussed in this thesis. The second is a strong field case, where the electrons doubly start to fill every orbital in a lower state before moving to a higher level. This takes place, hence the crystal field energy is higher than the pairing energy.

Removed

by the author

for copyright reasons

Figure 2.4: The sketch of the *d*-orbitals of the crystal field in both environments (a) octahedral and (b) tetrahedral taken from [8].

Orbital Quenching

Table 2.1 lists the experimentally determined magnetic moments of transition metal (TM) ions, P_{exp}, and the effective magnetic moment gives by the Landé theory, P_1. Hund's rules, as described in Subsection 2.2.2, are used to calculate the quantised momentum values of S, L, J, and the expectation value of the moment $P_1 = g_J\ [J(J+1)]^{\frac{1}{2}}$.

The large difference between P_{exp} and P_1, apart from half and fully complete d-orbitals, results from the interaction of the crystal field with the d orbitals, which is stronger than that of the spin-orbit interaction in the case of 3d ions. It indicates that Hund’s third rule cannot be assumed correct since it required that the second strongest interaction is the spin-orbit coupling after the Coulomb interaction. Thus, the results in Table 2.1 shows the comparable effective moments determined by taking only spin into account, where $L = 0$, $J = S$ and g_J, the Landé

g-factor, has the value 2. The effective magnetic moment can be written as the following:

$$\mu_{eff} = 2\mu_B \sqrt{S(S+1)} = P_2\,\mu_B \tag{2.22}$$

The comparable results values of P_{exp} and P_2 imply that the orbital is quenched. The reason behind this is that the orbital angular momentum was forced by the strong crystal field, for the 3d ions, to be bound to the crystal lattice. Hence, the orbital angular momentum does not contribute to the total angular momentum. However, the spin is not affected by this as the interaction spin-orbit is weak.

Table 2.1: The value of the effective magnetic moment with the calculated S,L,J, and the ground state energy term, taken from reference [6].

Removed

by the author

for copyright reasons

2.4 Magnetic Materials

All materials can be magnetised, and they are classified according to their behaviour under the influence of a magnetic field. The magnetic field $\boldsymbol{H}$ is produced by the current, and the resulting magnetic induction, $\boldsymbol{B}$, has a potential energy of $U = -\boldsymbol{B}.\boldsymbol{M}$ where **B** within the material may be written as:

$$\boldsymbol{B} = \mu_o(\boldsymbol{H} + \boldsymbol{M}) \qquad \{\boldsymbol{B} = \boldsymbol{H} + 4\pi\boldsymbol{M}\} \tag{2.23}$$

Where μ_0 is the permeability of free space, and $\boldsymbol{B}$ is given in Tesla in SI units. The relationship between the magnetisation, $\boldsymbol{M}$, which defines as the quantity of magnetic moment, m, per unit volume, V, can be defined as the following:

$$\boldsymbol{M} = \frac{\boldsymbol{m}}{V} \tag{2.24}$$

Where $\boldsymbol{M}$ is given in A/m in SI units and emu/cm^3 in cgs units.

The susceptibility is determined by dividing the magnetisation over the applied magnetic field, $\boldsymbol{H}$, in the low field and the equation below is given:

$$\chi = \frac{\boldsymbol{M}}{\boldsymbol{H}} \tag{2.25}$$

The susceptibility is a dimensionless quantity because $\boldsymbol{H}$ and $\boldsymbol{M}$ share the same units. The hysteresis loops are studied that describe the dependence of $\boldsymbol{M}$ or $\boldsymbol{B}$ on $\boldsymbol{H}$. The magnetic materials can be divided roughly into five different categories; depending on the sign and magnitude of their magnetic susceptibilities:

2.4.1 Diamagnetism

Diamagnetism is a property of all materials although, in most cases, it is swamped by other magnetic effects. Increasing the magnetic field applied to any material from zero will produce an induced emf. This induced emf, according to Lenz's law, attempts to screen the inside of the material from the external field. Hence χ_{dia} is negative and typically of the order of 10^{-6} in SI units. It is almost temperature independent and arises entirely due to the orbital motion of electrons in atoms. It is a characteristic of non magnetic insulator such as sapphire, which all have full electron shells and therefore exhibits no other forms of magnetism. In our experiments, the sapphire substrate was used because it is a transparent diamagnetic, as it will be discussed in Section 3.6.

2.4.2 Paramagnetism

Almost all solids which have isolated atoms or ions with partially filled d or f electron shells are paramagnetic at elevated temperature. In zero field, the magnetic moments have random orientations resulting in zero net magnetisation. When an external magnetic field is applied to them, some of them become parallel to the field so the sample is magnetised. The magnetisation is linearly field-dependent in low fields and vanishes on the removal of the field. The susceptibility (χ) varies inversely with the temperature, and may be written as:

$$\chi = \frac{C}{T} \tag{2.26}$$

This is known as Curie's law, C being the Curie constant. For paramagnetic substances, χ_{para} is typically in the range $10^{-5} < \chi_{para} < 10^{-3}$. Curie's law is valid if the material concerned has no interactions between the magnetic ions.

The Curie constant is given by:

$$C = \frac{N\mu_B^2\, P_{eff}^2\, \mu_0}{3k_B} \qquad \{C = \frac{N\mu_B^2\, P_{eff}^2}{3k_B}\} \tag{2.27}$$

Where k_B is Boltzmann's constant, N is the total number of magnetic atoms per unit volume V and P_{eff} is the effective magnetic moment. However, not all paramagnetic materials obey equation 2.26; hence, the modified Curie law is given by:

$$\chi = \frac{C}{T-\theta} \tag{2.28}$$

This is known as the Curie-Weiss law, θ is the paramagnetic Curie temperature or the Curie-Weiss constant, which is due to interactions. This equation holds for ferromagnetic materials below their Curie temperature. In the case of antiferromagnetic materials, they are paramagnetic above the Néel temperature, θ_N, as shown below:

$$\chi = \frac{C}{T+\theta_N} \tag{2.29}$$

The inverse susceptibility is plotted as a function of temperature to obtain θ as shown in Fig 2.5. It is noticeable that inverse of the susceptibility has changed linearly and intercepted the x-axes at T= - θ [9]. The materials behave paramagnetic when $\theta = 0$ as shown in equation 2.26. The materials will become ferromagnetic at low temperature when $\theta > 0$ and will become antiferromagnetic when $\theta < 0$.

It is worthwhile mentioning that non ferromagnetic metal for example, Cu or Na are paramagnetic, but this is so called Pauli paramagnetism which is not discussed here.

Removed

by the author

for copyright reasons

Figure 2.5: Inverse susceptibility vs temperature for antiferromagnetic (green), paramagnetic (black) and ferromagnetic (red) materials, where $\theta < 0$, $\theta = 0$ and $\theta > 0$ respectively, as taken from [9].

2.4.3 Ferromagnetism (FM)

Below their Curie temperature, *Tc,* ferromagnetic substances produce a complicated picture of the magnetisation as a function of the field. Strong ferromagnetic interactions have the majority of magnetic moments aligned in the same direction and parallel to each other, generating an internal magnetic field called the molecular field. Such behaviour exists regardless of the external magnetic field, leading to spontaneous magnetisation as is illustrated in Fig 2.6. Above *Tc*, a ferromagnetic behaves as a paramagnet with susceptibility given by equation 2.28. This phenomenon occurs due to thermal fluctuations, which break down the overall alignment of the magnetic moments. A ferromagnetic material has both values of *Tc* and θ positive, and *Tc* is slightly smaller than θ by ~ 10%.

The magnetisation of a ferromagnetic depends on its history; this gives rise to a hysteresis loop as shown in Fig 2.7. Ferromagnetic materials behave non-linearly with the applied external magnetic field. When an external magnetic field is applied to the material, the magnetisation rises until it reaches a maximum, this is known as the saturation magnetisation, *M*s. In addition, when the applied magnetic field decreases to zero, the magnetisation does not retrace the original path and reduce to zero. Rather, it decreases to a value called the remanence, *Mr*. If the direction of the applied field is now reversed, the magnetic field reaches a finite negative value, at which point the sample has zero magnetisation, this is called the coercive field, *Hc*. When the field is further increased, the sample eventually reaches saturation magnetisation in the opposite direction, *Ms.*

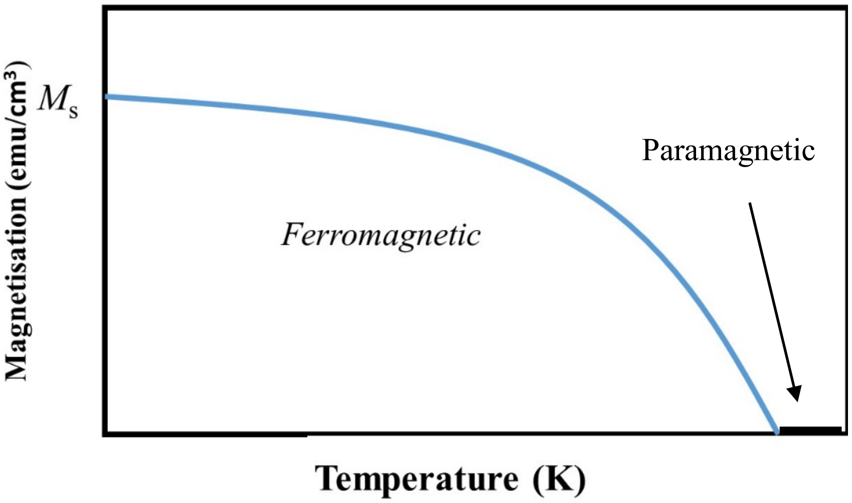

Figure 2.6: Magnetisation as a function of temperature of a ferromagnetic material in zero field.

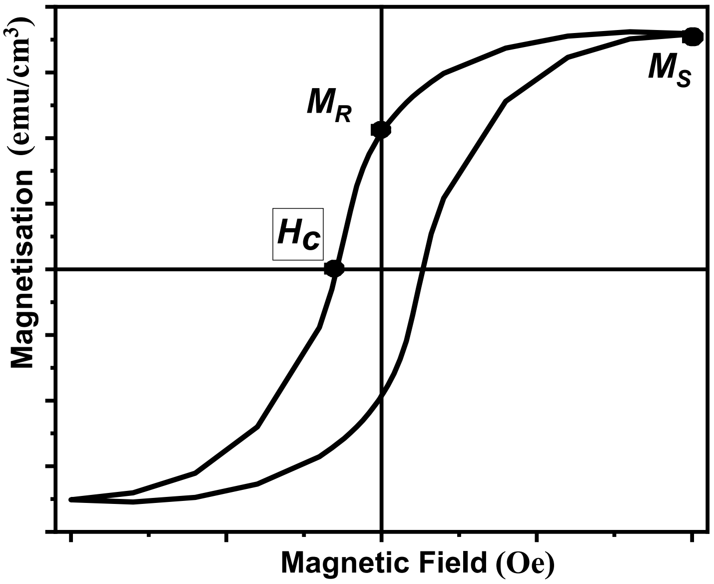

Figure 2.7: Key features of the hysterisis loop indicating the saturation magnetisation, Ms, the remanent magnetisation, *Mr* and the coercive field, *Hc*.

2.4.4 Antiferromagnetism (AFM)

In antiferromagnetic materials, the atoms are arranged on two sub-lattices; one has the magnetic moments aligned parallel to each other, and the second has the magnetic moments pointing anti-parallel to the first one. Thus, it gives no overall net magnetisation. Above the Néel temperature, T_N, moments are disordered and antiferromagnetic materials become paramagnetic similarly to that of a ferromagnet below Tc. Nevertheless, below $T_{N,}$ the neighbouring atomic moments are antiparallel to each other, which leads to a zero net magnetisation. The magnetic susceptibility obeys a modified Curie-Weiss law as shown in equation 2.29.

2.4.5 Ferrimagnetism

Ferrimagnetism is the word first used by Néel to describe the magnetism of the ferrites. Ferrimagnets, similar to ferromagnets, show spontaneous magnetic moments below their critical temperature, exhibiting hysteresis; above this critical temperature, they exhibit paramagnetism. The electron spins are ordered on two sub-lattices with unequal numbers of magnetic ions on each lattice and opposing spin directions. Thus, the effective magnetic moment on one lattice is larger than the other, giving rise to a net magnetisation. Ferrimagnets are usually non-metals, typically oxides and semiconductors; the spinel ferrites are a particularly well-known group.

2.5 Exchange Interactions

In this section, a situation where the magnetic ion has localised spins is considered. However, band magnetism will be discussed in Section 2.6. Exchange interactions of the magnetic moments are due to the coupling or the overlapping of electrons in conjunction with the Pauli exclusion principle. The interaction between neighbouring ions and atoms causes individual spins to be in either parallel or antiparallel alignment with their neighbours, depending on the Coulomb electrostatic interaction. The spins pointing in the same direction tend to be moved apart to save energy. This exchange interaction is responsible for producing the magnetic order of the materials. The competition between the kinetic energy and the Coulomb electrostatic interaction is a consequence of the exchange coupling of the magnetic moments. There are several different categories of exchange interactions depending on long or short-ranged order, or the resulting alignment being FM or AFM. In this section, the Exchange Interactions is categorised into two groups, direct exchange and indirect exchange:

2.5.1 Direct Exchange Interactions

Direct Exchange Interaction is the interaction that occurs between the neighbouring atoms in an insulator without involving any atom in the middle. The result of such interactions is strong and leads to antiferromagnetism. However, it is a short-ranged coupling and is reduced quickly with respect to the distance between coupling atoms. If two single free atoms were located beside each other, their wave functions would interfere. As mentioned previously, the Pauli principle states that no single electron can have the same energy state; thus, the total wave functions are antisymmetric. The parallel spins of electrons avoid each other by occupying different spatial orbitals, leading to a greater distance between them in which the electron-electron repulsion energy is decreased.

2.5.2 Indirect Exchange Interactions

Indirect Exchange Interaction occurs when a large distance is present between the magnetic moments and direct interaction coupling is not possible. The magnetic oxide behaviour can be explained as an exchange interaction such as super-exchange, double exchange, and (RKKY) exchange.

2.5.2.1 Super-Exchange Interaction

Super-Exchange Interaction occurs when the nearest magnetic ions of non-neighbouring cations interact *via* intermediate ion. This kind of interaction usually occurs in insulators such as oxides, where O^{2-} electrons play an important role by virtually hopping. This interaction leads to spontaneous virtual transfer between two electrons and causes the formation of an excited state.

The transition metal oxides (TMO), MnO, are excellent examples of a Super-Exchange Interaction. MnO has a d-orbital, which is half-full, leading to two possible configurations of d-orbitals that can couple with the p-orbital of the oxygen. This interaction can be either antiparallel or parallel spins. Nevertheless, the favoured one is the antiparallel spin over the parallel spin due to its lower energy. Hence, the two electrons of the oxygen p-orbital would be interacted with unoccupied d-orbitals.

The geometry of Mn-O-Mn is important to choose the type and the strength of the Super-Exchange Interaction, according to the Goodenough-Kanamori-Anderson rules (GKA) [10]. This why the Super-Exchange Interaction can be either antiferromagnetically strong or ferromagnetically weak. Fig 2.8 (a) shows the strong antiferromagnetic (antiparallel) Super-Exchange while Fig 2.8 (b) shows the weak ferromagnetic (parallel) Super-Exchange.

GKA rules are maintained for super-exchange energy, which is summarised as the following:

1- If there are two cations with lobes of magnetic orbital, where the d-orbitals are singly occupied and these orbitals point towards the p-orbital of the anion, then there is large overlap. This leads to a strong Super-Exchange Interaction, favouring an antiferromagnetic exchange which satisfies the Pauli exclusion principle. This is called the 180° Super-Exchange Interaction and it occurs in Mn-O-Mn as shown in Fig 2.8 (a).

2- If there are two cations with lobes of magnetic orbital, where the d-orbitals are coupled with different p-orbital, then no overlap occurs in the p-orbital pointing in a different direction to the d-orbital by symmetry. Then, the electron of the d-orbital is unable to interact with the electron in the electron on the opposing side. This results in a weak ferromagnetic interaction and is called the 90° Super-Exchange Interaction as shown in Fig 2.8 (b).

Removed
by the author
for copyright reasons

Figure 2.8: Schematic of both types of indirect Super-Exchange Interaction in MnO, (a) Strong antiferromagnetism of super-exchange and (b) Weak ferromagnetism of Super-Exchange Interaction as taken from [11].

2.5.2.2 Double exchange interactions

The Double Exchange Interaction (DE) was discovered by Zener *et al* [12,13], who was the first to propose the ferromagnetism of the interacting d-shells in TM, as was observed in manganese with the perovskite structure [13]. The DE interaction is indirect, takes place between the spins of magnetic ions, and requires a mixed-valence configuration. This type of interaction can be seen in oxides where two neighbouring TM ions exist. In this case, one TM ion has an extra electron occupying the ground state, which can then move back and forth between valence states.

The system Mn^{3+} O^{2-} Mn^{4+} for instance, contains two moving electrons at the same time; one in which the electron moves from the O^{2-} to Mn^{4+} empty e_g orbital while the other extra electron transfers from the Mn^{3+} e_g orbital, to the O^{2-} [11,14,15] as illustrated in Fig 2.9. Subsequently, the system changes to Mn^{4+} O^{2-} Mn^{3+} and the energy is conserved in this system as well as the one mentioned earlier because the spin orientation is also conserved.

Removed

by the author

for copyright reasons

Figure 2.9: Example schematic of the indirect ferromagnetic Double Exchange Interaction occurring between the Mn^{3+} and Mn^{4+} ions via the p-orbital of the O^{2-} ion, as modified from [1].

In short, the main difference between the previous indirect interaction, Super-Exchange and Double Exchange Interaction is that the former takes place when two ions share the equal number of valence electrons and the latter takes place when two atoms have unequal numbers of valence electrons.

2.5.2.3 The RKKY exchange interactions

The RKKY exchange interaction takes place in metals and explains the magnetic interaction occurring between the magnetic moment of a localised ion, due to partially filled shells, and the delocalized mobile conduction electrons in the sp-band. For example, the 4*f* electrons shell in the rare earth elements is responsible for the observed magnetism when interacts with 6*s* or 5*d* in the conduction band. This interaction can be explained by the polarisation of the delocalised conduction electrons interacting with the localised magnetic moment. As a result, the interaction of the polarisation with the surrounding localised magnetic moment occurs at a distance *r* with respect to the initial magnetic moment. This is an exchange interaction of indirect type because it takes place via the conduction electrons; this is called the RKKY interaction or itinerant exchange interaction. The exchange integral of the two localized moments, which are divided by distance *r* can be expressed as the following:

$$J_{RKKY}\,(\mathrm{r}) \sim \frac{\cos(2k_F r)}{r^3} \tag{2.30}$$

Where k_F is radius after considering a spherical Fermi surface. According to equation 2.30, this result is a long-ranged interaction with the oscillatory character from positive to negative depending *r*, which leads to ferromagnetic or antiferromagnetic [17], as illustrated in Fig 2.10.

Removed
by the author
for copyright reasons

Figure 2.10: Illustration of the indirect exchange interaction of RKKY ferromagnetic/antiferromagnetic as a function of the interatomic distance *r as* taken from [9].

2.6 Band Theory of Ferromagnetism

This section includes a discussion of magnetic atoms that have delocalised electrons. Most of the TMs elements have unfilled 3d shells and the magnetic moment value per unit atom is non-integral, which means that the magnetic moment, which arises cannot be explained from the basis of the localised moment on atoms. Thus, the localised moments are not involved in the resulting magnetisation. Magnetisation arises due to the existence of unpaired electrons in a material, hence completely filled energy bands cannot contribute to the magnetic moment. The imbalance of spins in partially filled bands results in a net magnetic moment in a ferromagnetic material. This occurs in the absence of an external magnetic field, where some of the spin-down electrons at the Fermi level are considered to flip their spin and move into the spin-up band, as shown in Fig 2.11 (a).

The number of electrons migrating due to spin-flip increases the energy δE in the spin-up channel which is considered as the energy required for a spin-flip. The band splitting is equal to $2\mu_B$ and the spin polarisation is i.e $n_\uparrow - n_\downarrow \neq 0$, where $n_\uparrow$ and $n_\downarrow$ are the number of the spin up and spin down electrons respectively. The magnetisation, M due to promoting electrons from spin-down to spin-up is given as

$$M = (n_\uparrow - n_\downarrow)\, \mu_B \approx \mu_B g\, (E_F)\, \delta E \qquad (2.31)$$

Where E_F is the Fermi energy. The total density of states is $g(E_F) = g_\uparrow(E_F) + g_\downarrow(E_F)$ and the total kinetic energy which describes the number of electrons which is converted by $\frac{1}{2}g(E_F)\delta E$. This can be increased by δE, and hence the total kinetic energy can be written as the following:

$$\Delta E_{K\cdot E} = \frac{1}{2}\, g(E_F)\, \delta E^2 \qquad (2.32)$$

The molecular field energy is

$$\Delta E_{\mathrm{P\cdot E}} = -\frac{1}{2}\, Ug(E_F)^2\, \delta \mathrm{E}^2 \qquad (2.33)$$

Where U is a measure of Coulomb energy and can be written as $U = \mu_0 \mu_B^2 \lambda$, where λ is the exchange energy interaction produced by all other electrons. The electrons move from spin-down to spin-up sub-bands in the absence of an external field due to an increase in the kinetic energy that is accompanied by a decrease in the molecular field energy, which occur spontaneously as Fig 2.11 (b) demonstrates. Hence, the total energy change ΔE is given as:

$$\Delta E = \Delta E_{K\cdot E} + \Delta E_{P\cdot E} = \frac{1}{2}\, g(E_F)(\delta E)^2\, (1 - Ug(E_F)) \qquad (2.34)$$

Spontaneous magnetisation occurs only when $\Delta E < 0$. Therefore, the result of equation 2.34 can only be less than zero when $Ug\ (E_F) \geq 1$; this is the Stoner criterion. To satisfy this, the Coulomb repulsion between electrons is large and the density of states at the Fermi-level for a particular channel is larger, causing spin splitting *via* exchange interaction.

Thus, if spontaneous ferromagnetism occurs, the band of spin-up and spin-down splits by an energy Δ, where Δ is the exchange splitting when no magnetic field is applied. The high value of magnetisation can be attributed to band ferromagnetism (also called the itinerant ferromagnetism), which occurred because of spontaneously spin-split bands. This type of band split can occur from defect states in grain boundaries or substitutional defect states in oxides as will be discussed in Chapter 4.

Removed
by the author
for copyright reasons

Figure 2.11: Schematic diagram of the electron density of states showing the spontaneous splitting of energy bands in the absence of an applied field (**a**) shows spin-flip (**b**) resulting band splitting due to spin-flip [6].

2.7 Overview of ZnO

All the work studied in this thesis are concerned with the magnetisation investigation of ZnO thin films that were doped with a variety of dopants including transition metals (TMs), rare earth elements (RE) and non TM-dopants. Here the important details concerning crystal structure, electronics, optical, and lattice dynamics are discussed in order to explain more about ZnO characteristics.

2.7.1 Properties of ZnO

Zinc oxide (ZnO) is a semiconductor belonging to the II-VI binary compound group of semiconductors because zinc and oxygen can be found in the 2nd and 6th groups of the periodic table respectively. ZnO is a nonmagnetic semiconductor and is considered as one of the most important host semiconductors of DMS [16,17]. High-quality bulk ZnO single crystals and samples are also widely available which results in low total cost when making ZnO based devices in comparison to other materials [17].

2.7.2 Crystal Structure

ZnO crystallises into 3 different structures as shown in Fig 2.12, the cubic (rocksalt), zinc-blende and hexagonal wurtzite structure, where each zinc ion is surrounded by four neighbour ions in a tetrahedron configuration and vice versa [17]. The thermodynamically stable phase is the wurtzite structure, in ambient conditions however the zinc-blende structure is also stable but only if it is grown on a cubic substrate. Nevertheless, ZnO can also form the rocksalt (NaCl) structure at relatively high pressure. All the ZnO systems studied in this thesis crystallised into the wurtzite structure.

The ZnO wurtzite structure is comprised of two inter-penetrating hexagonal closely packed (hcp) sub-lattices. In each sub-lattice, one type of atom is displaced with respect to the others along with threefold *c*-axis symmetry [17]. In Fig 2.12(c) ***a*** and ***b*** denote the primitive translation vectors which are equal in length and are at an angle of 120° to one another; the third axis is the c-axis which points in the directions of the tetrahedrally bound orbitals. The four-digit miller indices *hkil* are assigned to the orientation of the axes and faces in a wurtzite lattice. The *c*-axis is referred to as the [0001] direction, such that the surface is therefore perpendicular to the *c*-axis, the hexagonal (0001) plane lies along with it.

Removed

by the author

for copyright reasons

Figure 2.12: ZnO crystal structures: (**a**) cubic rocksalt, (**b**) cubic zinc-blende and (c) hexagonal wurtzite. The black spheres and shaded grey denote Zn and O atoms respectively, adapted from [17].

Wurtzite structure ZnO has a density of 5.675 g/cm^3 and the molecular weight is 81.38 g/mol, with an average atomic weight of 40.69 amu. The unit cell of ZnO consists of two Zn and two O atoms giving a total molecular weight of 162.76 per unit cell. The measured and calculated lattice constant of the ZnO wurtzite structure has been compiled from various experimentally published data sets. It is found that *a* is in the range between 3.2475 to 3.2501 Å and *c* is between 5.2042 to 5.2075 Å [17], where the ratio of *c/a* values are between 1.593 and 1.6035.

The bond polarity of ZnO caused the *c*-axis [0001] to have pronounced polar character. Hence the electrostatic forces have caused a small deviation from the ideal wurtzite geometry and the tetrahedrons are destroyed slightly. As a result, the ratio of *c/a* decreases with respect to the ideal wurtzite geometry value of $(8/3)^{1/2} = 1.633$.

Three surfaces and planes (0001), (11**2**0) and (1**1**00) are of particular importance in wurtzite structure. Their corresponding directions are [0001], [11**2**0] and [1**1**00], respectively. The (0001) is a basal plane and is typically used in epitaxial growth. These main directions and planes are shown in Fig 2.13 [18]. In addition, the sequence of positively charged Zn^{2+} and negatively charged O^{2-} ions, which lie in the planes perpendicular to the *c*-axis, imply that two faces of opposite polarity exist along the hexagonal *c*-cut ZnO crystal: The two most common face terminations are the polar Zn terminated (0001) and O terminated (000**1**) faces on opposite sides. These polar surfaces are known to have different physical properties, which influence not only how prone the film is to defects but also the electronic structure and magnetic behaviour [19-21], see Chapter 4 for a detailed discussion.

Removed

by the author

for copyright reasons

Figure 2.13: The most important planes in the ZnO crystal structure, taken from reference [18].

In this thesis, the lattice spacing of the crystal structures is determined using Bragg and X-ray diffraction as will be discussed in Section 3.3.1. All the samples in this thesis have a well-defined crystal orientation and are *c*-plane oriented.

2.7.3 Electronic Structure and Optical Properties

ZnO is desirable for use in semiconducting devices because of its inherent wide band gap. The structure of the electronic band gap in ZnO has been measured and calculated previously [22,23]. Fig 2.14 shows the resulting structure from the calculated wurtzite ZnO band structure [24]. The band structure follows high symmetry lines and is shown occurring in the hexagonal Brillouin zone. The maxima of the valence and the minima conduction band both occur at the Γ point k = 0, this implies that ZnO is a direct band gap semiconductor.

The energy band diagram in Fig 2.14 shows that the first 10 bands have energies of approximately -9 eV as derived from the Zn 3d levels. The subsequent 6 bands correspond to the O 2p levels and can be seen in the range from -5 to 0 eV. The uppermost lines are strongly Zn located corresponding to the empty available Zn 3s bonding states. Finally and perhaps most importantly that the inherent band gap is 3.4 eV. This is advantageous because a large band gap allows for high breakdown voltages, sustainable large electric fields, noise reduction.

The optical properties of ZnO are dependent on the energy of the band structure. The band gap energy of ZnO can also be measured employing optical absorption such that an electron in the valence band can be excited to the conduction band *via* the absorption of a photon of light with sufficient excitation energy. ZnO is transparent for photon $\hbar\omega < E_g$ and absorb strongly $\hbar\omega > E_g$, where ω is the angular frequency of light.

Removed

by the author

for copyright reasons

Figure 2.14: Electronic band structure of ZnO as calculated, where the horizontal dashed lines indicated the measured gap energy, as taken from [24].

2.7.4 Lattice Dynamics

In this subsection, the lattice dynamics is described for use as a reference alongside the Raman spectra measurements as will be discussed in Subsection 3.3.2. The wurtzite structure of ZnO has 4 atoms in a unit cell, with 12 resulting phonon modes as per the following: 1 longitudinal-acoustic (LA), 2 transverse-acoustic (TA), three longitudinal-optical (LO) and 6 transverse-optical (TO) branches. Firstly, the two E_2 non-polar branches are only Raman active whereas the A_1 and E_1 branches are both Raman and infrared active. Secondly, vibrations of the Zn sublattice are attributed to the E_2^{low} mode and the E_2^{high} mode is associated with only the O atoms. Finally, the B_1 branch is always inactive. All of the modes are crucial to consider when attempting to understand the optical, electronic and thermal crystal properties. There has been extensive modelling of ZnO phonon modes [17]. Table 2.2 provides a list of experimentally determined values of those commons phonons modes that are visible at 300 K as measured by Raman spectroscopy [27].

Table 2.2 Experimentally determined principal phonon modes measured using Raman spectroscopy in wurtzite ZnO at 300 K [27].

Phonon mode	Value(cm^{-1})
$E2^{low}$	101
$E2^{high}$	437
$TO(A_1)$	380
$LO(A_1)$	574
$TO(E_1)$	591

2.7.5 Native Point Defects

There are different types of point defects that could occur in ZnO with different ionisation energies: O and Zn vacancies (V_O and V_{Zn}), interstitials (Zn_i and O_i), and antisites O_{Zn} and Zn_O. However, O and Zn vacancies are known to be the predominant ionic defect types [28, 29]. The formation energies of native defects shown in Fig 2.15 are calculated in either oxygen-rich or zinc-rich conditions as a function of the Fermi-level position; the defects that are favoured under zinc-rich conditions are donors (p-type), while those that are favoured under oxygen-rich conditions are acceptors (n-type). The low formation energies of native defects such as oxygen vacancies and zinc vacancies in ZnO are ascribed to the incorporation of zinc and oxygen atoms.

Removed
by the author
for copyright reasons

Figure 2.15: Positions of native point defects within the ZnO lattice, left shows zinc-rich conditions and right shows oxygen-rich conditions. The 0 eV position of the Fermi level represents the valance band maximum, the position at ~3.4 eV represents the conduction band minimum, taken from reference [29].

The doping of ZnO and the resultant effects of different impurities and intrinsic defects in ZnO are extensively reviewed in [28] and in Chapters 4,5, and 6. The point defects are important in changing the electrical properties of semiconductors and hence the magnetisation, by adding to or taking away charge carriers. As-grown ZnO thin film, with a wurtzite structure, is generally an n-type semiconductor with O vacancies, which is described as adding charge carriers in the form of mobile electrons to systems. This n-type ZnO semiconductor is easily obtained by doping with various impurity materials, including TMs. However, the defects, which the carriers are added in the form of holes, are known as p-type defects. This p-type ZnO semiconductor is difficult to produce for the following factors: the tendency toward n-type conductivity, low-energy native defects compensating the attempted p-type dopant and some of the centres of compensation.

The position of the intrinsic and impurity defects within the band/ band gap and the type of defects determines whether they are electronically active or not. A detailed description of how the position of a defect is determined is outside the scope of this work. In general, there are two types of point defects: intrinsic and extrinsic, the latter being usually isolated impurity atoms. Here, the focus is on reviewing the most mentioned ZnO native defects - oxygen vacancies and zinc vacancies which are going to play an important part in Chapter 4 and 6.

2.7.5.1 Oxygen Vacancies (V_O)

The electrons, normally bound to the missing O atom, can be seen as contributions from the four neighbouring Zn sites, thus giving half an electron each. The electrons in question are still present, at least always where an uncharged defect is concerned; hence the two additional electrons originally residing at the O site requires that the V_O is a (double) donor.

Oxygen vacancies are among defects that behave as donors have the lowest formation energy, as shown in Fig 2.15. The transition levels ε (2+/0) of ZnO are located at approximately 1 eV below the conduction band minimum (CBM), where the oxygen vacancies are stable when in the neutral charge state in n-type ZnO, which means they are not the source of n-type conductivity of ZnO. Due to the 'negative U' shape, the transition levels ε (2+/+) and ε (+/0) reside in the conduction band. However, the oxygen vacancies can compensate for this in p-type ZnO assuming that Vo's are in neutrally charged states when the Fermi level is near CBM.

2.7.5.2 Zinc Vacancies (V_{Zn})

Zinc Vacancies are acceptors in ZnO. As shown in Fig 2.15, the formation energy of Zinc Vacancies decreases with increasing Fermi level, which means it can be formed more easily in n-type samples. The Zinc Vacancies in ZnO are derived from the broken neighbouring bonds from the four nearest oxygen neighbours, resulting in partially occupied states lying close to the valance band maximum (VBM). In p-type ZnO, the formation of Zinc Vacancies requires high energy; thus they should exist at very low concentrations, while the opposite is true where n-type ZnO is concerned, where the vacancies act as compensating centres [29].

2.8 References

[1] J. Coey, *Magnetism and magnetic materials* (Cambridge University Press, Cambridge, 2010).

[2] J. Crangle, *The magnetic properties of solids* (Edward Arnold, London, 1977).

[3] N. Spaldin, Magnetic materials: f*undamentals and applications* (Cambridge University Press, Cambridge, New York, 2011).

[4] B. Cullity, *Introduction to Magnetic Materials* (Wiley, 2009, Hoboken, 2009).

[5] C. Kittel, *Introduction to solid state physics* (Wiley, Hoboken, NJ, 2005).

[6] S. Blundell, *Magnetism in condensed matter* (Oxford University Press, Oxford, 2001).

[7] H. Ohno, Science **281**, 951 (1998).

[8] S. Chikazumi, *Physics of ferromagnetism* (Clarendon, Oxford, 1997).

[9] M. Getzlaff, *Fundamentals of magnetism* (Springer Science & Business Media, 2007).

[10] J. Goodenough, *Physical Review* **100**, 564 (1955).

[11] A. Haghiri-Gosnet and J. Renard, *Journal of Physics D-Applied Physics* **36**, R127, Pii s0022-3727(03)52664-x (2003).

[12] C. Zener, *Physical Review* **81**, 440 (1951).

[13] C. Zener, *Physical Review* **82**, 403 (1951).

[14] I. Solovyev and S. A. Nikolaev, *Physical Review* B **87**, 144424 (2013).

[15] S. Nikolaev and I. V. Solovyev, *Physical Review* B **89**, 064428 (2014).

[16] S. Zhou, K. Potzger, Q. Xu, G. Talut, M. Lorenz, W. Skorupa, M. Helm, J. Fassbender, M. Grundmann, and H. Schmidt, *Vacuum* **83**, S13 (2009).

[17] U. Ozgur, Y. Alivov, C. Liu, A. Teke, M. Reshchikov, S. Dogan, V. Avrutin, S. Cho, and H. Morkoc, *Journal of Applied Physics* **98**, 041301 (2005).

[18] A. Konar, A. Verma, T. Fang, P. Zhao, R. Jana, and D. Jena, *Semiconductor Science and Technology* **27**, 17, 024018 (2012).

[19] Z. Liu, X. He, Z. Mei, H. Liang, L. Gu, X. Duan, and X. Du, *Journal of Physics D-Applied Physics* **47**, 105303 (2014).

[20] L. Li, M. Jurkovic, W. Wang, J. Van Hove, and P. Chow, *Applied Physics Letters* **76**, 1740 (2000).

[21] M. Ying, W. Cheng, X. Wang, B. Liao, X. Zhang, Z. Mei, X. Du, S. Heald, H. Blythe, M. Fox, and G. Gehring, *Materials Letters* **144**, 12 (2015).

[22] S. Jung, W. Park, H. Cheong, G. Yi, H. Jang, S. Hong, and T. Joo, *Applied Physics Letters* **80**, 1924 (2002).

[23] C. Ahn, S. Mohanta, N. Lee, and H. Cho, *Applied Physics Letters* **94**, 261904 (2009).

[24] D. Vogel, P. Kruger, and J. Pollmann, *Physical Review* B **52**, 14316 (1995).

[25] D. Look, D. Reynolds, C. Litton, R. Jones, D. Eason, and G. Cantwell, *Applied Physics Letters* **81**, 1830 (2002).

[26] H. Kang, B. Du Ahn, J. Kim, G. Kim, S. Lim, H. Chang, and S. Lee, *Applied Physics Letters* **88**, 3, 202108 (2006).

[27] B Meyer, H. Alves, D. Hofmann, W. Kriegseis, D. Forster, F. Bertram, J. Christen, A. Hoffmann, M. Strassburg, M. Dworzak, U. Haboeck, and A. Rodina, *Physica Status Solidi B-Basic Solid State Physics* **241**, 231 (2004).

[28] C. Jagadish and S. Pearton, *Zinc Oxide Bulk, Thin Films and Nanostructures: Processing, Properties and Applications*, (UK, Elsevier, 1-5, 2006).

[29] A. Janotti and C. Van de Walle, *Physical Review* B **76**, 22, 165202 (2007).

Chapter 3 **Experimental Methods and Techniques**

3.1 Introduction

The experimental techniques employed throughout this thesis will be discussed in this chapter. This includes a description of the preparation of bulk targets, preparation of thin films by Pulsed Laser Deposition (PLD) and film thickness measurements by a *Dektak* surface profiler. The following techniques were used to characterise and investigate the structural properties of the thin films: X-Ray Diffraction (XRD), Raman Spectroscopy, X-Ray Absorption Near Edge Structure (XANES) and Extended X-Ray Absorption Fine Structure (EXAFS). Superconducting Quantum Interference Device (SQUID) magnetometry and Magnetic Circular Dichroism (MCD) were used to investigate the magnetic properties of the samples.

Most samples were produced in our lab at the University of Sheffield, but some other samples were produced by our collaborators, who will be acknowledged later. All of the SQUID and MCD measurements for the films were performed in Sheffield, while other measurements *i.e.* XANES and EXAFS were performed in the USA. Some XRD and Raman spectra measurements were measured in Sheffield while others were measured in China. All the techniques, mentioned above, will now be discussed in detail.

3.2 Thin Films Growth Techniques

3.2.1 Pulsed Laser Deposition (PLD)

Several techniques may be used to generate thin films, these include molecular beam epitaxy (MBE) [1-6], chemical vapour deposition [7] and reactive sputtering [8,9]. PLD is an extremely adaptable technique for producing a wide range of thin films and multilayer systems. Thin films of almost any material can be grown by focusing a pulsed laser beam onto a target and then collecting the ejected material on a suitably positioned heated substrate [10-18].

Among its many advantages, and one of the reasons for its major acceptance among scientists, is the relatively small start-up cost of PLD research. For example, PLD can be used to generate films of good quality which are comparable to those produced by MBE, but at 1/10th of the cost. Furthermore, the energy source (laser) is positioned outside the deposition system, which results in a very clean process and considerable freedom in the ablation geometry is possible. Finally, the deposition parameters such as the substrate temperature, chamber pressure, and gas environment can be easily controlled during the film ablation [19].

In contrast, one of the major drawbacks of growing thin films by laser ablation is splashing. Splashing occurs when sub-micron sized particles are ejected from the target and become lodged in the surface of the film. This is due to the rapid vaporisation of the liquid layer at the target's surface, formed by the laser.

3.2.1.1 Target Fabrication

A target is needed in order to make the films. The target is a homogeneous solid, with a high density and should be free from surface cracks. To produce the targets the standard solid-state reaction technique was used. The appropriate component powders were bought from *Alfa Aesar* and had a purity of 99.99%. An electrical balance was used to measure the precise stoichiometric quantity of the target components required. These powders were then mixed and ground with a mortar and pestle for no less than 25 minutes. This step was essential to ensure good mixing of all components. A high-quality alumina crucible was used to contain the powder for the annealing process. The powder was annealed for 12 hours at 300^o C in air, in a furnace. These powders were then remixed in the mortar and pestle for 25 minutes and reannealed for 12 hours at a higher temperature of 600^o C. The powder mixture was again re-ground and reannealed for 12 hours at 900^o C. Repeatedly increasing the temperature, sintering and grinding were essential, not only to make the desired oxide component but also to eliminate the impurity phases of un-reacted powders.

A commercial *Specac* die of internal diameter 25 mm was used in conjunction with a manual, hydraulic bench-press; this was to enable the powder to be compressed to a pressure of 25 kPa. This was a necessary step to produce a dense cylindrical pellet with a 25 mm diameter and 5 mm thickness. This pellet was then finally sintered at 900^o C for 13 hours in order to produce a target with a smooth surface. By using this method, the target would have high density and therefore would be ideal for ablation. Each prepared target was then affixed to a holder using a UHU glue, for use in the PLD chamber. The whole process of preparing a single target can take up to 4 days to complete. All targets that were made in Sheffield used this method; this includes ZnO films and ZnO films doped with Co, CoO, and Co_3O_4 targets as shown in Chapter 6. All the films were deposited on a sapphire substrate, see Section 3.6.

3.2.1.2 PLD Set-up and Procedure

The PLD system, shown in Fig 3.1, comprises of three major components: the deposition chamber, the vacuum system, and the laser. A high-powered laser Lambda Physik Lextra 200 xenon chloride (XeCl) which is a mixture of various gases typically: 0.56% HCl, 2.48% Xe, 48.48% He and 48.48% Ne. This excimer laser operates at a wavelength of 308 nm. The optical pulse length, full width at half maximum (FWHM) was 28 ns. The laser produces a pulse energy of up to 400 mJ, at a repetition rate of 10 Hz. The laser beam is focussed onto the target using a convex quartz lens, mounted on a rail.

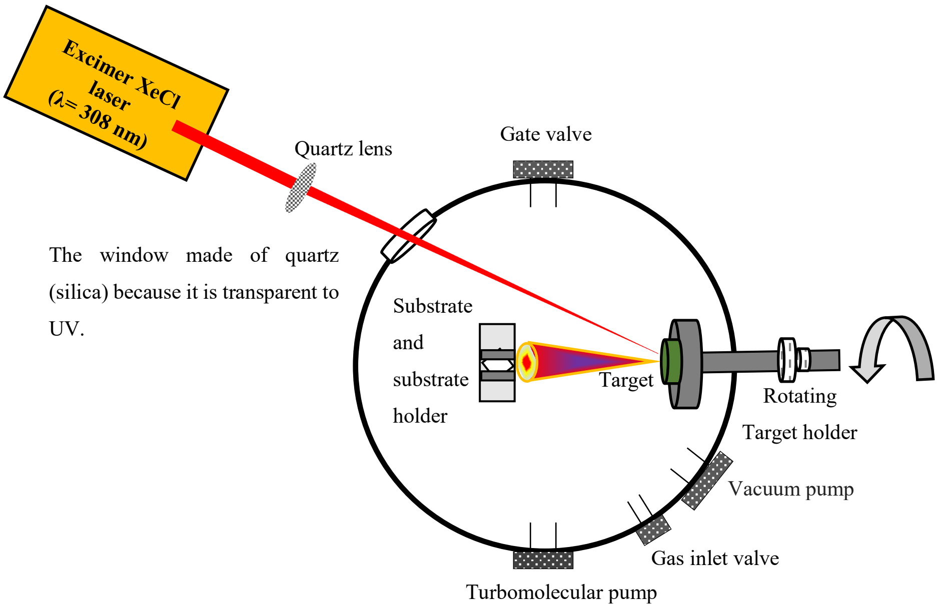

The window made of quartz (silica) because it is transparent to UV.

Figure 3.1: Schematic diagram of the PLD system.

The beam is focussed onto the target inside the chamber. This can be managed by sliding the lens along the rail and varying the distance between the lens and the quartz window of the ablation chamber. A rectangular cardboard aperture, positioned in front of the chamber-window, blocks out the non-uniform part of the beam. The incident beam, angled at approximately 45 degrees, creates a spot around 3 mm in diameter on the target surface. This procedure is first performed using a HeNe visible laser as a guide, to ensure the ablation beam hits the target correctly.

The deposition chamber is made of stainless steel. It can be pumped down to a base pressure of ~10^{-5} Torr, using a turbo-molecular pump (TMP). The chamber contained a substrate holder, target holder and a pressure-gauge unit. The target holder was connected to an electric motor that rotates the target at a speed of 60 rpm. This regular rotation not only prevented over-ablation of the same spot on the target but also yields good film uniformity. In other words, regular rotation reduces the likelihood of splashing. The substrate holder was located perpendicular to the target at a fixed distance of ~ 3.5 cm.

The usual procedure was to pump down the chamber to its base pressure using a rotary pump, then any gas, usually oxygen in our work, can be bled into the chamber to obtain the required pressure. This pressure could be controlled by balancing valves: oxygen inlet-valve aperture, and a gate-valve sitting directly above the TMP. The pressure control unit made by *MKS Instruments* was used to control the flow of the gas in the chamber.

The substrate used for the thin films was sapphire, Al_2O_3; which will be discussed in detail in Section 3.6. The sapphire substrate was cleaned in an ultrasonic bath using acetone and then attached to the substrate holder, which was also cleaned with acetone, to ensure no deposition traces remain from the previous run.

Inside the chamber, the substrate-holder consisted of two thin stainless-steel plates clamped together, with two commercial electric heater-elements sandwiched between them. These heater-elements were connected to a DC power supply, allowing temperatures of up to 600°C to be achieved. During the ablation process, the temperature of the substrate was measured using a chromel-alumel thermocouple attached to the substrate heater, which was controlled by the power supply. The substrate was attached to the holder and covered partially by two small brass clamps on two corners. This allowed two deposition-free areas on the edges of the blank substrate which were used as a starting point (or reference) when measuring the film thickness, see Fig 3.2.

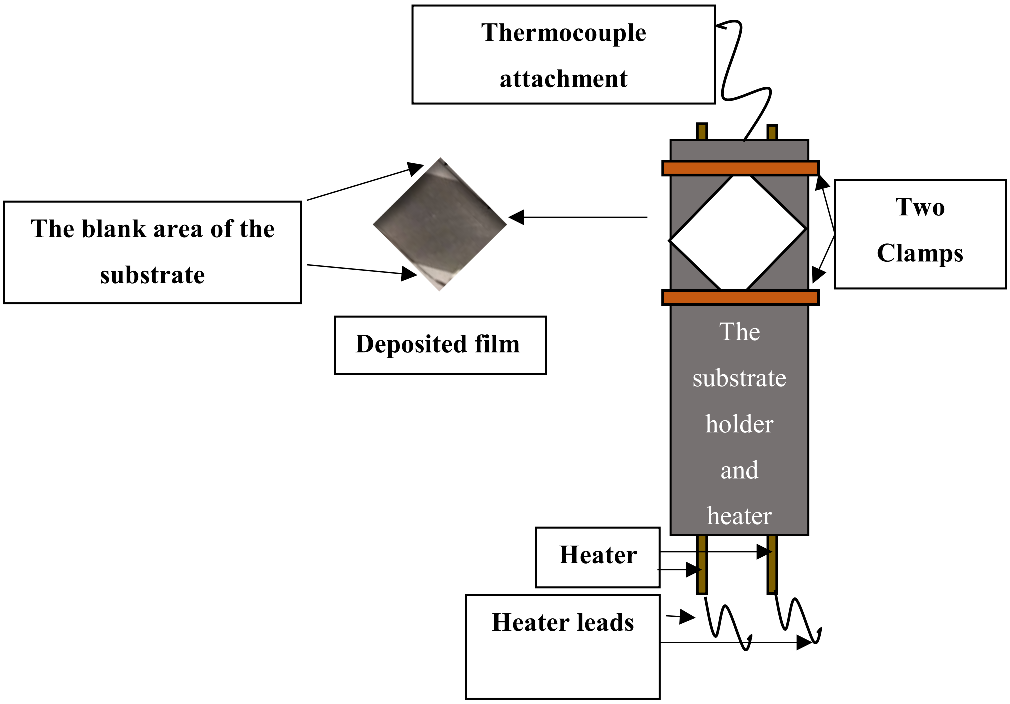

Figure 3.2: Schematic diagram of the substrate holder with a picture of the deposited films depicting the free area of the film.

After placing the target and the substrate inside the chamber, the deposition chamber was tightly-sealed, closed, and evacuated. The laser was then switched on after the desired substrate temperature and chamber pressure had been attained. The film was then deposited for a period of time, which is determined by the film thickness ultimately required. The incident beam from the laser hits the target at an angle and the subsequent plume is then directed perpendicular to the surface of the substrate as shown in Fig 3.1

During the ablation, the energy of the laser beam created a plasma plume from the surface of the target. This means that the atoms, molecules and ions were transferred from the target to the substrate. The control parameters such as substrate temperature, gas pressure, and deposition time were tuned to improve the characteristics of the film. These conditions were measured continuously every five minutes and ideally should remain constant throughout the film deposition. Films were deposited under different oxygen pressures will be discussed in Chapter 6.

The laser plume has different shapes depending on the deposition pressure in the chamber as illustrated in Fig 3.3. The shape of plume varies due to the chemical interactions between the deposited species and the oxygen in the chamber [20,21]. The deposition time at base pressure is reduced, compared to the deposition time in oxygen, for films of equal thickness as the amount of ablated material reaching the target is reduced.

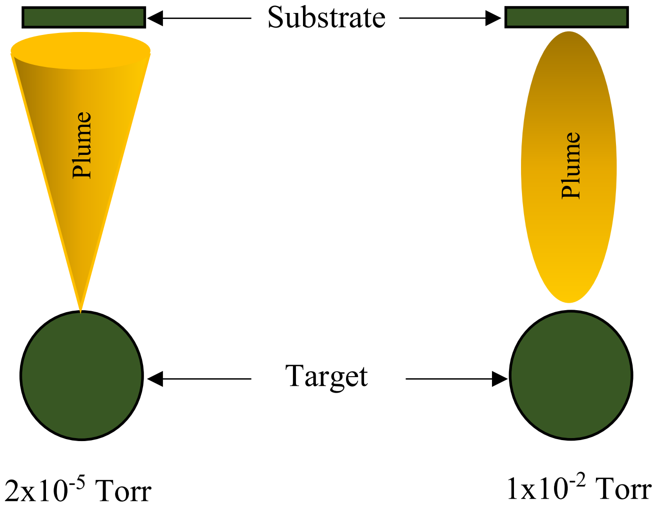

Figure 3.3: Sketches depicting the plume, from the laser beam strikes, during the ablation procedure at two different pressures; base pressure oxygen pressure.

After ablating the film, the film is left inside the chamber to cool down until it reaches room temperature before venting the chamber to atmospheric pressure. Typically, dry nitrogen was utilised to vent the chamber to atmospheric pressure in order to avoid undesired contamination and so that water vapour and other contaminants were prevented from being absorbed by the vessel wall. Finally, the chamber-lid can be released and the sample can be removed for further measurements.

3.2.2 Molecular Beam Epitaxy (MBE)

Molecular Beam Epitaxy is a technique that can be used to produce compound semiconductor materials. It is most often used for the growth of very thinly layered films (Epitaxy). It is a straightforward technique which works by directing multiple beams of atoms, that are generated with effusion-cells, onto a heated crystal surface or substrate. The effusion-cell contains a heated crucible, that contains the materials, which are evaporated to create an angular distribution of atoms in the beam [1-3,5,22,23]. It is highly recommended that the substrate is continuously rotated in order to enhance the growth homogeneity.

An ultra-high vacuum (UHV) chamber enables pressures of the order of 10^{-10} Torr to be reached and is an essential part of the MBE process. It provides an extremely clean environment and prevents any contamination in the surface growth-layer from atmospheric molecules [5]. One of the main advantages of the MBE technique is the high-quality production/growth of thin films of elements and compounds. However, MBE requires a lower rate of film deposition and subsequently takes a longer time to achieve the same results as PLD; e.g. a typical rate for MBE is 3Å/s compared to 10Å/s for PLD [24]. MBE is expensive and not suitable for industry because it is too slow and high throughput is essential. For research, it is useful because one needs to control precisely the deposition of each film. MBE thin films, investigated in the present work, were grown by Dr Zengxia Mei at the Beijing National Laboratory for Condensed Matter Physics, Institute of Physics, Chinese Academy of Sciences.

3.2.3 Ion Implantation

Ion Implantation is fundamentally a surface or near-surface technique by which ions are implanted into a solid material. This process results in a change in the physical surface properties. The technique includes an ion source, an accelerator, and a target. The depth of penetration of the ions in the solid depends on the accelerated energy and the ion implanted [25]. The film’s properties are changed during the ion implantation process because the sample becomes damaged and defects are created.

The Ion Implantation technique uses an accelerator to provide ions with typical high kinetic energy ranging up to ~500 KeV using a high electric field. As a result, the ions can penetrate the target up to depths varying from nanometres to tens of micrometres [25,26]. The precise dose of the ions and the accelerated energy of the implantation is calculated using the Stopping and Range of Ions in Matter (SRIM) programme in order to optimise implantation depth. The disadvantage of Ion Implantation is that it is an expensive and complicated technique. Ion Implantation was used by two of our collaborators: Dr Minju Ying at the College of Nuclear Science and Technology, Beijing Normal University, Beijing, China, and Dr Nianhua Peng at the Surrey Ion Beam Centre, University of Surrey, Guildford GU2 7XH, Surrey, UK.

3.2.4 *Dektak* Surface Profiler

The thickness of films deposited in Sheffield were measured with a *Veeco Dektak* profilometer (Model 150) which uses a diamond-tipped stylus profiler. The *Dektak* is capable of measuring film thicknesses in the range of 50 to 900 nm. In order to measure a film's profile, the stylus of the *Dektak* moves over the surface of the film collecting data on the surface topography [27]. Also, the micrometre screw alters the height of the stylus to adjust its position on the sample. The blank areas of the two corners generated at the film deposition stage are ideal to use as a reference in the measurement of the film's thickness as shown in Fig 3.4 by the red and green bands respectively. The thickness of the film increases when the deposition time increases as shown in Fig 3.5.

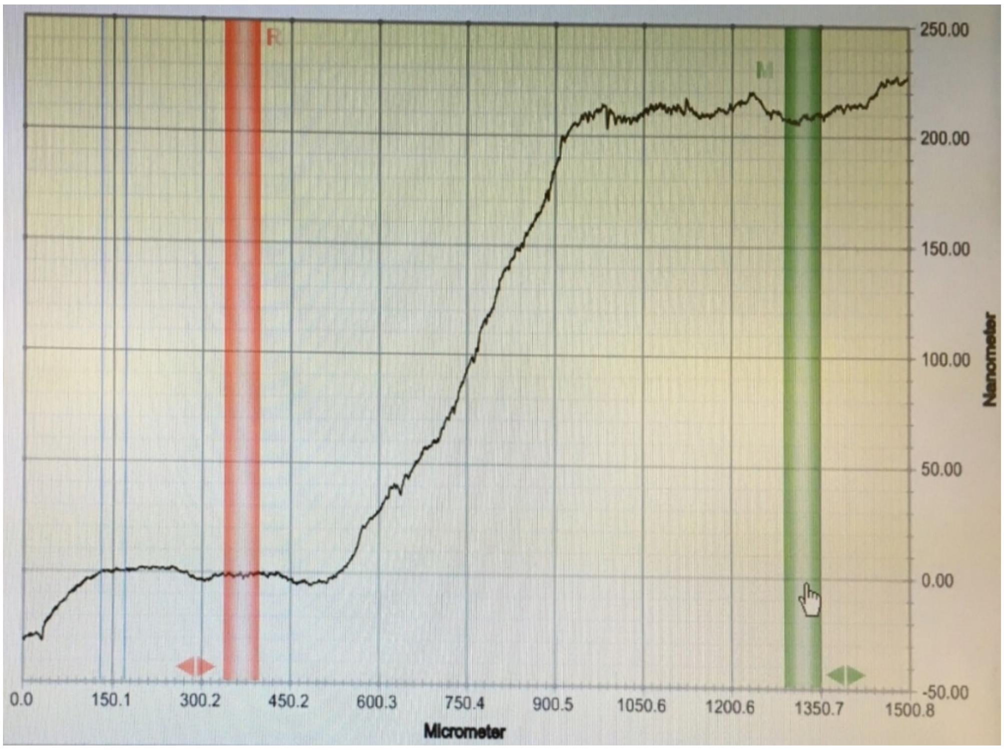

Figure 3.4: Thickness of pure ZnO thin films, grown on a sapphire substrate as measured by *the Dektak* surface profiler.

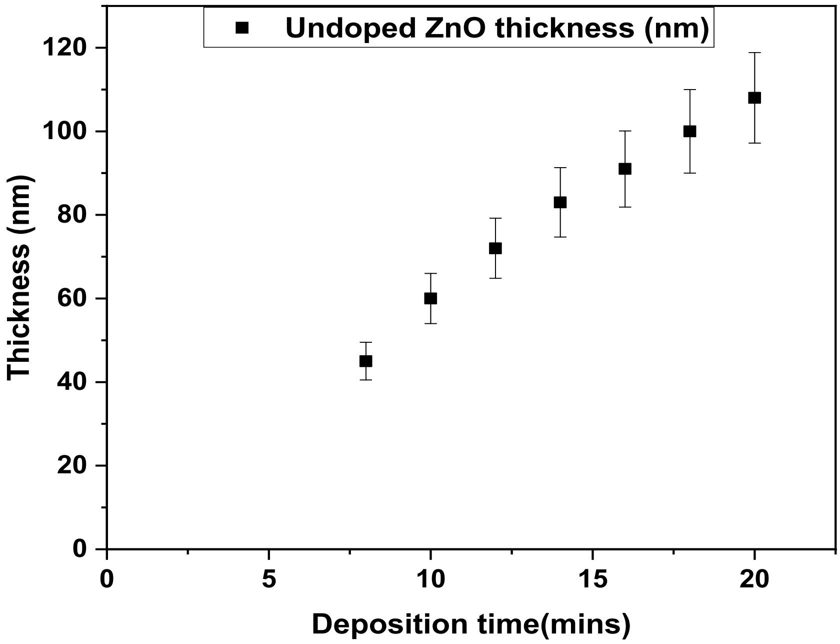

Figure 3.5: Thicknesses of pure ZnO thin films grown on sapphire substrates at base pressure as a function of deposition time at a fixed substrate temperature of 450 ˚C , Error bars of 10 % is shown on the data points.

3.3 Structural Measurements

3.3.1 X-Ray Diffraction Measurement (XRD)

XRD is a powerful technique for determining the crystallographic symmetry of the sample produced. The X-ray beam is incident on the film, creating interactions between the electric field of the X-ray and the electron cores of the atom. The reflected beams are collected and the lattice spacing can be calculated using Bragg's law:

$$n\,\lambda = 2d\sin\theta \tag{3.1}$$

Here, d is the spacing between planes, n is an integer, λ is the wavelength of the incident X-ray beam and θ is the angle of diffraction. Many X-ray geometries exist and in the present work the θ-2θ geometry was used, such that the X-ray tube remains in the same position throughout and the sample then moves through the angle θ while simultaneously the detector travels through an angle 2θ. The angle θ is the angle of both the incoming electromagnetic wave and the diffracted electromagnetic wave with regard to the Bragg planes. Thus, the electromagnetic wave changes totally by 2θ as shown in Fig 3.6.

According to Bragg's law, the XRD is varied as spacing and the crystallography states that the spacing between planes for a cubic lattice is given by the equation:

$$d = \frac{a}{\sqrt{h^2+k^2+l^2}} \tag{3.3}$$

where a is the lattice constant and (h, k, l) are the Miller indices for the crystalline lattice. The Miller indices determine the plane orientation in the crystal with lattice constants (a,b, and c). However, for a hexagonal lattice, ZnO for example, with constants a and c,

$$d_{hkl} = \frac{a}{\sqrt{\frac{4}{3}\ (h^2+k^2+hk)+(\frac{a}{c})^2\ l^2}} \tag{3.4}$$

Our thin films (ZnO) have a textured structure and are highly oriented with the c-axis perpendicular to the plane of the sapphire substrate. Therefore, the only reflection can be seen as the following:

$$d_{002} = \frac{a}{\sqrt{(\frac{a}{c})^2\ l^2}} = \frac{c}{2} \tag{3.5}$$

$$\mathrm{d}_{004} = \frac{c}{4} \tag{3.6}$$

Most of the samples were measured at the University of Sheffield using a *Bruker D2* X-ray diffractometer device. The device contained a Cu target and produced two main wavelengths of radiation, CuK_{α} and CuK_{β}. The CuK_{β} wavelength has a much lower intensity, which results in a weak signal-to-noise ratio, when used as the mainline.

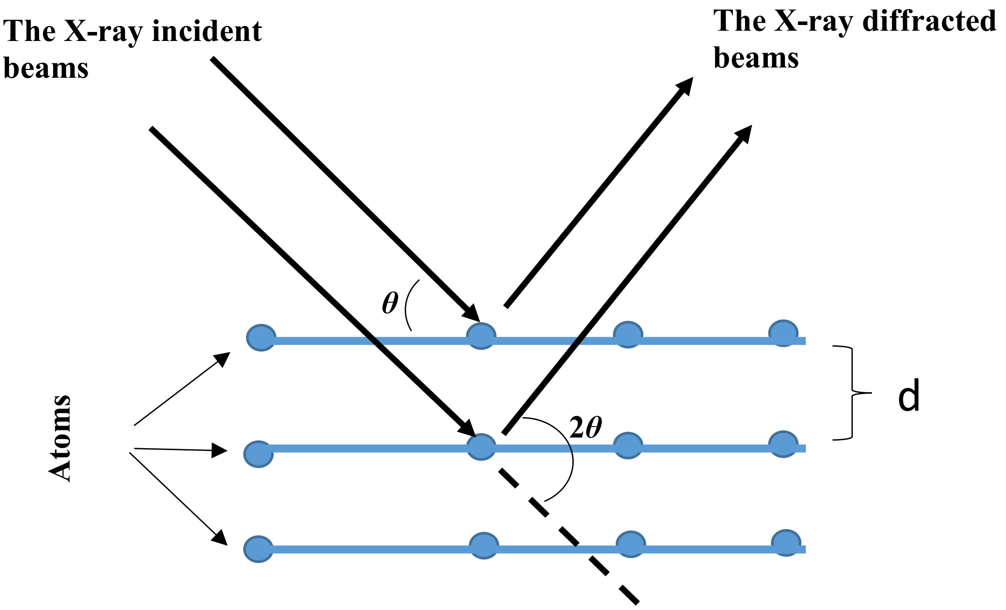

Figure 3.6: Diagrammatic sketch of X-ray interactions with atoms.

However, the CuK$_\alpha$ intensity is higher than CuK$_\beta$, so the latter can be removed by a filter that is inserted into the exit beam. CuK$_\alpha$ radiation was produced at a wavelength of 1.5406 Å and is useful in this case for determining the inter-planar spacing and results in a better XRD pattern.

A θ-2θ plot was used, and measurements were taken in the range $20° \leq 2\theta \leq 80°$ and processed using the *Diffrac* software. The Debye-Scherrer equation determines the size of the particles that give rise to the observed XRD peak [29, 30]:

$$D = \frac{K\lambda}{\beta \cos \Theta} \tag{3.7}$$

Where D is the grain size, β is the full width at half maximum (FWHM) which is expression used to describe the width of a line shape at of its half of its maximum amplitude, λ is the X-ray wavelength, K is a constant related to crystallite shape and is usually given by = 0.94, and θ is the diffraction angle = ($2\theta/2$) [29,30].

3.3.2 Raman Spectroscopy

The fundamental operating procedure of Raman Spectroscopy is reliant on the inelastic scattering of an intense source of monochromatic light, such as that produced by a laser beam incident on a sample. The experiments used in this work focus on lattice vibrations (phonons)[28]. The Raman shift is normally plotted in wavenumber as the following: $1/\lambda = v/c$, where the frequency $1/\lambda$ = cm^{-1}. In a standard spectrum, the Raman shift is most often expressed as a function of the incident light intensity. The difference between the frequency of the scattered light and the incident laser beam is the Raman shift.

Rayleigh scattering occurs when there is no change in frequency between the incident and scattered light after the interaction between the light and material as shown in Fig 3.7 (a). When the incident light interacts with the material, the material vibrates leading to inelastically scattered light [28-30]. The absorption of a photon from a crystalline solid takes place in a virtual excited state and with no delay, a different photon is emitted at a different wavelength. A red-shifted Stokes photon is illustrated in Fig 3.7 (b) which shows that the energy decreases relative to the interaction of the incoming light with that of the material. An anti-Stokes blue-shifted photon, depicted in Fig 3.7 (c), shows that the energy increases relative to the interaction of the incoming light with the material. This increase is proportional to the energies of the vibrational levels in the material. In short, the vibration energy level of the phonon corresponds to the difference in frequency between the incident and scattered photons [28-31].

. The main benefit of Raman Spectroscopy is that it provides information on the film’s structural properties, such as lattice dynamics as discussed in Subsection 2.7.4. In order to achieve this, the Raman signals are analysed with respect to several factors, these include the frequency shift, intensity, width and line-shape in the spectrum. This is particularly important when one investigates the deposited films by ion implantation and relates Raman spectra to the various features such as point defects, extended defects, surfaces and amorphous materials as discussed in chapter 4 and 5.

Removed

by the author

for copyright reasons

Figure 3.7: Energy level diagram of Raman scattering; (**a**) Rayleigh scattering (**b**) Stokes scattering, (**c**) anti-Stokes scattering.

According to the selection rules for energy conservation, the generated or annihilated elementary excitation energy is equal to that of the transferred energy.

The phonon generation (Stokes process):

$$\hbar\omega_i - \hbar\omega_s = \hbar\Omega_s \tag{3.8}$$

where ω_i and ω_s are the frequencies of the incident and scattered light respectively.

The phonon annihilation (anti-Stokes process):

$$\hbar\omega_s - \hbar\omega_i = \hbar\Omega_s \tag{3.9}$$

Where Ω_s is the frequency of the phonon. The frequency of the incident light is much higher than that of the scattered excitation. Therefore, the difference between the two frequencies is small as shown below:

$$\omega_i >> \Omega_s \Rightarrow \omega_i \sim \omega_s \tag{3.10}$$

Another selection rule is correlated to the conservation of the quasi-momentum; this momentum includes the wave-vectors of the incident light ($\boldsymbol{k}_i$) and scattered light ($\boldsymbol{k}_s$), and the elementary excitation ($\boldsymbol{q}_j$). The phonon generation (Stokes process):

$$\boldsymbol{k}_i - \boldsymbol{k}_s = \boldsymbol{q}_j \tag{3.11}$$

and the phonon annihilation (anti-Stokes process):

$$\boldsymbol{k}_s - \boldsymbol{k}_i = \boldsymbol{q}_j \tag{3.12}$$

The wavelength of the incident radiation light, $\lambda_i \sim 500$ nm = 5000 Å is much larger than the lattice constant of the crystal, $a_0 \sim 3$Å. As a result, k_i, k_s, and q_j are much smaller, compared with the Brillouin zone boundary $Q = 2\pi/a_0$ and wave vector $k = 2\pi/\lambda$ thus $k << Q$ and $\boldsymbol{q}_j << Q$. When the wave vector of the light is minimal, the Raman scattering for ZnO is only observed at $\Gamma = 0$, as shown in Fig 3.8.

A phonon dispersion relation (PDR) reflects the lattice dynamics of a solid, where the energy of a lattice vibration is plotted as a function of its wave-vector, along the high-symmetry direction of the crystal. When all the states in the PDR were integrated over the Brillouin zone energy, this generates the phonon density of states (PDOS) as shown in Fig 3.8 (a).

Raman Spectroscopy was performed using a *Renishaw Raman Microscope* system to measure most of the Raman scattering data for our ZnO samples, an example of the Raman spectrum of an undoped ZnO thin film is shown in Fig 3.8 (b). These peaks are discussed in details in chapter 4 and 5. The laser has a wavelength of 514.5 nm (green) and a power of up to 25 mW and is focused onto a ~ 2 μm spot, with z(xx)**z** scattering geometry.

Removed

by the author

for copyright reasons

Figure 3.8: Phonon dispersion relation resulting from the wurtzite ZnO structure as taken from [32]. The frequency values are represented by the energy of phonon wurtzite modes which are graphed against their wavevector along with the directions of the crystal which are highly-symmetric. Experimental data points from Raman scattering [33] and inelastic neutron scattering [34,35] are inserted as red diamonds and black circles, respectively. On the right side, the one-phonon density of states is labelled (**a**).

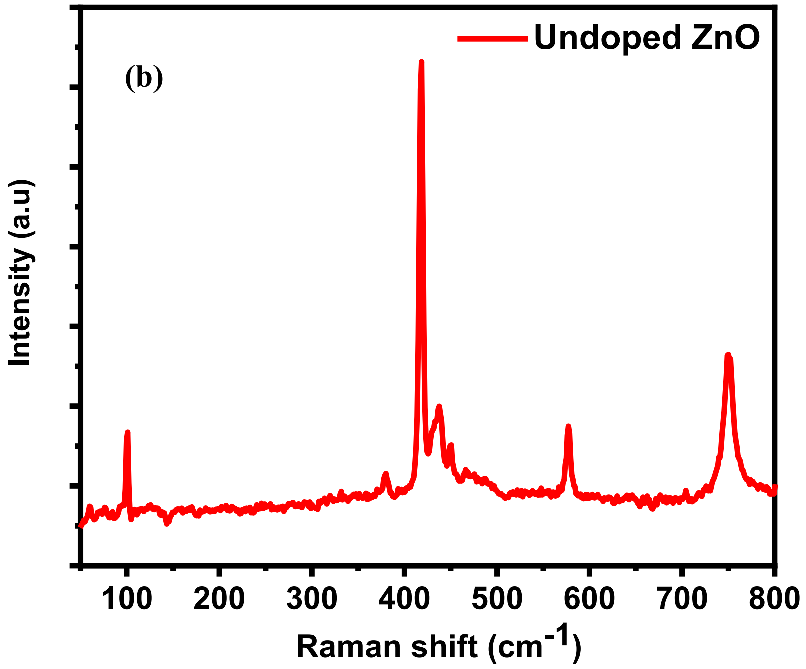

Figure 3.8: (**b**) Raman spectra measurements for an undoped ZnO film.

3.3.3 X-Ray Absorption Fine Structure (XAFS), X-Ray Near Edge Structure (XANES) and Extended X-Ray Absorption Fine Structure (EXAFS)

XAFS is a crucial technique for use in understanding the electronic structure of atoms or ions in a given sample. It aims to provide information about the local geometry surrounding the core of an atom. This is achieved when x-rays are absorbed by an atom at various energies near and above the core-level binding energy of the atom. XAFS spectra can be used to measure all elements present in crystals and in highly disordered materials. As a result, XAFS can detect any secondary phases which are present in the sample [36-40].

The X-ray incident on the sample is scattered, but when a photon excites an electron from an inner to an outer shell, the absorption exhibits a sharp peak. This is because the absorbing atom is excited to an unoccupied state.

This leads to the production of a photo-electron. The intensity of the beam passing through the sample, $I(x)$ can be expressed as

$$I(x) = I_0 \, e^{-\mu x} \tag{3.13}$$

where x is the sample thickness, I_0 is the intensity of the incident beam and μ is the linear absorption coefficient which depends on the material and incident photon energy.

The XAFS absorption spectrum contains three essential parts: pre-edge, X-Ray Near Edge Structure (XANES), and X-Ray Absorption Fine Structure (EXAFS). These components provide relevant data for the electronic structure of the sample, as illustrated in Fig 3.9. The oxidation state of the absorption atoms is found using XANES, whereas EXAFS finds information on the neighbouring species. The near edge allows one to detect Co^0, which is a metal ion, as it has low ionisation energy compared to Co^{2+} and Co^{3+} ions which have higher energy. The absorption arises when an incident photon with sufficient energy excites the inner electron; this moves an electron up into the conduction band creating a photoelectron.

XANES and EXAFS spectra have unique standard data for known samples, and these are used as calibration. The data from the unknown sample is then compared to the linear combination of the known sample. The XANES and EXAFS measurements are both sensitive to secondary phases [39].

All the X-ray absorption data provided in this thesis were measured and analysed by Dr Steve Heald at beamline 20-BM at the *Advanced Photon Source* in the *Argonne National Lab*, IL, USA, and then analysed using the *Athena* analysis program.

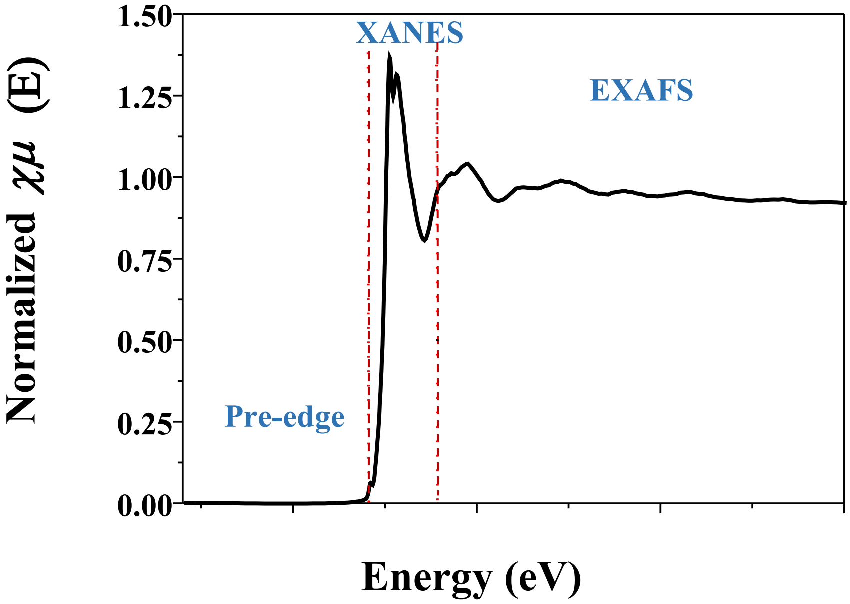

Figure 3.9: The three important regions of XAFS, which are identified as pre-edge, XANES and EXAFS respectively.

3.4 Magneto-Optics Measurement

3.4.1 Magnetic Circular Dichroism Spectroscopy (MCD)

The phenomena of Magneto-Optics (MO) occurs when a polarised plane wave of light interacts with a magnetic sample. It is a powerful technique used for the spectroscopic identification of the origin of ferromagnetism in materials. MCD is a robust method used to study the electronic states involved in magnetisation processes [41]. The behaviour of the magnetic states of the material is investigated by evaluating the properties of the circularly polarised light travelling through the material [6,42].

3.4.1.1 Background Theory

The light beam propagates through a transparent material such that its speed is reduced by the refractive index n. The refractive index, n, is the ratio of the speed of light c, to the velocity of light in a medium V, and is given by the following:

$$n = \frac{c}{V} \qquad (3.14)$$

When light propagates through an absorbing medium, the optical properties can be expressed by the complex refractive index, $\tilde{n}$, which is defined as follows:

$$\tilde{n} = n + i\kappa \qquad (3.15)$$

where $\tilde{n}$ is the sum of both the real refractive index n and the imaginary extinction coefficient κ. This shows the relation between the imaginary component and the absorption coefficient. This is obtained from the electric field, *E,* of a wave propagating via a medium in the z-direction of the light, which can be written as the following:

$$E(z, t) = E_0 \, e^{i(qz - \omega t)} \tag{3.16}$$

Here q is the wavenumber of the light and ω is the angular frequency, which is related to the refractive index as the following:

$$q = \frac{\omega \tilde{n}}{c} = (n + i\kappa) \frac{\omega}{c} \tag{3.17}$$

If equation 3.17 is substituted into equation 3.16, exponential decay of the wave can be seen in the medium, where α is the absorption coefficient.

$$I(z) = I_0 \, e^{-\alpha z} \tag{3.18}$$

I is the intensity and $I \alpha |E|^2$

The absorption coefficient, α, is related to the extinction coefficient κ, by the following formula:

$$\alpha = \frac{2\kappa\omega}{c} = \frac{4\pi\kappa}{\lambda} \tag{3.19}$$

where λ is the wavelength of light in *vacuo* [43].

Linearly polarised light can be expressed in two parts by considering the equivalent combinations of left circularly polarised light (LCP) and right circularly polarised light (RCP) when both components are passing through a medium.

In a magnetic medium, $\tilde{n}$ depends on the polarisation of light and thus equation 3.15 becomes:

$$\tilde{n}_{\pm} = n_{\pm} + i\kappa_{\pm} \tag{3.20}$$

Where the negative sign (-) represents the LCP, the positive sign (+) represents the RCP.

The Magneto-Optical effect (MO) is achieved when LCP and RCP light reconnect when travelling via the magnetic medium. LCP and RCP light components are absorbed in different quantities because the refractive indices of both components are not equal ($\tilde{n}_+ \neq \tilde{n}_-$), and these differences result in a phase and amplitude shift in LCP and RCP components [44-46] as shown in Fig 3.10. It can be seen from Fig 3.10 (b) that the angle θ rotates and is accompanied by a change in light intensity resulting in elliptically polarised light. When the phase lag in transmission and the attenuation both differ from LCP and RCP light, the combined result is elliptically polarised light. This type of elliptically polarised light and the rotation of circularly polarised light causes the Faraday effect along with MCD. The Faraday rotation effect is given as the difference between the refractive indices of the LCP and RCP components, which is described by the following:

$$\theta_F = \frac{\omega l}{2c}(\Delta n) = \frac{\omega l}{2c}(n_+ - n_-) \tag{3.21}$$

Here c represents the speed of light and l is the thickness of the magnetic film. However, the differences in the extinction coefficients, κ_- and κ_+ , causes the RCP and LCP to differ at frequency ω, resulting in elliptically polarised light and MCD is given by the following:

$$\text{MCD} = \frac{\omega l}{2c}(\Delta k) = \frac{\omega l}{2c}(\kappa_+ - \kappa_-) \tag{3.22}$$

Equation 3.22 indicates that MCD depends on the transitions at ω, where the medium is absorbing. Thus, MCD is a useful technique which may be used to define the structural magnetic state of the observing material [47]. MCD is mainly concentrated on in this work.

Removed
by the author
for copyright reasons

Figure 3.10: (**a**) The equally intense LCP and RCP light produces linearly polarised light. (**b**) If the LCP and RCP components are unequal, then elliptically-polarised light emerges with a different phase and amplitude when they pass through a perpendicularly magnetised thin film taken from [6].

3.4.1.2 Experimental Setup

The MCD setup follows Sato's method which utilises Faraday geometry [6,44] as illustrated in Fig 3.11. This system allows measurements of MCD and Faraday rotation of magnetic materials simultaneously. It also allows us to maintain the measurements at variable wavelengths across the range of the regional spectrum. All of the experiments throughout this thesis are performed in Faraday geometry because all of our films were transparent thin films. Faraday rotation and MCD are measured in radians, where both depend linearly on the thickness and are dimensionless.

For the set up of our measurement, a 150-watt xenon lamp was used to cover the range of energies from 1.5 to 4.5 eV which is associated with a wavelength of 827-276 nm. The light, after being aligned, was passed into a *SpectraPro-275* spectrometer such that a uniform source of monochromatic light is created. The monochromatic light then travels *via* band pass filters, which restrict those wavelengths of light that are undesirable. Then, the light passed via a *Glan Tayler* UV prism polariser in order to maintain the desirable type of plane polarised light before reaching the sample. The UV prism is located at an angle of 90° with respect to the optical axes and at an angle of 45° with respect to the analyser.

The sample was cleaned with acetone before being mounted on the sample holder. The sample holder contained an aperture of diameter ~3 mm. The sample holder was inserted between the poles of an electromagnet. The poles of the electromagnet were capable of producing a magnetic field up to 1.8 T at room temperature, in a direction parallel to the light.

The light beam is reflected through a number of mirrors and the positions of the mirrors must be adjusted and checked regularly such the amount of light transmitted *via* the sample is maximised. The light is directed onto the sample via the aperture in the sample holder.

Then, the light passes through the photoelastic modulator (PEM) device which produces a signal, where polarised light is modulated with a fixed frequency, f [48] and it allows us to use detection methods which provide the ability to measure θ and η simultaneously. The piezoelectric transducer has an applied stress, which induces periodic retardation to change slightly into each of the two components of the transmitted beam that are elliptically polarised. The periodic retardation occurs parallel to that of the vibration direction and may be expressed as $\delta = \delta_0 \sin(2\pi ft)$, where δ_0 and f stand for the retardation amplitude and the frequency modulation, respectively. The birefringent crystal vibrations are directed and set at an angle of 45° to that of the first polariser.

The light passed through an analyser after entering the PEM and being focused into the PMT (Photomultiplier tube) detector. When the sample is magnetic and thus contains a circular polarisation and MCD, the light intensity oscillates with a frequency of either f or $2f$ and exhibits ellipticity and Faraday rotation respectively. On the other hand, when the light intensity at the detector is constant, no MO effect is presented in the sample.

The light intensity signal is converted into an electrical signal when passing via the PMT (*Hamamatsu* H8567-03 Model). The intensity signal produced by the PEM is then passed through an amplifier unit to split the signal components into DC and AC. The DC component I_0, is maintained constant and worked as a reference intensity. This is measured using a *Keithley* voltmeter. In order to obtain the MCD and Faraday rotation respectively, the intensities $I_2(f)$ and $I_3(2f)$ are taken using two lock-in amplifiers.

Figure 3.11: Schematic diagram of the MCD system using Faraday geometry [6].

The MCD and Faraday rotation measurements as derived from the three intensities (I_0, $I_{2(f)}$, and $I_{3(2f)}$) by Sato [44] are:

$$I_1\,(0) = I_0 T\,[1+J_0(\delta_0)\,\sin\,(\Delta\Theta + 2\Phi)] \qquad (3.23)$$

$$I_2\ (f) = I_0\ \Delta T\ J_1\ (\delta_0) \tag{3.24}$$

$$I_3\ (2f) = 2I_0\ T\ J_2\ (\delta_0)\ sin\ (\Delta\Theta + 2\Phi) \tag{3.25}$$

$$\Delta T = t_+^2 - t_-^2 \tag{3.26}$$

$$T = \tfrac{1}{2}\ (t_+^2 + t_-^2) \tag{3.27}$$

Where I_0 is the intensity constant, J_0, J_1, J_2 are zero, first, and second order Bessel functions that determine the optimal photo-elastic modulation and the Bessel functions are proportionate to the light intensity. δ_0 is the retardation amplitude applied by the PEM and $\Delta\Theta$ is the difference between the RCP and LCP of the analyser. Φ is the analyser angle, which is normally set to be zero, and t_+ and t_- are the Fresnel coefficients describing the transmitted RCP and LCP light respectively. From the intensities $I_1\ (0)$, $I_2\ (f)$, and $I_3\ (2f)$, the value of MCD rotation η_F and Faraday rotation Θ_F are derived by Sato [44]:

$$\Theta_F = -\ \tfrac{1}{2}\ \Delta\Theta \tag{3.28}$$

$$\eta_F = \tfrac{1}{4}\ \frac{\Delta T}{T} \tag{3.29}$$

The (I_2/I_1) and (I_3/I_1) ratios can be related to the MCD and Faraday rotation calculations using equations (23), (24) and (25):

$$\frac{I_2\ (f)}{I_1\ (0)} = A\ \ \frac{J_1(\delta_0)\frac{\Delta T}{T}}{1+J_0(\delta_0)\sin(\Delta\Theta+2\Phi)} \tag{3.30}$$

$$\frac{I_3\ (2f)}{I_1\ (0)} = B\ \ \frac{2J_2(\delta_0)\sin(\Delta\Theta+2\Phi)}{1+J_0(\delta_0)\sin(\Delta\Theta+2\Phi)} \tag{3.31}$$

Where A and B are calibration factors, and δ_0 is the amplitude of the retardation applied by the PEM and δ_0 was set at 0.383 to obtain the maximum sensitivity [49]. Where $J_0 = 0$ and J_1, J_2 are near to the maximum at this value.

If $J_0 = 0$, $\Phi = 0$, and $\Delta\Theta$ then equation 3.30 and 3.31 can be written:

$$\frac{I_2\,(f)}{I_1\,(0)} \quad = AJ_1\,(\delta_0)\ \ \frac{\Delta T}{T} \approx \eta F \tag{3.32}$$

$$\frac{I_3\,(2f)}{I_1\,(0)} \quad = BJ_2\,(\delta_0)\ 2\Delta\theta \ \approx \theta F \tag{3.33}$$

3.5 Magnetic Measurement

3.5.1 Superconducting Quantum Interference Device (SQUID)

The SQUID magnetometer is a sensitive instrument to detect the magnetic flux; it can measure minute changes in the magnetic properties of a sample when a magnetic field is present [50]. SQUIDs may be divided into two kinds; the first is called a DC SQUID because it contains two Josephson junctions connected parallel through a superconducting loop. The second type includes only one Josephson junction called radio frequency (RF) SQUID. The RF SQUID is the most frequently used because of the need for only one junction. The SQUID literature with detailed information can be found in references [51-55].

The *Quantum Design* model MPMS-5 Radio Frequency SQUID magnetometer was used to measure all the samples in this thesis. This SQUID is capable of measuring over a wide range of temperatures from 2.2 K to 400 K with a magnetic field ranging from 0-5 T [55]; although the present work was performed mainly in the range 5-300 K and 0-1 T. The SQUID system is shown in Fig 3.12.

Removed

by the author

for copyright reasons

I. Sample Rod
2. Sample Rotator
3. Sample Transport
4. Probe Assembly
5. Helium Level Sensor
6. Superconducting Solenoid
7. Flow Impedance
8. SQUID Capsule with Magnetic Shield
9. Superconducting Pickup Coil
10. Dewar Isolation Cabinet
11. Dewar
12. HP Think Jet Printer
13. Magnet Power Supply
14. Model 1802 Temperature Controller
15. Console Cabinet
16. Power Distribution Unit
17. Model 1822 MPMS Controller
18. Gas Magnet Control Unit
19. HP Vectra Computer
20. Monitor

Figure 3.12: The system components of SQUID taken from [56].

3.5.1.1 SQUID Concept

Direct measurements of the magnetic moment are not possible using the SQUID but instead the voltage induced in the field-sensing coil, from the sample's magnetic response, can be determined. The SQUID magnetometer contains a superconducting magnet that is used to produce the applied magnetic field. The SQUID magnetometer also includes detection coils and a superconducting ring or loop interrupted by a fragile, resistive region; this is a so-called "weak-link" or a single Josephson junction. One side of the superconducting ring is coupled inductively to a field-sensing coil, using superconducting transformers. An RF circuit is then inductively coupled to the other side in order to determine the changes occurring in the superconducting loop [50,51]. This RF circuit oscillates at ~ 20 MHz when it is excited by an RF current.

The SQUID shielding includes the whole of the cryostat which sits inside a large mu-metal cylinder and serves to shield the system from external influences. It is required to protect the SQUID magnetometer, and therefore the sensing coil can detect only the current arising from the magnetic field of a sample. The pick-up sensing coils are wound to form a second-order gradiometer; this consists primarily of two sets of oppositely wound coils, which means that the coils are immune to both uniform and linearly varying magnetic fields.

The superconducting loop is closed and therefore, any change in the magnetic flux produces a current in the loop which must be proportional to the magnetic flux. Hence, the magnetic moment can be determined from the SQUID output voltage. It is then possible to fit the data using a least-squares fitting program and calculate the resulting magnetic moment of the sample, with a simple theoretical expression. Magnetic flux lines penetrate the superconducting loop and fall into discrete levels called fluxons. A fluxon is a quantised multiple of magnetic flux that is given by

$$\Phi_0 = h/2e = 2.1 \times 10^{-15}\,\mathrm{Wb} \tag{3.34}$$

Where 1 $Wb = 1\ T.m^2$; h is Planck's constant and e is the electronic charge. The magnetic field generated by the sample may then be removed, by removal of the sample, which results in entrapment of the magnetic flux. This induces a current in the superconducting loop which circulates indefinitely, without resistance, in order to maintain a constant state of magnetic flux. An indefinitely circulating current may only be sustained if the loop resides at a temperature that is below its superconducting transition temperature; such that the loop remains superconducting.

Since the output voltage is proportional to the magnetic flux flowing through the loop, it must vary sensitively as a periodic function of the flux itself. Effectively, the SQUID becomes a sensitive magnetic flux-to-voltage transducer. By measuring amplitude variations in the output voltage, using sophisticated electronics, the SQUID is able to precisely measure minute changes in the magnetic flux and thus the magnetic moment of the sample in question.

3.5.1.2 Operation

Firstly, the film and substrate were cleaned with acetone in an ultrasonic cleaner for two minutes before being mounted in a transparent drinking straw specifically bought for this purpose. Located on the top of the SQUID system is an air-lock which enabled samples to be removed and placed in the SQUID without contaminating the cryostat with oxygen or other impurities. The straw was attached to the end of a long, thin, stainless-steel rod about 1.5 m in length, with a final section made of brass. The most common sample size was 5 × 5 × 0.3 mm^3. The samples were mounted inside the straw. After inserting the mounted sample through the air-lock, it was positioned in the device's sensing coils. The sample holder was then scanned over a region, 8 cm in length, in order to detect the location of the centre of the sample accurately. When the sample had been detected and subsequently re-positioned, a further, shorter and more accurate, 2 cm scan was performed. This whole process was semi-automated. After the sample had been satisfactorily positioned and the temperature stabilised, a sequence program, which had previously been written, was run.

Two types of SQUID measurements were performed in this work. The first measurement is measuring the moments of a film as a function of an external magnetic field in the range ± 1T over fixed temperature of 5 K or 300 K. For our samples, the magnetisation, M, data obtained is shown in Fig 3.13, where M is plotted as a function of the applied magnetic field thus producing a magnetic hysteresis loop. The raw data shown (black curve) is the hysteresis loop measured at 5 K, for a 5% CoO doped ZnO thin film, before subtraction of the diamagnetic contribution from the sapphire substrate as depicted in Fig 3.13 (a). The data shown in red is obtained from the blank sapphire substrate.

Two different magnetic contributions originated from our deposited film; a linear contribution that was determined in high fields, and saturation ferromagnetic in low fields. The blue dotted lines are the diamagnetic contribution of the sapphire substrate. The ferromagnetic contribution was separated from the diamagnetic one by subtracting the latter from the raw data. The result is a hysteresis loop, which frequently saturates at ~ 3000 Oe. A noticeable linear magnetisation can be fitted above this field.

Another type of magnetisation measurement is to measure the magnetisation behaviour of a sample as a function of temperature in a constant field, the so-called Zero-Field-Cooled (ZFC) and Field-Cooled (FC) measurements. The ZFC measurement procedure begins by setting the magnetic field to zero at room temperature, such that a random orientation of magnetic partiles through the sample is achieved. The sample is then introduced into the cryostat and subsequently cooled to 5 K, where the aligned magnetic moments are frozen.

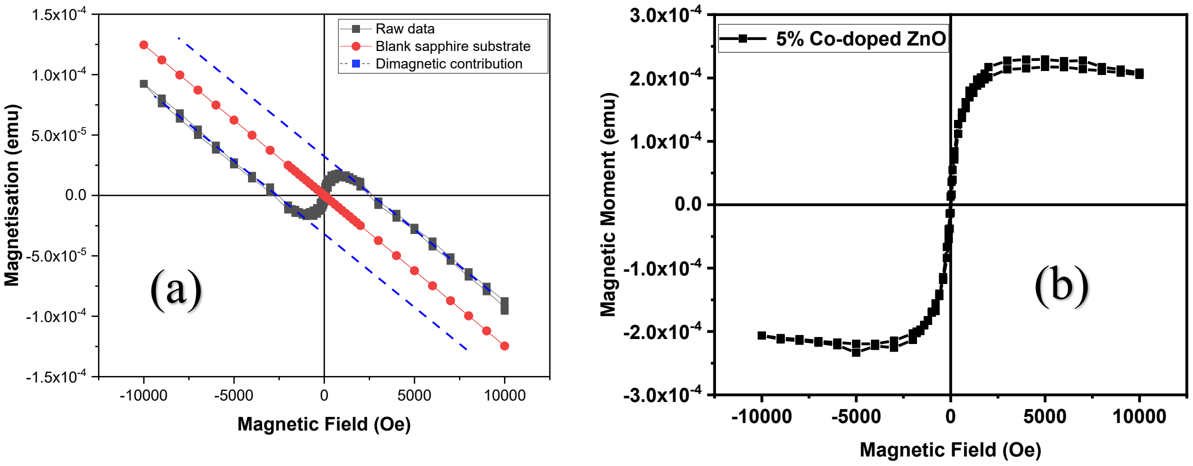

Figure 3.13: (**a**) Raw data from hysteresis loops as measured for both 5% CoO doped ZnO sample taken at 5 K (Gray squares) and a blank sapphire substrate (red circles). (**b**) The resulting ferromagnetic hysteresis loop of a 5% Co-doped ZnO sample after the diamagnetic contribution has been subtracted.

Thus, the alignment is maintained with respect to the direction of the applied field. Then, a small magnetic field of ~ 100 Oe is applied. The sample's moment is then measured as it is slowly warmed up to 350 K. The FC measurement was the reverse of this process; the magnetic moment was measured when the sample cooled down from 350 K to 5 K in the magnetic field of ~100 Oe. Both runs of ZFC and FC measurements are made consecutively in a single run, thus both measurements can be plotted in one graph as shown in Fig 3.14. These measurements provide information about the temperature dependence of the magnetisation along with the magnetic field history.

ZFC-FC measurements can be used to determine the existence and the size of any magnetic nanoparticles, which are dependent on a specified temperature called the blocking temperature T_B. According to the magnetic anisotropy of the material, if no external magnetic field is applied, the alignment of each particle has a tendency to align with the magnetic moment of the easy direction magnetisation. The magnetic moment of uniaxial nanoparticles has two orientations which are antiparallel to each other separated by an energy barrier of size KV. The magnetic nanoparticles are perturbed by the thermal energy, k_BT, and causes them to flip direction at random. If all the nanoparticles were constant in size, then a blocking temperature T_B is present and the magnetic moments of the nanoparticles are frozen with the field direction below this temperature. However, the particles can overcome this energy barrier since the nanoparticles have sufficient thermal energy when $T > T_B$ [59].

The Bean-Livingston equation [57] is used to obtain the particle size as determined from the following equation:

$$25k_BT_B = KV \tag{3.36}$$

Where K is the magnetic anisotropy constant, and V is the particle volume. The period taken for this procedure is called the relaxation time, τ. The assumption of the duration of a typical magnetisation measurement of a particle is 100 Sec [57,58].

ZFC measurement was also used to calculate the magnetic susceptibility, which can be plotted as a function of the temperature in order to determine the Curie's constant when using the Curie-Weiss law, as it is shown in equation 2.28. Fig 3.14 shows ZFC/FC curves (a) for the 5% Co-doped ZnO film grown on a sapphire substrate. The diamagnetic contributions arising from sapphire substrates have been subtracted, and Fig 3.14 (b) shows the ZFC/FC magnetisation of sapphire substrates.

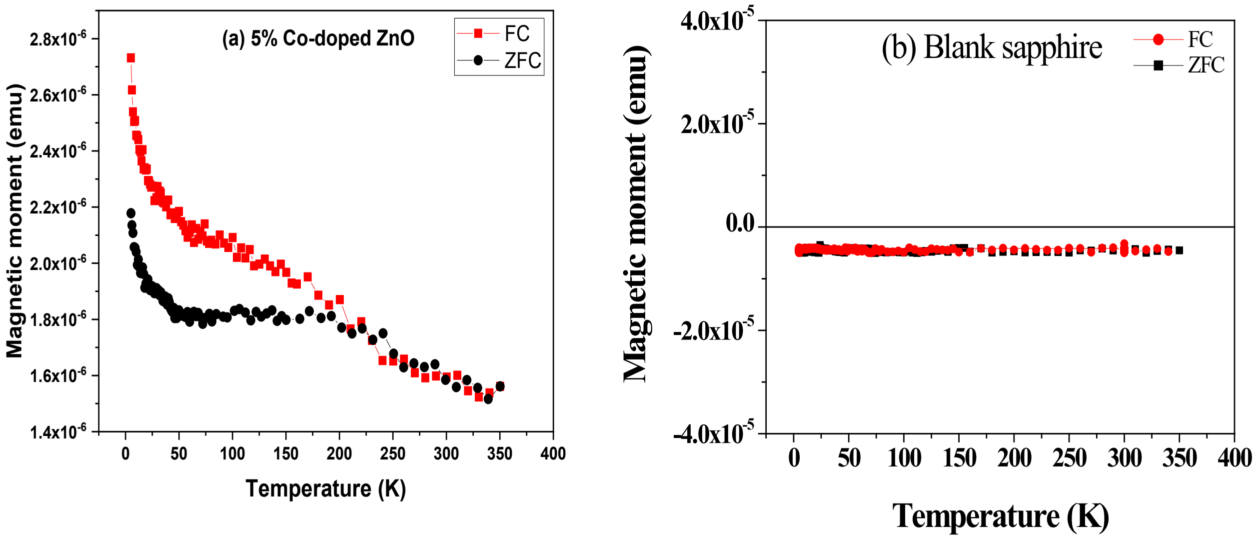

Figure 3.14: (**a**) the ZFC/FC measurements of a 5% Co-doped ZnO film grown on sapphire substrates. (**b**) the ZFC/FC measurements of sapphire substrates.

3.6 Sapphire Substrate

Sapphire (aluminium oxide-Al_2O_3) is a ceramic material which has the crystal structure of both rhombohedral and hexagonal structures with a unit cell volume 84.93 Å^3 and 254.79 Å^3respectively [60,61]. Fig 3.15 shows two different lattice structures of sapphire Al_2O_3. While Sapphire Substrates can be cut in several orientations, the most important ones are *c*, *r*, and *a*, as shown in Fig 3.16. The *c*-plane cut is achieved along [0001] direction, which is the basal plane for hexagonal structure, as shown in Figure 3.16, where the *a*-plane cut is along [11**2**0] direction, and *r*-plane cut is along [1**1**02].

Removed

by the author

for copyright reasons

Figure 3.15: Rhombohedral (**a**) and hexagonal (**b**) sapphire unit cell where the grey atoms are for oxygen and the dark atoms are for Al, taken from reference [61].

Removed

by the author

for copyright reasons

Figure 3.16: Orientation of sapphire planes, taken from [62].

In this thesis, only the c-cut hexagonal Al_2O_3 structure is utilised as a substrate because it is a suitable substrate for wurtzite ZnO, as discussed in Section 2.7. Sapphire is a transparent diamagnetic insulator, is chemically stable and has a density of 3.98 g cm^{-3}. Sapphire is a suitable substrate for use when depositing DMS films because it has a comparable lattice constant, of 4.758 Å, to that of many oxide materials. The advantage of this similarity is that it reduces the strain which originates from the interface created between the deposited film and the substrate itself. Nevertheless, the strain resulting from the small mismatch between substrate and film leads to unpredictable ferromagnetism in some semiconductor materials such as ZnO [63-65]. The above conditions made sapphire a substrate suitable for investigating the origin of the ferromagnetism in deposited thin films.

3.7 References

[1] M. Ilegems, *Crystal Growth in Science and Technology* 359 (1989).

[2] B. Pamplin, *Molecular beam epitaxy* (Elsevier, 2017).

[3] O. Pchelyakov, *Uspekhi Fizicheskikh Nauk* **170**, 993 (2000).

[4] D. Mattox, *Handbook of Physical Vapor Deposition (PVD) Processing*, 237 (2010).

[5] F. Rinaldi, *Niversität Ulm*, 31 (2002).

[6] A. Behan, "*Characterisation of doped ZnO thin films for spintronic applications*", PhD thesis, University of Sheffield (2008).

[7] N. Archer, *Physics in Technology* **10**, 152 (1979).

[8] D. Mattox, *Physical Sputtering and Sputter Deposition (Sputtering)*, Handbook of Physical Vapor Deposition, 2010.

[9] D. Mattox, *Plating and Surface Finishing* **80**, 38 (1993).

[10] H. Krebs, M. Weisheit, J. Faupel, E. Suske, T. Scharf, C. Fuhse, M. Stormer, K. Sturm, M. Seibt, H. Kijewski, D. Nelke, E. Panchenko, and M. Buback, *Advances in Solid State Physics* 43 **43**, 505 (2003).

[11] V. Craciun, J. Elders, J. G. E. Gardeniers, and I. W. Boyd, *Applied Physics Letters* **65**, 2963 (1994).

[12] Y. Hiroshima, T. Ishiguro, I. Urata, H. Makita, H. Ohta, M. Tohogi, and Y. Ichinose, *Journal of Applied Physics* **79**, 3572 (1996).

[13] M. Ashfold, F. Claeyssens, G. Fuge, and S. Henley, *Chemical Society Reviews* **33**, 23 (2004).

[14] X. Wu, S. Foltyn, R. Dye, A. Garcia, N. Nogar, and R. Muenchausen, *Thin Solid Films* **218**, 310 (1992).

[15] A. Ohtomo and A. Tsukazaki, Semiconductor Science and Technology **20**, S1 (2005).

[16] H. Habermeier, Applied Surface Science **69**, 204 (1993).

[17] H. Christen and G. Eres, *Journal of Physics-Condensed Matter* **20**, 264005 (2008).

[18] D. Bhattacharya, R. Singh, and P. Holloway, *Journal of Applied Physics* **70**, 5433 (1991).

[19] Q. Feng, "*Magnetic and Magneto-Optical Properties of Magnetic Oxides Thin Films*", PhD thesis, University of Sheffield, 2013.

[20] X. Chen, S. Xiong, Z. Sha, and Z. Liu, *Applied Surface Science* **115**, 279 (1997).

[21] A. Bulgakov and N. Bulgakova, *Journal of Physics D-Applied Physics* **28**, 1710 (1995).

[22] Y. Segawa, A. Ohtomo, M. Kawasaki, H. Koinuma, Z. Tang, P. Yu, and G. Wong, *Physica Status Solidi B-Basic Research* **202**, 669 (1997).

[23] M. Ying, W. Cheng, X. Wang, B. Liao, X. Zhang, Z. Mei, X. Du, S. Heald, H. Blythe, M. Fox, and G. Gehring, *Materials Letters* **144**, 12 (2015).

[24] R. Eason, Pulsed laser deposition of thin films: applications-led growth of functional materials (*John Wiley & Sons*, 2007).

[25] J. Mayer, *Nuclear Instruments and Methods* **63**, 141 (1968).

[26] K. Potzger, *Nuclear Instruments & Methods in Physics Research Section B-Beam Interactions with Materials and Atoms* **272**, 78 (2012).

[27] N. Petrova, P. Petrov, M. Edmonds, and C. Shanahan, *Calcified Tissue International* **94**, 403 (2014).

[28] M. Cardona, M. H. Brodsky, M. H. Brodsky, and M. Cardona, *Light scattering in solids* (Berlin ; New York : Springer-Verlag, 1975).

[29] L. Fine, (*American Library Association dba Choice*, p 320, Middletown, 2005).

[30] P. Vandenabeele, Analytical and Bioanalytical Chemistry **397**, 2629 (2010).

[31] L. Ziegler and P. Champion, XXII *International Conference on Raman Spectroscopy* (American Institute of Physics, Boston, USA, 2010).

[32] J. Serrano, A. Romero, F. Manjon, R. Lauck, M. Cardona, and A. Rubio, *Physical Review* B **69**, 14, 094306 (2004).

[33] J. Serrano, F. Widulle, A. Romero, A. Rubio, R. Lauck, and M. Cardona, *physica status solidi* (b) **235**, 260 (2003).

[34] K. Thoma, B. Dorner, G. Duesing, and W. Wegener, *Solid State Communications* **15**, 1111 (1974).

[35] A. Hewat, *Solid State Communications* **8**, 187 (1970).

[36] M. Newville ,*Reviews in Min-eralogy and Geochemistry* **78**, 33 (2014).

[37] S. Heald, T. Kaspar, T. Droubay, V. Shutthanandan, S. Chambers, A. Mokhtari, A. Behan, H. Blythe, J. Neal, M. Fox, and G. Gehring, *Physical Review* B **79**, 11, 075202 (2009).

[38] E. Alp, S. Mini, and M. Ramanathan, *Legibility Notice* 5, 25 (1990).

[39] D. Koningsberger and R. Prins, *X-Ray Absorption: Principles, Applications, Techniques of EXAFS, SEXAFS and XANES* (Wiley, 1988).

[40] D. Norman, *Journal of Physics C-Solid State Physics* **19**, 3273 (1986).

[41] M. Suzuki, K. Hanmura, T. Kotani, N. Yamaguchi, M. Kobayashi, and A. Misu, *Review of Scientific Instruments* **66**, 1589 (1995).

[42] E. Lage, L. Beran, A.Quindeau, L. Ohnoutek, M. Kucera, R. Antos, S. Sani, G. Dionne, M. Veis, and C. Ross, *APL Materials* **5**, 036104 (2017).

[43] M. Fox, *Optical properties of solids* (Oxford University Press, Oxford; New York, 2010).

[44] K. Sato, *Japanese Journal of Applied Physics* **20**, 2403 (1981).

[45] J. Wang, S. Hall, Y. Zhen, and D. Guo, *Journal of Superconductivity and Novel Magnetism* **23**, 1155 (2010).

[46] F. Jenkins, *Fundamentals of physical optics* (New York; London: McGraw-Hill, 1937).

[47] E. Lage, L. Beran, A.Quindeau, L. Ohnoutek, M. Kucera, R. Antos, S. Sani, G. Dionne, M. Veis, and C. Ross, *APL Materials* **5**, 036104 (2017).

[48] B. Wang, E. Hinds, and E. Krivoy, *Conference on Polarization Science and Remote Sensing IV* (San Diego, CA, 2009).

[49] W. Van Drent and T. Suzuki, *Journal of magnetism and magnetic materials* **175**, 53 (1997).

[50] J. Clarke, Squid Sensors: *Fundamentals, Fabrication and Applications* **329**, 1 (1996).

[51] J. Flokstra, H. Terbrake, E. Houwman, D. Veldhuis, W. Jaszczuk, M. Caspari, H. Rogalla, A. Martinez, and C. Rillo, *Sensors and Actuators a-Physical* **27**, 781 (1991).

[52] S. Bechstein, F. Petsche, M. Scheiner, D. Drung, F. Thiel, A. Schnabel, and T. Schurig, (7th *European Conference on Applied Superconductivity*, pp. 1266, Vienna Univ Technol, Vienna, AUSTRIA, 2005).

[53] H. Yang, C. Wu, J. Chen, K. Chen, M. Chen, S. Liao, H. Horng, and S. Yang, *Journal of the Korean Physical Society* **48**, 1084 (2006).

[54] B. Cullity, *Introduction to Magnetic Materials* (Wiley, Hoboken, 2009).

[55] K. Gramm, L. Lundgren, and O. Beckman, *Physica Scripta* **13**, 93 (1976).

[56] M. Mcelfresh, (*Quantum Design, Quantum Design*, 1994).

[57] C. Bean and J. Livingston, *Journal of Applied Physics* **30**, S120 (1959).

[58] R. Fagaly, *Review of scientific instruments* **77**, 101101 (2006).

[59] M. Ying, H. Blythe, W. Dizayee, S. Heald, F. Gerriu, M. Fox, and G. Gehring, *Applied Physics Letters* **109**, 5, 072403 (2016).

[60] U. Ozgur, Y. Alivov, C. Liu, A. Teke, M. Reshchikov, S. Dogan, V. Avrutin, S. Cho, and H. Morkoc, *Journal of Applied Physics* **98**, 041301 (2005).

[61] H. Morkoc, Zinc oxide fundamentals, materials and devicetechnology. (*Wiley-VCH*., Weinheim, 2009).

[62] (https://www.ad-na.com/en/product/jewel/material/sapphire.html).

[63] Y. Heo, M. Ivill, K. Ip, D. Norton, S. Pearton, J. Kelly, R. Rairigh, A. Hebard, and T. Steiner, *Applied Physics Letters* **84**, 2292 (2004).

[64] X. Sun and H. Kwok, *Journal of Applied Physics* **86**, 408 (1999).

[65] M. Kumar, R. Mehra, A. Wakahara, M. Ishida, and A. Yoshida, *Thin Solid Films* **484**, 174 (2005).

Chapter 4 Krypton (Kr) Implanted ZnO Films Grown by MBE

4.1 Introduction

This current chapter includes a description of the magnetic effects of Krypton (^{84}Kr)-doped ZnO by ion implantation. The implantation causes radiation damage in the samples, which produces defects that cause the observed magnetism. This is because Kr is an inert element, which has no local moment. Thus, it belongs to a special class of DMS called d^0 magnetisation. The first section of this chapter provides a literature review of d^0 magnetism in ZnO. The second section reports collections of experimental works of Kr with different concentrations implanted into ZnO samples. These ZnO samples are divided into two types, the first type of samples were 300 nm thick polar films and was produced on sapphire substrates by a radio frequency plasma-assisted molecular beam epitaxy (MBE) system. The second type were commercial polar ZnO single crystals with a thickness of 0.5mm. Both polar crystals and films have one O-polar and one Zn-polar face and both faces were implanted and studied. SQUID, Raman spectroscopy, X-ray diffraction and X-ray absorption fine structure spectroscopy studies were conducted to investigate the source of ferromagnetism. The work that is presented in this chapter has been published in the Journal of Materials Chemistry *C* [1].

4.2 Literature Review of d^0 Magnetism in ZnO

The d^0 magnetism is only found in undoped oxides and oxides that have been undoped or doped with elements that have complete d shells. This type of d^0 magnetism was observed in almost all oxides such as In_2O_3, TiO_2, MgO and ZnO grown as thin films or films with low crystalline quality. Among these candidates, ZnO has drawn great attention due to its outstanding properties, ease of availability and potential applications in spintronics [2].

Ferromagnetism is obtained in non-magnetic TM doped ZnO such as C or Cu-doped ZnO [3,4], and As-doped ZnO by ion implantation [1,5,6] or even in undoped ZnO [6-8]. It originates from points defects such as oxygen vacancies [3,9,10], interstitials [11], surfaces [7,12], or grain boundaries [8,13,14]. To the best of our knowledge, undoped ZnO can also have RTFM due to Zn vacancies [7,9,10,15]. Neither Zn^{2+} nor O^{2-} are magnetic and therefore such magnetism for thin films is not expected.

The magnetism is not found in a perfect crystal. This magnetism observed in ZnO strongly depends on certain experimentally controlled parameters such as the growth method chosen and post-annealing processes in different gas environments, which produce defects. The ion implantation method, as discussed in Subsection 3.2.3, generates suitable defect states associated with grain boundaries and point defects; including O and Zn interstitials, vacancies and anti-site defects. Thus, it is vital to investigate the correlation between FM and defects created in undoped ZnO and non-TM doped ZnO. This can result in a greater understanding of the ferromagnetism in d^0 materials in DMSs. Here a review of d^0 magnetism in undoped ZnO thin films, focusing on magnetisation arising from point defects, such as oxygen vacancies, Zn vacancies and grain boundaries is presented. Non-TM doped films are also discussed, such as Arsenic (As) doped-ZnO thin films by ion implantation, which are related to the work in this chapter.

The magnetic properties of undoped ZnO, which originate from defects such as oxygen vacancies, is discussed first. Zhan *et al* [10], reported RTFM in undoped ZnO thin films with a thickness of 100 nm when the films were thermally annealed in flowing Argon (Ar). Thus, defects were produced and the magnetisation observed was found to be due to oxygen vacancies, which also have been seen by others [16,17]. The XRD peaks produced from both pure ZnO and annealed ZnO thin films, at various temperatures in an Ar atmosphere, are shown in Fig 4.1. All peaks show a wurtzite structure corresponding to the (0002) plane of ZnO, indicating that the ZnO thin films are highly *c*-axis oriented. No secondary phases were detected except for the film that was annealed at 750° C, in which Zn_2SiO_4 was formed due to the reaction that occurred between the SiO_2 substrate and ZnO film. Thus, the magnetisation depended on how much oxygen is present in the material. The ferromagnetism has been increased with annealing as the temperature increased up to 600° C for two hours in an Ar atmosphere, as shown in Fig 4.2. The magnetisation observed in ZnO films, as grown, has small ferromagnetism. However, annealing the films in Ar at higher temperatures leads to oxygen vacancies on the surface of the film and increased ferromagnetism. This was confirmed by photoluminescence (PL) spectroscopy, which shows a decreased oxygen present at the film surface after annealing [10].

Removed

by the author

for copyright reasons

Figure 4.1: XRD peaks for all films; pure ZnO thin films and annealed ZnO deposited on quartz substrate taken from [10].

Removed
by the author
for copyright reasons

Figure 4.2: Magnetic hysteresis loops of pure ZnO thin films annealed at different temperatures measured at 300K taken from [10].

Now, the magnetic properties of undoped ZnO films, which originate from defects such as Zn vacancies are discussed. The work by Hong *et al* [7], for instance, observed RTFM for undoped ZnO thin films made by PLD. Fig 4.3 shows the two films of thickness 10 and 50 nm are strongly magnetic while the magnetisation disappeared for the 375 nm film. This implies that the defects arose from the film's surface, where the defects are generated. These defects are only found in thin films and are not present in the bulk. The films were not affected after being annealed for 10 hours in an oxygen atmosphere, and the source of magnetism was found to be Zn vacancies. Hong *et al* [7] also argued that TM doping in ZnO might not play an essential role in the magnetism observed in ZnO. However, it might only enhance the magnetism in specific systems. This was concluded after the magnetic properties of undoped ZnO, as well as Fe, and Mn-doped ZnO thin films were carefully investigated [7]. The magnetisation observed in Fe-doped ZnO was similar to undoped ZnO thin films. However, the magnetisation observed in Mn-doped ZnO thin film has an additional ferromagnetic compound, which enhances the total magnetic moment in the host, via the double exchange interaction.

Removed
by the author
for copyright reasons

Figure 4.3: Magnetisation of pure ZnO as a function of the magnetic field at 300 K for films of thickness 10 nm, 50 nm, and 375 nm taken from [7].

The magnetism found in d^0 materials arises due to defects. The aim is to control these defects in a way that may lead to the desired formation of different defects. This can be achieved by adjusting the growth methods as well as post-synthesis treatment such as annealing in a different gas environment. Therefore, Xing *et al* [15] investigated the ferromagnetism of undoped ZnO thin films that were grown via two different methods; Sol-gel (SG) and MBE. It was found that the synthesis routes can cause a significant change in the structure and the properties of thin films and maybe tuned expertly to produce defects. A ZnO thin film of 400 nm on a Si substrate was produced by the SG method, in a rich oxygen environment which led to point defects such as Zn vacancies. The other set of high-quality 400 nm ZnO films were grown on the sapphire substrate by MBE. Fig 4.4 shows that the film exhibited large RTFM independent of temperature and then a further reduction after annealing in an Ar atmosphere.

The ferromagnetism was also confirmed, by photoluminescence measurements, to result from Zn vacancies [15]. However, the films made of MBE, which are of high-quality, have negligible ferromagnetism. This work strongly suggests that defects are essential to observe ferromagnetism in ZnO.

Removed
by the author
for copyright reasons

Figure 4.4: Magnetic hysteresis loops of the two sets of ZnO films as-grown and annealed in Ar at 5 k and 300 K taken from [15].

It is important to stress that only d^0 magnetism that arises from defects is discussed and this does not include bulk materials or materials that are otherwise free from defects. This magnetism can be created from the spontaneous splitting of the shallow impurity band, as first proposed by Coey *et al* [18,19]. The strong temperature independent magnetisation can be observed if the narrow band of the electron states has sufficient interaction, which leads to Stoner splitting as discussed in Section 2.6. The narrow defect bands associated with both donors and with acceptors can occur in ZnO.

Coherent transport of electrons through the material is necessary for band formation. In order to achieve this the donor states in the material must overlap by a distance that is less than or equal to the defect radius r_d. The most common estimation for this uses the hydrogenic model, which is more accurate for the largest donors and is given by the formula $r_d = r_H \varepsilon/(\frac{m_e}{m})$, where r_H is the radius of a hydrogen atom and ε is the dielectric constant of the material. The radius of the donor state was calculated to be r_d ~ 30 nm in ZnO. Once the minimum separation is known, it is possible to estimate the minimum concentration of defects required for coherent transport of electrons in the material. This is given by $1/V$, where V is the volume of the donor state and is calculated to be ~ 9×10^{16} defects per cm^3. It is important to note that the hydrogenic model assumes that the dielectric constant is continuous, and only provides an estimation, it is however the best simple theory and is used by many in the field as a first estimation of the minimum density of defects required for coherent transport.

However, the defect states must be sufficiently deep so that the defect bands do not overlap the conduction or the valence band because this would lead to a wider band and hence a lower density of states. This combination of a relatively narrow band gap and deep defect levels appears to occur for only ZnO.

The impurity band, according to some studies, can also originate at grain boundaries [13,14]. Thus, the defects that cause the RTFM in undoped ZnO thin films including grain boundaries is discussed. The review by Straumal *et al* [14] showed that observed RTFM in undoped ZnO thin films is due to grain boundaries and not due to the intrinsic property of the ZnO crystalline lattice. The magnetisation also can be enhanced by TM-doping in ZnO such as Mn-doped ZnO. This was observed in multiple data sets produced from undoped ZnO and Mn-doped ZnO thin films, which demonstrate ferromagnetic behaviour. Fig 4.5 (a) and (b) shows the collection of the grain boundary areas sources that were tabulated and summarised of pure ZnO and Mn-doped ZnO respectively as a function of temperature. It can be seen that the magnetic films have small grain sizes of the order of 10^{-7}m for pure ZnO films. However, doping Mn in ZnO shifts the grain size to the order of 10^{-5} m with the FM remaining unchanged. All the data points from films on the right side of the hard line are magnetic while the data points from the films on the left are non-magnetic. The grain sizes were about 10^{-8} m, as shown in Fig 4.5 (a). By adding Mn to the ZnO system, the magnetic properties sometimes increase and the grain sizes generally decrease, as shown in Fig 4.5 (b). No magnetism was observed when TM-doped ZnO bulk (crystal). This is because thin films have texture and amorphous inter crystalline layers. This dictates that the origin of the ferromagnetic properties is derived from the grain boundary sizes and adding TM to ZnO increases it.

Removed
by the author
for copyright reasons

Figure 4.5: Ferromagnetic (full symbols) and paramagnetic or diamagnetic properties (open symbols), where the solid vertical black line is to divide the ferromagnetic (right) and non-ferromagnetic behaviour (left), of (**a**) pure zinc oxide and (**b**) Mn-doped ZnO versus the specific area of grain boundaries sGB (ratio of the area of the boundaries to the volume) at various synthesis temperatures (T), taken from [14].

The magnetism, which arises from defects caused by ion implantation, is considered and is the subject of this chapter. The structural and magnetic properties of implanting non TM such as arsenic (As), on two high-quality ZnO films with different polarity was investigated by Ying *at el* [6]. The 400 nm thick films, O-polar and Zn-polar ZnO, were grown on a sapphire substrate by MBE. The two polar surfaces are reported to give structurally and chemically different films [20]. They differ in their optical and electrical properties, doping efficiency and impurity incorporation [21]. A range of different implantation energies 400KeV, 200KeV, 100KeV, and 30KeV were used to achieve near uniform doping at a chosen depth. Fig 4.6 shows that both films O-polar and Zn-polar exhibit large RTFM, independent of temperature. The observed RTFM for O-polar is twice as big as the magnetisation observed in O-polar ZnO films. Thus, the observed magnetisation cannot be due to local moments because it is too big but instead is due to the lattice disorder introduced by ion implantation. Also, the observed magnetisation differences between the O-polar and Zn-polar films can be attributed to the different defect densities. The origin of magnetisation was from the lattice defects, which was introduced by ion implantation.

Removed
by the author
for copyright reasons

Figure 4.6: Magnetisation hysteresis loops for As doped O-polar and Zn-polar ZnO films at 5 K and 300 K after separating the ferromagnetic and paramagnetic contributions. The inset shows paramagnetism at 5 K taken from [5].

An extension of the previous work performed by Ying *et al* [6], investigated different concentrations of implanted As in high-quality O-polar ZnO thin films on a sapphire substrate made by MBE. Three samples with different As doping concentrations of 6×10^{17} cm^{-3}, 6×10^{18}

cm^{-3}, and 6×10^{19} cm^{-3} were produced. In Fig 4.7 (a) the XRD peaks were attained for undoped ZnO and As implanted ZnO films and all the samples show a single phase of the wurtzite structure. These correspond to the (0002) and (0004) plane of ZnO, indicating that the ZnO thin films are highly *c*-axis oriented. No secondary phases were detected for the films. In Fig 4.7 (b) the enlarged ZnO (0002) peak shows that the peaks shift to lower angles with increasing the doping concentration, indicating expansion of the *c*-axis parameter. The inset shows the calculated lattice constant as a function of dose concentration.

Fig 4.8 shows the magnetisation hysteresis loops of undoped ZnO and As implanted O-polar ZnO thin films, which exhibit large RTFM and independent of temperature. The diamagnetic contributions from the undoped ZnO thin film have been subtracted from the plots.

Removed

by the author

for copyright reasons

Figure 4.7: (**a**) XRD peaks for undoped ZnO and As implanted ZnO, (**b**) the enlarged ZnO (0002) diffraction peaks. The inset in (**b**) shows the c-axis parameter as a function of doping concentration taken from [6].

It was noticed that the RTFM was largest with the highest dose of As implanted in O-polar ZnO films. Thus, the magnetisation decreases with decreasing concentration and the number of defects decreases due to the ion implantation process. The magnetic moment per As atom was calculated for the highest doping sample of 15.2 emu/cm^3 is 27 μ_B/As, which is much higher than 1 μ_B/As which was predicted by Lu *et al* [22]. Thus, the observed magnetisation was due to the polarised lattice defects produced by ion implantation.

Removed

by the author

for copyright reasons

Figure 4.8: Magnetisation hysteresis loops for As-doped O-polar ZnO films at 5 K and 300 K after subtracting the diamagnetism contribution from undoped ZnO. The inset shows diamagnetism of undoped ZnO at 5 K and 300 K taken from [6].

4.3 Sample Preparation

Two types of sample, a high-quality O-polar and Zn-polar ZnO film, were made with a radio frequency (RF) plasma-assisted molecular beam epitaxy (MBE) system, see Subsection 3.2.2. The thickness of the films was 300 nm and they were deposited on the sapphire substrate by our collaborators Dr Zengxia Mei and Prof Xiaolong Du at the Beijing National Laboratory for Condensed Matter Physics, Institute of Physics, Chinese Academy of Sciences. Also, another set of samples were produced from commercial polar ZnO single crystals. The single crystals were purchased from Hefei Kejing Materials Technology Co. Ltd and were 0.5 mm thick, with one O-polar and one Zn-polar face. High-quality krypton ions were then inserted into O-polar and Zn-polar ZnO films and single crystals by the ion implantation method, as discussed in Subsection 3.2.3, by our collaborator Dr Minju Ying at the College of Nuclear Science and Technology, Beijing Normal University, Beijing, China.

The Stopping and Range of Ions in Matter (SRIM) reveals that a sequence of four implantation energies 200 KeV, 150 KeV, 80 KeV, and 30 KeV was essential to create an almost uniform distribution of Kr ions through the whole of the depth of the 70 nm layers of the films. This is much less than the thickness of the 300 nm film so that the ions implanted in the substrate can be neglected. Thus, three doped Kr concentrations of 5×10^{19} cm^{-3}, 1×10^{20} cm^{-3}, and 5×10^{20} cm^{-3} were implanted and investigated in this chapter, as shown in Fig 4.9. The dose of each ion at different energies is given in Table 4.1.

Table 4.1: The parameters of the implantation: energies, concentration and doses.

Energies keV	**Dose (ϕ) cm^{-2}**	**The concentration of Kr at a chosen depth**
200	**2.5×10^{14}**	**5×10^{19} cm^{-3}**
150	**5×10^{13}**	
80	**7.5×10^{13}**	
30	**5×10^{13}**	
200	**5×10^{14}**	**1×10^{20} cm^{-3}**
150	**1×10^{14}**	
80	**1.5×10^{14}**	
30	**1×10^{14}**	
200	**2.5×10^{15}**	**5×10^{20} cm^{-3}**
150	**5×10^{14}**	
80	**7.5×10^{14}**	
30	**5×10^{14}**	

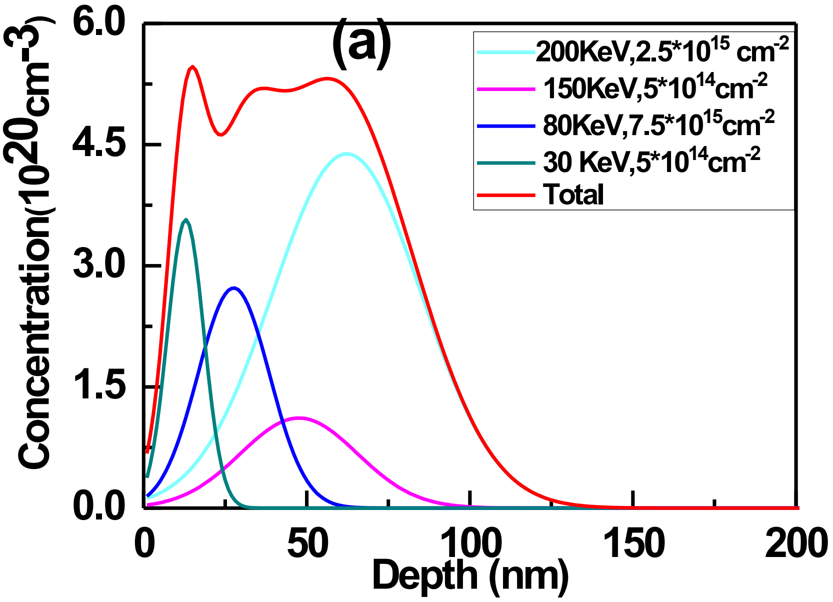

Figure 4.9: The distribution profiles of high doping Kr ions film with a sequence of four implantation energies, the total shows a near even Kr ions distribution with Kr concentration of ~ 5×10^{20} cm^{-3} up to a thickness of ~ 70 nm, taken from [1].

4.4 Experimental Results and Discussion

The Kr implanted films and crystals structural properties were studied using X-ray diffraction (XRD) and Raman spectroscopy measurements by our collaborator Dr Minju Ying at the College of Nuclear Science and Technology, Beijing Normal University, Beijing, China. The X-ray absorption fine structure spectroscopy measurement and analysis were obtained by our collaborator Dr Steve Heald at the Advanced Photon Source in the Argonne National Laboratory, USA. The magnetic properties were characterised using a superconducting quantum interference device (SQUID) magnetometer and were carried out at the Department of Physics and Astronomy at the University of Sheffield.

4.4.1 Structural Properties

Structural properties were analysed for all Kr implanted films in both O-polar and Zn-polar ZnO films and single crystals. The structure of the crystal lattice, the lattice constant, and the grain sizes were obtained from the XRD measurement. This was essential to observe the effect of the Kr implantation on high-quality O-polar and Zn-polar ZnO thin films and single crystals.

All the X-ray measurements for the undoped ZnO films and Kr implanted O-polar and Zn-polar ZnO films and crystals were made using the apparatus similar to the one discussed in Section 3.3.1 with θ-2θ geometry. The XRD plots of all the films exhibit a single phase with a typical wurtzite ZnO structure, showing a *c*-axis out of plane orientation with only (0002) and (0004) ZnO diffraction peaks. The (0006) diffraction peak is from the sapphire substrate, marked S in Fig 4.10. No secondary phases were detected within the detection limit of the XRD.

The XRD patterns from the Kr-doped O-polar ZnO films are shown in Fig 4.10 (a) along with the enlarged ZnO (002) diffraction peaks in Fig 4.10 (b). It can be seen that the diffraction peaks are shifted closer to smaller angles as the doping concentration is increased; indicating the *c* lattice constant is expanding after ion implantation. Table 4.2 gives a summary of the information obtained from the XRD measurements such as the lattice parameter, FWHM of ZnO (0002), and grain sizes for the O-polar films and single crystals.

The Debye-Scherrer formula was used to estimate the grain sizes, as explained in Subsection 3.3.1; however, the calculated grain sizes for undoped ZnO films and single crystals were larger than 100 nm, which is not valid to calculate it by the Scherrer formula. A large increase of the lattice constant corresponding to the O-polar films was obtained compared to the small increase found in the O-polar single crystals. Also, the radiation damage from the implantation has caused the FWHM to increase. The increase of FWHM indicates that the formation of the grain fragmentation occurred as a result of the expansion of the lattice constant due to Kr incorporation. The highest expansion of the FWHM and largest grain fragmentation observed was found in the O-polar films with doping larger than 5×10^{19} cm^{-3}. The high increase of the *c* lattice constant and little grain size were observed in the implanted Kr-doped O-polar films which suggest that a considerable amount of the Kr atoms were implanted into the grains.

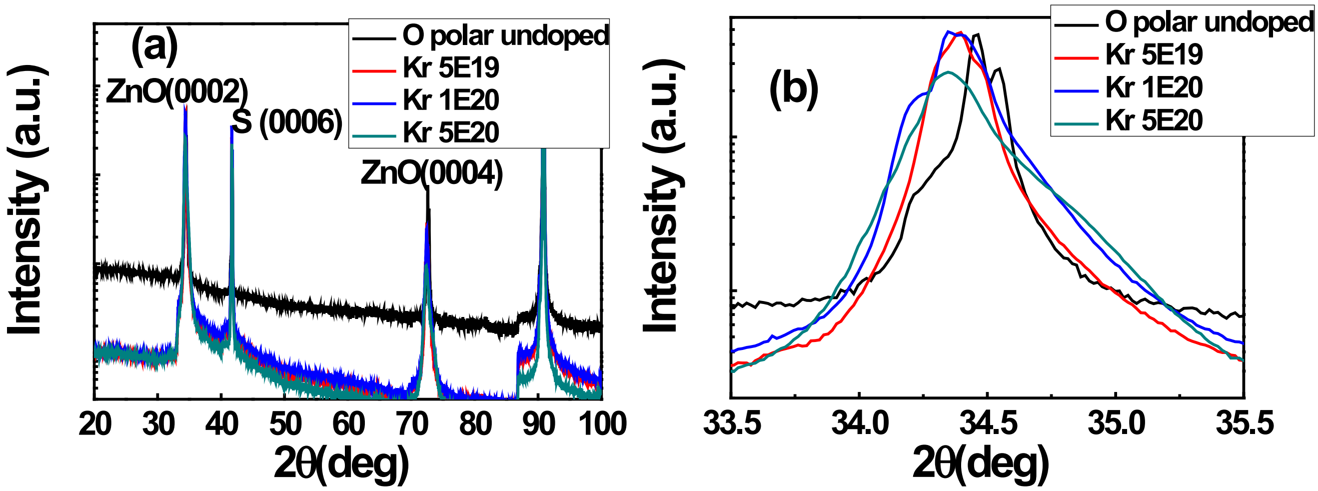

Figure 4.10 (**a**): XRD data for O-polar films showing all the reflections, where the S peak refers to the sapphire substrate. (**b**) An enlarge plot of the ZnO (0002) reflection using a log scale taken from [1].

Table 4.2: Kr-doped O-polar ZnO films and single crystals indicate the calculated lattice constants and grain sizes.

Samples	**The lattice constant (±0.002 Å)**				**FWHM(±0.005 degree)/Grain size ((±5 nm)**			
	undoped	**5×10^{19}** (cm^{-3})	**1×10^{20}** (cm^{-3})	**5×10^{20}** (cm^{-3})	**undoped**	**5×10^{19}** (cm^{-3})	**1×10^{20}** (cm^{-3})	**5×10^{20}** (cm^{-3})
Doped O-polar films	5.202	5.211	5.214	5.222	0.071	0.091/90	0.111/74	0.149/55
Doped O-polar single crystals	5.205	5.207	5.208	5.207	0.063	0.082	0.083	0.077

No large lattice expansion was noticed for Zn-polar films suggesting that a large number of the Kr atoms were deposited at the grain boundary. Reflection high-energy electron diffraction (RHEED), which is a technique utilised to characterise the surface of the crystalline materials, confirmed that the island surface structure of the Kr implanted Zn-polar ZnO films caused the implanted Kr atoms to go into the grain boundary [1].

Table 4.3: The estimated lattice constants and grain sizes for Kr implanted Zn-polar ZnO films and single crystals.

Samples	**The lattice constant (±0.002 Å)**				**FWHM(±0.005 degree)/Grain size (±5 nm)**			
	undoped	**5×10^{19}** (cm^{-3})	**1×10^{20}** (cm^{-3})	**5×10^{20}** (cm^{-3})	**undoped**	**5×10^{19}** (cm^{-3})	**1×10^{20}** (cm^{-3})	**5×10^{20}** (cm^{-3})
Doped Zn- polar films	5.202	5.203	5.203	5.205	0.063	0.080/>100	0.085/97	0.090/91
Doped Zn- polar single crystals	5.205	5.207	5.208	5.208	0.065	0.068	0.078	0.077

The X-ray absorption near edge (XANES) and extra-fine-structure-absorption spectroscopy (EXAFS) measurements were performed to investigate the position of the Kr in the lattice, as shown in Fig 4.11 (a) and (b). Two separate runs were performed to collect the data, and the results of both runs were consistent. Fig 4.11 (a) shows the combined data set of the two measurement runs. It is worthwhile to mention that the multi-electron background of the Kr gas is present and must be carefully considered when making the measurement. Thus, the strong multi-electron features derived from Kr atoms were extracted by subtracting the signal that comes from a sample of Kr gas. However, no signal of the EXAFS can be obtained. The EXAFS measurement of the samples reveals that the Kr atoms were in random sites because the signal was very weak. Fig 4.11 (b) shows the low R features in the Fourier transforms resulting from the residuals of the Kr background. The Zn-polar film has a much smaller amplitude in comparison to the O-polar films indicating higher disorder and/or fewer neighbours in Zn-polar films. This is supported by the XRD data, which reveals that the Kr atoms move into the grain for the O-polar and to the grain boundary for the Zn-polar films. Therefore, higher disorder and/or fewer neighbours were found in the Zn-polar ZnO samples.

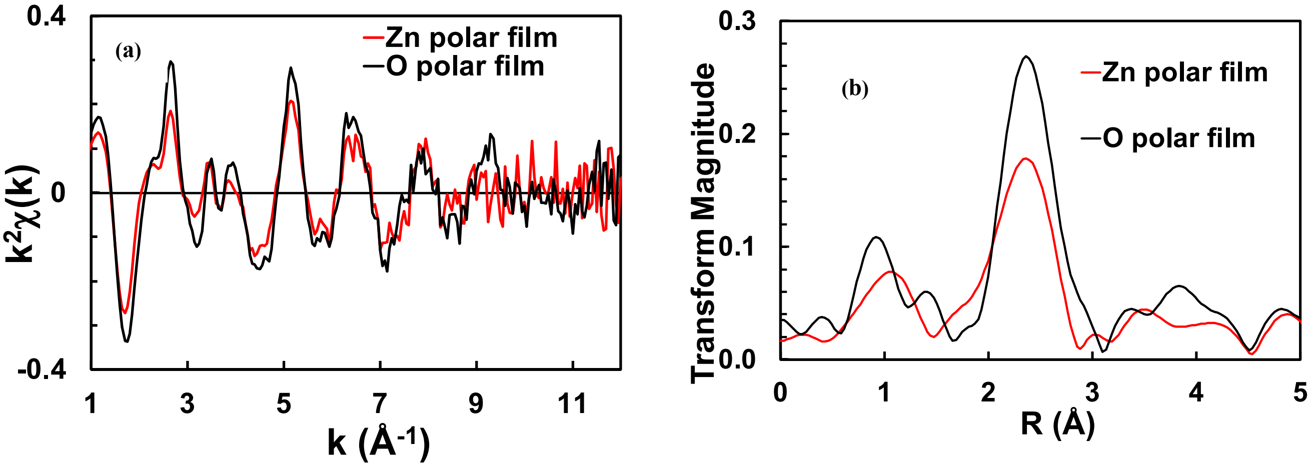

Figure 4.11: EXAFS data for 5×10^{20} cm^{-3} Kr-doped O-polar and Zn-polar ZnO films; (**a**) a plot of $k^2\chi(k)$ and (**b**) $|\chi(R)|$ taken from [1].

Another measurement for the Zn near edge absorption was made for the highest implanted Kr-doped O-polar and Zn-polar ZnO films, including all the Zn in the film and the implanted part. The measurement did not detect any notable difference between the data for the O-polar and Zn-polar film, as shown in Fig 4.12. It was challenging to distinguish if the defects that were introduced, in theses implanted films, caused the Zn ionisation to be increased or decreased. However, the observed magnetism suggests that charged defects were produced for the implanted films.

Raman spectroscopy was utilised in this work to distinguish between the point defect density and the grain boundaries as it was discussed previously in Section 3.3.2. Fig 4.13 shows a selection of peaks at 380 cm^{-1}, 418 cm^{-1}, 578 cm^{-1} and 752 cm^{-1}, marked S, for the sapphire substrate. Two well-known peaks of ZnO are shown for undoped ZnO films, low-frequency mode marked E_2(L) at 101 cm^{-1} and high-frequency mode marked E_2(H) at 439 cm^{-1}. The high-frequency E_2 mode is believed to be the oxygen sublattice [23] while the vibration of the heavy Zn sublattice corresponds to the low-frequency E_2 mode. The undoped ZnO films show no other peaks, which concludes that no secondary phases can be found within the detection limit.

It was observed that the total Raman intensity for implanted films was much higher than for undoped films. There is a pronounced peak arising at 580 cm^{-1} with a possible second reduced peak at lower frequencies as has been seen previously in both doped and implanted ZnO [5,23-26]. However, another high broad signal was observed in the range of 50 cm^{-1} and 300 cm^{-1}, which increases nearly linearly between 300 cm^{-1} to 500 cm^{-1}.

The peak at 580 cm^{-1} was observed in other studies related to nanoparticles [27,28] and can be associated with two Raman peaks A_1(LO) at 584 cm^{-1} and E_1(LO) at 595 cm^{-1}, which are forbidden for undoped ZnO in the $z(xx)\bar{z}$ geometry. The multi-phonon scattering corresponding to the broadened signal at approximately 540 cm^{-1} is due to defects.

The signal that arises in the range of 50 cm^{-1} to 300 cm^{-1} can be attributed to the phonon density of states [29,30], which can be explained by the amorphous regions in the grain boundaries. Such a signal was observed in a different study of As implanted ZnO [5], however, it was not seen in nanoparticles [27] suggesting that the signal is related to the grain boundary region not to the finite grain size.

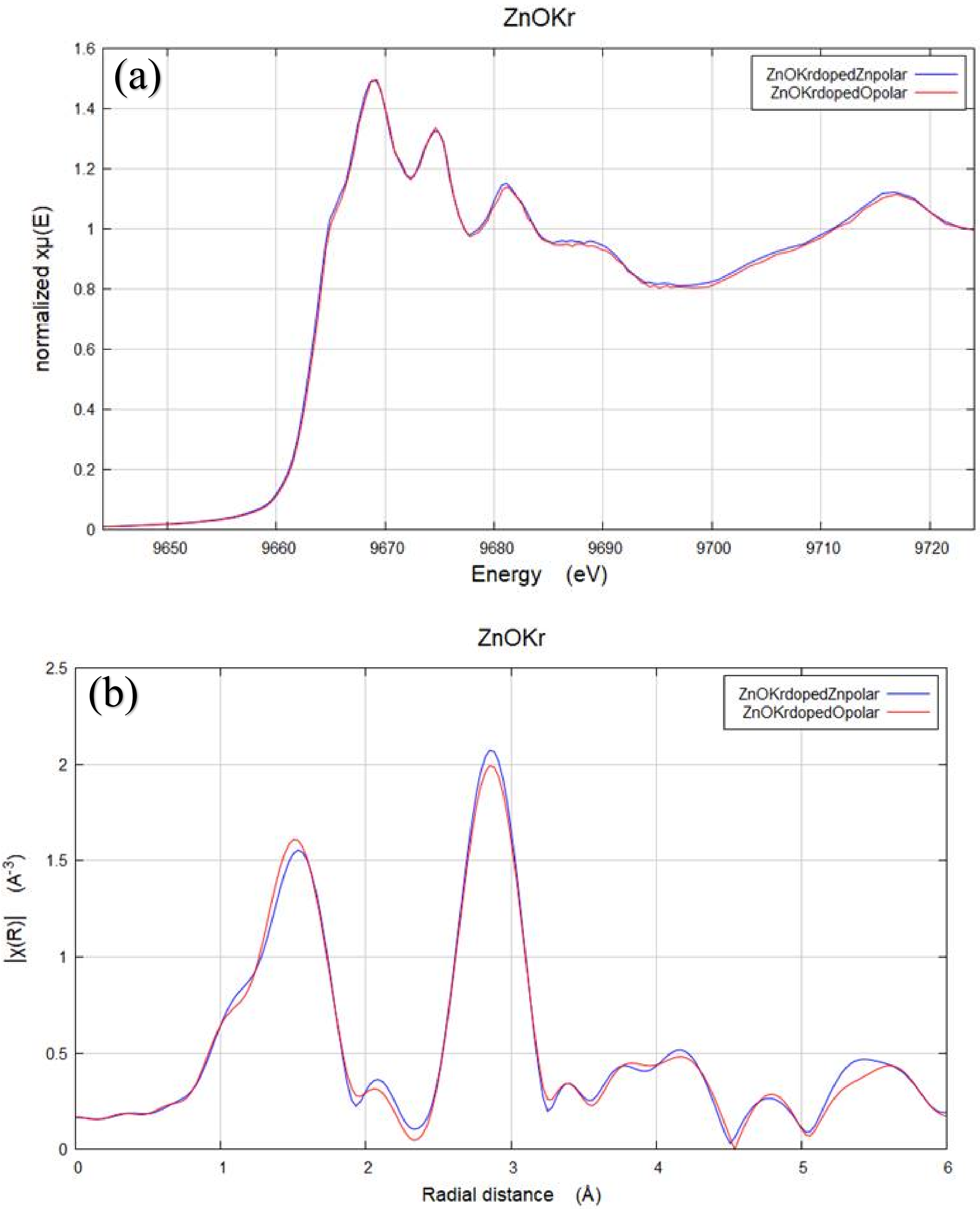

Figure 4.12: (**a**) XANES and for Zn in the highest doped concentration Kr implanted O-polar and Zn-polar ZnO films. (**b**) EXAFS for Zn in the highest doped concentration Kr implanted O-polar and Zn-polar ZnO films taken from [1].

The two signals, corresponding to the undoped ZnO at 101 cm^{-1} and 438 cm^{-1}, are not strong enough to be seen for the O-polar but are clearly visible in the Zn-polar film as shown in Fig 4.13(a) and 4.13 (b) respectively. Thus, Kr-doped O-polar films can be prone to damage as the signal peak at 438 cm^{-1} was also observed in different implanted ZnO films and dope nanoparticles [28,31,32]. The grain size was decreased for the O-polar films as indicated in the low scattering, which dominates the signal. The two Raman signals E_2(L) and E_2(H) show that the film still keeps overall crystallinity, the Raman peak at ~580 cm^{-1} for O-polar is somehow less intense than the film for Zn-polar indicating that a massive point defect has occurred.

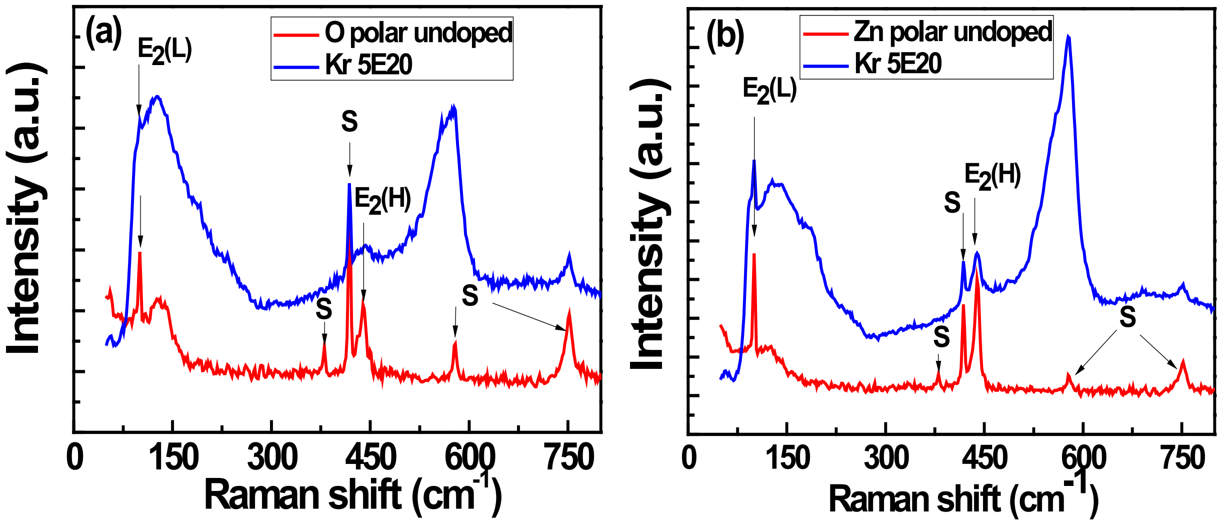

Figure 4.13: Peaks of the Raman spectra for the undoped and 5×10^{20} cm^{-3} Kr-doped ZnO films. (**a**) O-polar (**b**) Zn-polar films, taken from [1].

4.4.2 Magnetic Properties

The magnetic hysteresis loop measurements were taken using the superconducting quantum interference device (SQUID) at 5K and 300K, for both doped and undoped samples. It is worthwhile mentioning that the magnetisation of the Kr-doped ZnO films was calculated by deducting the un-doped ZnO film from that obtained for the implanted film. The films were in irregular shapes, so the area A of the films are given by

$$A = \text{Mass (Substrate + film)} / \rho L \qquad (4.1)$$

Where ρ is the density and L is the substrate thickness. Since the thickness of the film, 300 nm, is very much less than L, its contribution can be ignored. The saturation magnetisation for the doped samples was calculated from the following:

$$\Delta M_{saturation}(\text{emu/g}) = \text{implanted (emu)/weight(g) - unimplanted (emu)/weight(g)} \qquad (4.2)$$

(M/g) was used to separate the effects due to different areas. Thus, the result in emu units is divided by the weight of the sample. The magnetisation per unit volume was evaluated using the implanted depth of 70 nm, as shown in Fig 4.1 (a). In some cases, ΔM_{sat}, as defined in this way, was negative! As this was clearly unphysical, it allowed us to estimate the error in our measurements as ±10 emu.

For Kr-doped O-polar films, with the highest doping concentration of 5×10^{20} cm^{-3}, extremely large ferromagnetism has been obtained which is independent of temperature, with Ms values of 186 and 185 emu cm^{-3} at 5 K and 300 K respectively. When the Kr-doped concentration decreased and reached 1×10^{20} cm^{-3}, magnetic hysteresis loops were observed with a saturation magnetisation of 38 and 28 emu/cm^{3} at 5 K and 300 K respectively. However, no detectable magnetisation was observed at 5 K neither at 300 K for Kr doping at a low concentration of 5×10^{19} cm^{-3} in O-polar films. No detectable magnetisation was observed for all concentrations of Kr in O-polar ZnO single crystals.

Fig 4.14 shows the value of the saturation magnetisation for Kr-doped O-polar ZnO film as a function of the implanted Kr dose concentration. The magnetisation of the O-polar ZnO film increases linearly with increasing Kr doping concentration. This is due to the fact that defects induced by ion implantation, extend with the doping concentration [1]. Fig 4.15 shows the magnetic hysteresis loops for Kr-doped O-polar films doped with different concentrations of 5×10^{19} cm^{-3}, 1×10^{20} cm^{-3}, and 5×10^{20} cm^{-3}. Table 4.4 gives the value of the magnetic saturation and the magnetic moment per implanted Kr ion for O-polar ZnO films at 5 K and 300 K.

Table 4.4: The saturation magnetism, *Ms*, and the moment per implanted Kr atom for O-polar ZnO films at 5 K and 300 K.

O-polar film	***Ms* (emu/cm^3)**		***Ms* (μ_B/Kr) (Method A)**		***Ms* (μ_B/Kr) (Method B)**	
	5 K	**300 K**	**5 K**	**300 K**	**5 K**	**300 K**
5×10^{19} cm^{-3}	0 ± 10	0 ± 10	0± 10	0± 10	0±5	0±5
1×10^{20} cm^{-3}	38 ± 10	28 ± 10	41± 10	30± 10	20±5	15±5
5×10^{20} cm^{-3}	186 ± 10	185 ± 10	40± 2	40± 2	28±2	28±2

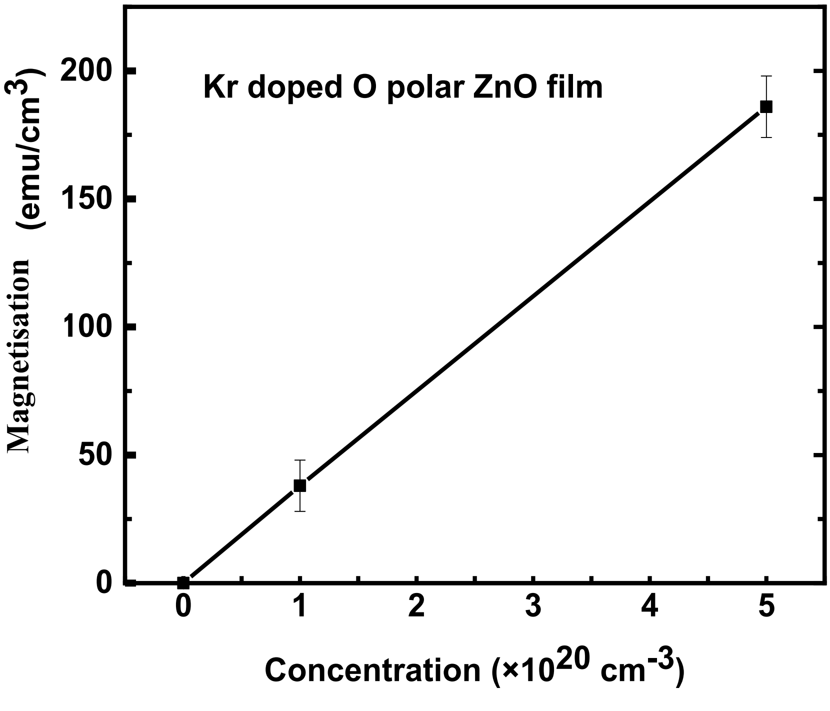

Figure 4.14: Magnetisation is linear of the Kr-doped O-polar ZnO film measured at 5 K as a function of Kr concentration.

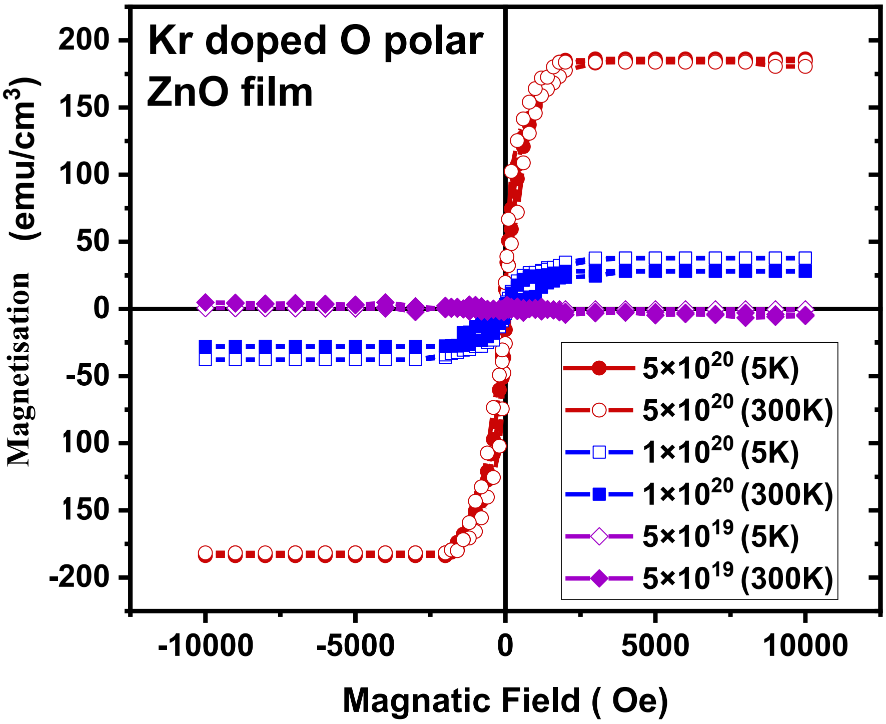

Figure 4.15: Magnetization data, found after subtracting the magnetisation signal measured for undoped O polar ZnO film, for Kr doped O polar ZnO films at 300 K and 5 K for Kr concentrations of 5×10^{20} cm^{-3}, 1×10^{20} cm^{-3}, and 5×10^{19} cm^{-3}.

The extremely large saturation magnetisation of 186 and 185 emu cm^{-3} for Kr-doped O-polar, at high doping concentrations, was observed at 5 K and 300 K respectively, as shown in Fig 4.15. This corresponds to the enormous magnetic moment per Kr ion. Such a result implies that the observed magnetisation is due to the implantation process instead of the local moment derived from the Kr-doped in the ZnO lattice because Kr has is an inert chemical with no local moments. Hence, the observed magnetisation was independent of temperature, and the coercive field was low for the Kr-doped O-polar film with the highest doping concentration of 5×10^{20}, both characteristics are similar to those caused by the defect magnetisation [13,19,33].

The magnetisation for the sample doped with 1×10^{20} cm^{-3} Kr ions has decreased at 300K because it was affected by the weaker magnetisation coupling in various defective regions. The suggested value of the grain size of ~33 nm [34] is partially lower than the values of the grain sizes of 55 nm and 74 nm for both 5×10^{20} cm^{-3} and 1×10^{20} cm^{-3} doped films respectively. The magnetic moment per Kr ion was calculated in two ways; the first way is common where it is similar to the one used for As implanted ZnO [5]. The first method of determining the magnetic moment per Kr atom is used by taking the concentration at the chosen depth ~70 nm as shown in table 4.1. The method can be explained as the following:

Assume all the magnetisation results from the implantation of Kr ions into your film and anything else is negligible. The saturation magnetisation in emu/cm^3 is divided by the Kr doping concentration in cm^3 to get the total magnetic moment as the following:

$$\frac{M_S}{Kr \text{ concentration}} = \frac{186}{5\times10^{20}} = 3.92 \times 10^{-19} \text{ emu.} \tag{4.3}$$

Then, to convert from emu to μ_B, the total magnetic moment is multiplied by 1.078×10^{20}. Thus, our result ~ 40 μ_B/Kr, which is much higher than 27μ_B/As obtained from the previous work of As implanted ZnO [5].

The second method of determining the magnetic moment per Kr atom is used by taking the total number of Kr atoms into consideration including all the doping concentrations of the films as shown in Table 4.1. The method can be explained as the following:

The total magnetisation M_0, in a film of area A is measured in emu units. Two useful measures are connected. The first is magnetisation per unit volume where $m = \frac{M_0}{Ad}$ emu/cm^3. Here d is the approximate thickness of the implanted region. The second is magnetisation per implanted Kr in Bohr magnetons, $m_{Kr} = \frac{M_0}{FA\mu_B}$ where F is the total flux of implanted Kr so that the total number of implanted ions is FA. These two expressions are related to the following:

$$m_{Kr} = \frac{M_0}{FA\mu_B} = \frac{dm}{F\mu_B} \tag{4.4}$$

Now, the total flux of the most heavily implanted Kr can be calculated as F= (25+5+7+5) ×10^{14} cm^{-3} from Table 4.1. Hence, F= 4.2×10^{15} cm^{-3}, $\mu_B = 9.27\times10^{-21}$, and m = 186 emu/cm^3 at 5k. The depth of the Kr implantation is associated with the minimum flux of 5×10^{14} cm^{-3} is at 10 nm and the maximum flux of 25×10^{14} cm^{-3} at 70nm. Hence we take the difference as d= (70-10) = 60 nm, which is associated with the implantation ranges. The resulting magnetic moment of the Kr ion is 28μ_B/Kr, which is much smaller than the value 40μ_B/Kr which is calculated by method (I), as shown in Table 4.4. This result is as expected as all the Kr atoms were included while in the previous calculation only the highest density region was used. Even the second method shows a much larger value of Kr per ion than expected to originate from the defect state localised at the Kr. No magnetisation was observed for the Kr-doped Zn-polar films and wafers.

All these results show that both the structural and magnetic characteristics of the implanted Kr O-polar films can be distinguished from all others, such as Zn-polar films and ZnO wafers. Both XRD and EXAFS showed that the grain size was reduced substantially for the O-polar films compared to Zn-polar films, implying the Kr atoms were not combined in the grain boundary but were in the lattice. Raman spectra clearly showed the scattering of the point defects for the Zn-polar films is stronger than that scattering for the O-polar film. No magnetisation was observed for the Zn-polar films, but large magnetism was observed for the O-polar films because O-polar films are prone to absorb impurities [21,31] and have flat surface morphology leading to the incorporation of ^{84}Kr ions into the lattice [1]. In addition, the relative size of Kr in comparison to ^{65}Zn or ^{16}O leads to strain in the lattice, this causes fractured grains which produce grain boundaries, causing the resulting magnetism.

Hence, our result demonstrates that the observed magnetisation is almost independent of temperature, indicating that the magnetism emerged from the polarised electrons in the narrow defect band [35]. The magnetisation observed arises from defect states which are near to each other and form a band; where other isolated defects that have localised states can be ignored. Both donor and acceptor defects are formed as expected e.g. Zn vacancy (acceptor) and a Zn interstice (donor). Complex defects occur in the grain boundary region. The theory of the proposed grain-boundary defect model suggests that the zinc vacancies are located on the grain boundary; in order to offset the positively charged oxygen vacancies that stretch into the adjacent grains [35,36].

4.5 Conclusions

In this chapter, the magnetisation produced by the implantation of Kr ions in ZnO is found to be the consequence of radiation damage because krypton is chemically inert. Very large magnetisation 185 emu/cm^3 at room temperature is observed. This was associated with a moment of ~40 Bohr magnetons per implanted krypton ion. This was found for the highest doped of Kr concentration in O-polar films. All the films made of Kr ions implanted in O-polar ZnO pass into the grains and cause different vacancies and interstitials that lead to a marked grain fragmentation. The magnetic defect bands were formed as the Zn vacancies might be attracted to the grain boundary. Results were compared from implantation in different systems, O and Zn-polar thin films and a thin ZnO crystal wafer.

XRD and EXAFS measurements were used to show that the Kr-doped O-polar ZnO films have an increased lattice spacing accompanied by a decreased grain size, which implied that the Kr atoms had been incorporated into the lattice. This means that a large amount of Kr was implanted into the grain, leading to an increase in the volume of the sample occupied by grain boundaries. However, for the Kr-doped Zn-polar film, the lattice spacing and grain size were hardly changed by the implantation, indicating that the vast majority of Kr atoms reside in the grain boundaries.

Further investigation by Raman spectra demonstrated that the scattering for the O-polar films was strong, which implies that these films were especially prone to the formation of amorphous regions [1], associated with the grain boundaries that are highly magnetic. On the other hand, Raman spectra demonstrated that the scattering for the Zn-polar film was even stronger than the O-polar, but the Zn-polar films were not magnetic.

This work indicates how the grain surface produced at the boundary region has a significant impact on the resulting magnetism. Magnetism was found not to result from the surface of nanoparticles and the Raman spectra obtained for nanoparticles is different than that usually found for implanted crystals [27]. In our case, the RTFM observed due to grain boundaries and caused by ion implantation is much larger than that of previous studies [13,14,34]. The films made of ion implanted O-polar ZnO films are especially prone to the creation of amorphous regions associated with grain boundaries which are ultimately responsible for the observed large magnetisation.

4.6 References

[1] M. Ying, A. M. A. Saeedi, M.Yuan, X. Zhang, B.Liao, X. Zhang, Z. Mei, X. Du, S. Heald, and M. Fox and G. Gehring, *Journal of Materials Chemistry* C **7**, 1138 (2019)..

[2] U. Ozgur, Y. Alivov, C. Liu, A. Teke, M. Reshchikov, S. Dogan, V. Avrutin, S. Cho, and H. Morkoc, *Journal of Applied Physics* **98**, 041301 (2005).

[3] J. Coey, *Solid State Sciences* **7**, 660 (2005).

[4] B. Roberts, A. Pakhomov, P. Voll, and K. Krishnan, *Applied Physics Letters* **92**, 162511 (2008).

[5] M. Ying, W. Cheng, X. Wang, B. Liao, X. Zhang, Z. Mei, X. Du, S. Heald, H. Blythe, M. Fox, and G. Gehring, *Materials Letters* **144**, 12 (2015).

[6] M. Ying, S. Wang, T. Duan, B. Liao, X. Zhang, Z. Mei, X. Du, F. Gerriu, M. Fox, and G. Gehring, *Materials Letters* **171**, 121 (2016).

[7] N. Hong, J. Sakai, and V. Brize, *Journal of Physics-Condensed Matter* **19**, 036219 (2007).

[8] S. Aravindh, U. Schwingenschlogl, and I. Roqan, *Journal of Chemical Physics* **143**, 224703 (2015).

[9] J. Yi, C. Lim, G. Xing, H. Fan, L. Van, S. Huang, K. Yang, X. Huang, X. Qin, B. Wang, T. Wu, L. Wang, H. Zhang, X. Gao, T. Liu, A. Wee, Y. Feng, and J. Ding, *Physical Review Letters* **104**, 137201 (2010).

[10] P. Zhan, W. Wang, C. Liu, Y. Hu, Z. Li, Z. Zhang, P. Zhang, B. Wang, and X. Cao, *Journal of Applied Physics* **111**, 033501 (2012).

[11] L. Tong, Y. Wang, X. He, H. Han, A. Xia, and J. Hu, *Journal of Magnetism and Magnetic Materials* **324**, 1795 (2012).

[12] S. Mal, T. Yang, C. Jin, S. Nori, J. Narayan, and J. T. Prater, *Scripta Materialia* **65**, 1061 (2011).

[13] T. Tietze, P. Audehm, Y. Chen, G. Schuetz, B. Straumal, S. Protasova, A. Mazilkin, P. Straumal, T. Prokscha, H. Luetkens, Z. Salman, A. Suter, B. Baretzky, K. Fink, W. Wenzel, D. Danilov, and E. *Goering, Scientific Reports* **5**, 8871 (2015).

[14] B. Straumal, S. Protasova, A. Mazilkin, E. Goering, G. Schutz, P. Straumal, and B. Baretzky, *Beilstein Journal of Nanotechnology* **7**, 1936 (2016).

[15] G. Xing, Y. Lu, Y. Tian, J. Yi, C. Lim, Y. Li, G. Li, D. Wang, B. Yao, J. Ding, Y. Feng, and T. Wu, *Aip Advances* **1**, 022152 (2011).

[16] G. Xing, D. Wang, J. Yi, L. Yang, M. Gao, M. He, J. Yang, J. Ding, T.. Sum, and T. Wu., *Applied Physics Letters* **96**, 112511 (2010).

[17] M. Zhu, Z. Zhang, M. Zhong, M. Tariq, Y. Li, W. Li, H. Jin, K. Skotnicova, and Y. Li, *Ceramics International* **43**, 3166 (2017).

[18] J. Coey, P. Stamenov, R. Gunning, M. Venkatesan, and K. Paul, *New Journal of Physics* **12**, 053025 (2010).

[19] J. Coey, M. Venkatesan, and C. Fitzgerald, *Nature Materials* **4**, 173 (2005).

[20] Y. Segawa, A. Ohtomo, M. Kawasaki, H. Koinuma, Z. K. Tang, P. Yu, and G. K. L. Wong, *Physica Status Solidi B-Basic Research* **202**, 669 (1997).

[21] L. Li, M. Jurkovic, W. Wang, J. Van Hove, and P. Chow, *Applied Physics Letters* **76**, 1740 (2000).

[22] Y. Lu, Y. Dai, M. Guo, L. Yu, and B. Huang, *Physical Chemistry Chemical Physics* **15**, 5208 (2013).

[23] X. Ke, F. Shan, Y. S. Park, Y. Wang, W. Zhang, T. W. Kang, and D. Fu, *Surface & Coatings Technology* **201**, 6797 (2007).

[24] F. Manjon, B. Mari, J. Serrano, and A. Romero, *Journal of Applied Physics* **97**, 053516 (2005).

[25] C. Bundesmann, N. Ashkenov, M. Schubert, D. Spemann, T. Butz, E. M. Kaidashev, M. Lorenz, and M. Grundmann, *Applied Physics Letters* **83**, 1974 (2003).

[26] F. Reuss, C. Kirchner, T. Gruber, R. Kling, S. Maschek, W. Limmer, A. Waag, and P. Ziemann, *Journal of Applied Physics* **95**, 3385 (2004).

[27] P. Chand, A. Gaur, and A. Kumar, *Journal of Alloys and Compounds* **539**, 174 (2012).

[28] R. Kumari, A. Sahai, and N. Goswami, *Progress in Natural Science-Materials International* **25**, 300 (2015).

[29] D. Raymand, T. Jacobsson, K. Hermansson, and T. Edvinsson, *Journal of Physical Chemistry* C **116**, 6893 (2012).

[30] J. Serrano, F. Manjon, A. Romero, A. Ivanov, M. Cardona, R. Lauck, A. Bosak, and M. Krisch, *Physical Review* B **81**, 174304 (2010).

[31] S. Lautenschlaeger, J. Sann, N. Volbers, B. Meyer, A. Hoffmann, U. Haboeck, and M. Wagner, *Physical Review* B **77**, 144108 (2008).

[32] J. Serrano, A. Romero, F. Manjon, R. Lauck, M. Cardona, and A. Rubio, *Physical Review* B **69**, 14, 094306 (2004).

[33] Q. Feng, W. Dizayee, X. Li, D. Score, J. Neal, A. Behan, A. Mokhtari, M. Alshammari, M. Al-Qahtani, H. Blythe, R. Chantrell, S. Heald, X. Xu, M. Fox, and G. Gehring, *New Journal of Physics* **18**, 113040 (2016).

[34] B. Straumal, A. Mazilkin, S. Protasova, A. Myatiev, P. Straumal, G. Schutz, P. van Aken, E. Goering, and B. Baretzky, *Physical Review* B **79**, 205206 (2009).

[35] C. Song, F. Zeng, K. W. Geng, X. J. Liu, F. Pan, B. He, and W. S. Yan, *Physical Review* B **76**, 045215 (2007).

[36] T. Gupta and W. Carlson, *Journal of Materials Science* **20**, 3487 (1985).

Chapter 5 **Cobalt and Europium Implanted ZnO Thin Films Grown by PLD**

5.1 Introduction

In the previous chapter, the investigation of magnetisation, due to defects created during ion implantation, in Krypton implanted ZnO films is described. The implanted films were not annealed since Kr is non-magnetic and the magnetisation produced from defects was the focus of the investigation. In this chapter, the aim is to investigate the interaction when codoping Co 3*d* and Eu 4*f* electrons in ZnO (O-polar) by ion implantation and beginning by attempting to reproduce the results of Lee *et al* [1]. This is a very interesting result, due to the observation of RTFM associated with a large coercive field, which is extremely high compared to the others that were reported in the diluted magnetic oxides [1]. This will provide us with a good starting platform. Co and Eu-doped ZnO as implanted will have inherent magnetism from Co and Eu but also that which arises from defects created during ion implantation. Secondly, the effect of different thermal annealing on the structural and magnetic properties in ZnCoO, ZnEuO, ZnCoEuO films is investigated. It was found that the damaged crystalline regions, created during ion implantation, can be recovered by annealing at high temperatures. The effect of the annealing on the structural and magnetic properties was investigated in order to find the minimum temperature required to recover the defects. The annealing was performed at temperatures low enough such that the migration of Co into metallic Co clusters could not be facilitated. Next, the previous studies of Co and codoped CoEu implanted ZnO thin films will be discussed, followed by the results.

5.2 Previous Studies of Co and Codoped Co and Eu Implanted ZnO Films

DMS have attracted increased interest because of their potential use in the development of spintronics [2]. Previous works and results of RTFM in Co-doped ZnO films, made by various techniques such as PLD, Sol-Ge, MBE...etc, will be reported and discussed alongside our findings in Chapter 6. It has been suggested that, by codoping two magnetic transition metals, such as Fe and Co [3], it may be possible to increase the saturation magnetisation in ZnO systems. Rare earth (RE) elements, in comparison to TMs, have a high 4*f* spin orbit magnetic moments thus may provide stronger anisotropy magnetism. RE ions such as (Gd [4], Er[5], and Nd[6]), when doped in DMSs, have attracted a large amount of interest as Gd-doped GaN in particular has been found to exhibit a colossal magnetic moment [7]. Unfortunately, the paramagnetic behaviour reported in Gd/Sm and Mn-codoped ZnO was found to be related to the secondary phase formed in RE oxides [8]. In addition, the much larger radius of RE atoms limits their solubility in ZnO due to the lattice distortion required. Due to the high magnetic moment that can be generated from the 7 unpaired electrons in the *4f* orbital, Eu^{2+}. It is considered as a good candidate as a dopant in ZnO in order to obtain high magnetization in DMS.

As was discussed in Subsection 3.2.3, ion implantation is a technique used to create semiconductor materials, which allow for precise control of the doping concentration. It is desirable to control precisely the dose of magnetic elements in the ZnO matrix and as such, this technique has been widely used in DMSs such as TM [9-11] and RE-doped ZnO [4]. Those results reported however still remain controversial since Co is well known to aggregate and form clusters [12] and point defects [13].

Akdogan *et al* investigated Co-doping in ZnO, through ion implantation and reported that the magnetic properties in some films could convert between paramagnetism and ferromagnetism, depending on the Co ion concentration [11]. They noted that there are two magnetic phases, where one is due to the magnetism of Co substituted on Zn sites while the other is due to Co clustering. The occurrence of cobalt clustering is frequently observed in the ZnCoO thin films prepared by the ion implantation technique [14-16]. The films became ferromagnetic when the Co ion dosage increased from 2.5×10^{16} to 2×10^{17} cm^{-2}. Borges *et al* also studied Co implanted in ZnO but in single crystal, with fluences of 2×10^{16} and 1×10^{17} cm^{-2} at an implantation energy of 100 keV, annealed in vacuum. The RTFM observed was also found to result from the formation of Co clusters [14]. Sn-doped ZnO substrates implanted with Co, with fluences of 3×10^{16} and 5×10^{16} cm^{-2} at an implantation energy of 250 keV, were also found to have cobalt clustering which was responsible for the observed RTFM [15]. However, these studies cannot exclude the contribution of Co substituted on Zn site to the observed magnetism [14,15]. In a more promising study by Photongkam *et al* [17], who suggested that the cobalt nanoparticles can be limited by codoping with the rare earth element. The first-principles calculations, using density functional theory (DFT) [18] has verified it. Nevertheless, no clear mechanism of the origin of the magnetism and in a recent effort to understand this, the interaction between 3*d* and 4*f* elements in the codoping systems has been investigated by Lee *et al* [1]. In Lee *et al*, the observed structural and magnetic properties of ZnO films implanted with Co and Eu, with no metallic Co present, are discussed.

The films of 4% Co, 4% Eu doped and codoped ZnO thin films were made by ion implantation using an accelerated voltage of 30 kV and 45 kV respectively, in order to achieve an average implantation depth of 15 nm. The films were then annealed for 30 min in flowing argon at 600° C. The XRD patterns in Fig 5.1, show the resulting diffraction peaks for pure ZnO and those implanted, all films show a *c* axis out of plane orientation with only (002) and (004) peaks. No secondary phases, for example from Co clustering and Co or Eu corresponding oxides, was detected in the sample within the detection limit. Raman spectra measurements were also carried out alongside XRD and no secondary phases were found.

Removed
by the author
for copyright reasons

Figure 5.1 XRD patterns taken on ZnCoO, ZnEuO, and ZnCoEuO thin films, taken from [1].

Fig 5.2 shows the (M-H) field curves that were measured at 300 K and 5 K for both the undoped and implanted ZnO films. The hysteresis loops at 300 K and 5 K were clearly exhibited in both mono-doped and codoped ZnO films, which demonstrate RTFM. The inset shows the diamagnetic magnetisation from the undoped ZnO measurement using the SQUID. The saturation magnetisation M_s for ZnCoO, ZnEuO, and ZnCoEuO are 7 emu/cm^3, 9 emu/cm^3, and 18.2 emu/cm^3 at RT whilst 8.5 emu/cm^3, 11 emu/cm^3, and 28.6 emu/cm^3 at 5 K, respectively. The M_s of ZnCoEuO samples is larger than the sum of both the Co and Eu mono doped samples together, which implies that the magnetic contribution is complex. The coercivity (H_c) of ZnCoO, ZnOEuO, and ZnCoEuO films are 150 Oe, 286 Oe and 1200 Oe at 300 K and 200 Oe, 370 Oe and 1340 Oe at 5 K respectively. Lee *et al* [1] concluded that ferromagnetism might result from the exchange interaction between Co (3d) electrons that localised carriers induced by Eu^{3+} ion codoping.

Removed
by the author
for copyright reasons

Figure 5.2 M-H curves taken on ZnCoO, ZnEuO, and ZnCoEuO thin films at 300 K (**a**) and 5 K (**b**) the insets show the magnetic behaviours of undoped ZnO at 5 K and 300 K [1].

5.3 Experimental Detail, Result and Discussion

The structural properties of the Co, Eu and codoped CoEu implanted films were studied using X-ray diffraction (XRD) and Raman spectroscopy. Measurements were carried out at the Department of Materials Science and Engineering at the University of Sheffield. The X-ray absorption fine structure spectroscopy measurements were obtained by our collaborator Steve Heald at the Advanced Photon Source in the Argonne National Laboratory, USA. The magnetic properties were characterised using a SQUID magnetometer and were carried out at the Department of Physics and Astronomy at the University of Sheffield.

5.3.1 Growth of Thin Films

5.3.1.1 Sample Preparation of ZnO Thin Films

Two sets of 15 pure ZnO (O-polar) thin films were grown in similar growth conditions in different laboratories. In both laboratories, the films were grown at the same oxygen pressure of 1×10^{-2} Torr and the same temperature at 500^{o} C by PLD. The first set was grown in our laboratory with a xenon chloride (XeCl) excimer laser at University of Sheffield as discussed in Section 3.2 whereas the second set of films were grown with a krypton fluoride (KrF) excimer laser by our collaborator Marzook Alshammari at King Abdulaziz City for Science and Technology, KACST, Saudi Arabia. This allowed us to implant twice as many films that could otherwise have been produced in our laboratory at The University of Sheffield. This is also advantageous because growing the films at different sites, and reproducing the results, is a good quality control measure.

A high-purity ZnO powder was used to produce the pure ZnO target for PLD. The powder was purchased from Alfa Aesar and had a purity of 99.999% ZnO. The powder was mixed and ground with a mortar and pestle for more than 15 minutes. Next, this powder was placed in a high-quality alumina crucible and annealed for 12 hours at 300^{o} C in air. This powder was then remixed in the mortar and pestle for 20 minutes and reannealed for 12 hours at a higher temperature of 600^{o} C. The powder was again re-ground and reannealed for 12 hours at 900^{o} C. A commercial Specac die of internal diameter 25 mm, was used in conjunction with a manual hydraulic bench-press to compress the powder to a pressure of 25 kPa. This was a necessary step to produce a cylindrical, dense pellet that was 25 mm in diameter and 5 mm in thickness. The target was then finally sintered at 900^{o} C for 13 hours in order to produce a target with a smooth surface.

This target was used to produce pure ZnO films by PLD as discussed in Subsection 3.2.2.1. Films were made with a series of deposition steps in order to obtain the desired thickness of ~100 nm. This meant depositing once for a short time and checking the thickness and then repeating this process until the desired thickness is reached. The films were deposited on a sapphire substrate, purchased from PI-KEM Ltd as double-sided, polished, single-crystal *c*-cut Al_2O_3 as discussed in Section 3.6.

The polarity of ZnO thin films is important when producing defects by ion implantation since their magnetic properties are well known to be influenced by the polarity of the surface [19,20]. In polar films, made in Chapter 4 via MBE, it was discovered that those with an O-polar surface were magnetic whereas those implanted into a Zn-polar film were not magnetic [19,20]. The films grown *via* PLD may be either Zn-polar or O-polar or a mixture of the two. The polarity of the films was determined using photoluminescence after MgZnO was deposited on the samples by our collaborator Yutaka Adachi at National Institute for Materials Science, Japan. The Mg content of the resulting film depends on the polarity of the surface [21]. This is due to the sticking coefficient of the O-polar surface being higher than that of the Zn-polar. The photoluminescence was then measured and the wavelengths of the near band edge emission peak from our two undoped ZnO samples were similar and ranged between 327- 330 nm. This means that the films have the c (-)-polarity and subsequently the films must be O-polar. Thus, Co and Eu doped and codoped were implanted into ZnO O-polar thin films as discussed in the next subsection. If however, the films had c (+)-polarity, the peak would have been observed at around 340-350 nm and the film would be Zn-polar [21].

5.3.1.2 Sample Preparation of ZnO implanted with Co, Eu, and Codoped CoEu

Co and/or Eu ions were implanted into the ZnO films using the ion implantation method by our collaborator Nianhua Peng at Ion Beam Centre, Surrey University, Surrey UK. Prior to the implantation, the Stopping and Range of Ions in Matter (SRIM) programme was employed to optimise the stopping powers and implantation depth of both ^{59}Co and ^{152}Eu ions. The accelerated voltage of 30 KeV and 45 KeV for ^{59}Co and ^{152}Eu ions respectively was required in order to create an implantation depth of 15 nm in the ZnO thin film. The fluence of implanted Co and Eu ions in ZnO is regulated at 3.3×10^{15} Co/cm^2 and 2.2×10^{15} Eu/cm^2 which effectively corresponds to a Co and Eu nominal concentration of 4% in the implanted region of the ZnO film to follow the procedure used by Lee *et al* [1]. Therefore, Co, Eu doped and codoped CoEu ZnO thin film were prepared. These films will be denoted as ZnCoO and ZnEuO, ZnCoEuO respectively. For the codoped sample of CoEu, Co ions were implanted first followed by Eu ions.

5.3.2 Annealing Regimes

The structural and magnetic properties of the films were studied as implanted and as annealed at different temperatures in both vacuum and air. First, the aim was to follow the work by Lee *et al* [1], who annealed ZnCoO, ZnEuO, and ZnCoEuO after implantation in an Ar atmosphere at 600^o C for 30 minutes. The interesting about the work was that high ferromagnetism associated with high coercivity was observed. Lee *et al* claimed that no metallic Co was detected in the system. Thus, the films were annealed under the same conditions at 600^o C for 30 minutes in vacuum to compare it with the work by Lee *et al*. The results showed that annealing in vacuum gives an immense amount of metallic cobalt, which is also found by others [15, 16].

Hence, the origin of the magnetisation is the metallic cobalt, which is not useful in real applications. The results of Lee *et al* [1] could not be reproducible and there is no published record of anyone achiving similar results. Secondly, the aim was to find the minimum temperature required to recover defects and to reduce the amount of the metallic cobalt. Thus a series of different annealing temperatures, 200° C, 300° C, 400°C, 500° C, and 600° C were used and all the films were annealed for 1 hour in air. The annealing temperatures used for the ZnCoO and ZnEuO samples were 200° C, 300° C, 400° C, 500° C, and 600° C, ZnCoEuO was only annealed at 600° C.

The damaged region leads to defects which increase the magnetisation and annealing allows us to investigate their importance. The crystalline structure of the damaged region caused by ion implantation was indeed recovered via thermal annealing at 600° C, and no Co clusters or their related oxide phases were observed.

5.3.3 Structural Properties of Undoped ZnO, Implanted Films for Both as Implanted and Annealed Films

Structural properties were analysed for all undoped ZnO films, ZnCoO, ZnEuO and ZnCoEuO as grown and after annealing. The *c* lattice constant, and the grain sizes were obtained from XRD measurements at the University of Sheffield. This was essential to observe the effect of Co, Eu and CoEu implantation on ZnO thin films made by PLD at the University of Sheffield. The XANES and EXAFS measurements were taken by Steve Heald at the Advanced Photon Source in the Argonne National Laboratory, USA. Raman Spectra measurement was carried out in The Department of Materials Science and Engineering at the University of Sheffield.

5.3.3.1 X-Ray Diffraction Measurements (XRD)

All the XRD measurements were made using the apparatus described in Subsection 3.3.1 using CuK$_\alpha$ radiation (λ=1.5406 Å). Figure 5.3 shows typical XRD measurements of all the films of undoped and ZnO as implanted, which exhibit a single phase with a wurtzite ZnO structure, showing a *c* axis out of plane orientation with only (0002) and (0004) ZnO diffraction peaks. The (0006) diffraction peak is from the sapphire substrate, marked S in Fig 5.3. No secondary phases were observed within the detection limit of the XRD measurement, indicating ZnCoO, ZnEuO, and ZnCoEuO films were free of secondary phases.

The Debye-Scherrer formula was used to estimate the grain sizes, as explained in Section 3.3.1. The two sets of undoped ZnO films were made in Sheffield and KACST, the lattice constants were calculated respectively which are 5.206 ±0.002 Å and 5.205±0.002 Å with grain sizes of 41±4 and 39±4 nm. These were sufficiently close for us to use the average in all subsequent measurements.

The XRD spectra of undoped ZnO films show a strong and sharp (0002) diffraction peak, which implies that the undoped ZnO film was well crystallised. This (0002) peak is broader with a small right shift toward the higher diffraction angle in ZnCoO film as implanted; demonstrating that the *c* lattice parameter undergoes a shrinkage due to Co-dopants. The *c* lattice parameter reduced from 5.205 Å in the undoped ZnO film to 5.201 Å in ZnCoO as implanted and it further decreases to 5.198 Å after annealing at 600 °C in air. The substitution of the Zn^{2+} ions with high-spin Co^{2+} ions results in a tetrahedral structure with a reduction in the *c* lattice parameter and a large compressive strain [22]. This is because the Co^{2+} ions have a radius of 0.58 Å which is slightly smaller than the Zn^{2+} ions of radius 0.60 Å [22]. This is in good agreement with the calculation of the strains because the sign of ZnCoO was negative, as shown in table 5.1. The strain is defined as $\frac{d_1 - d_2}{d_2} \times 100$, where d_1 is the lattice spacing for implanted ion into ZnO thin film, d_2 is the lattice spacing for pure ZnO thin films.

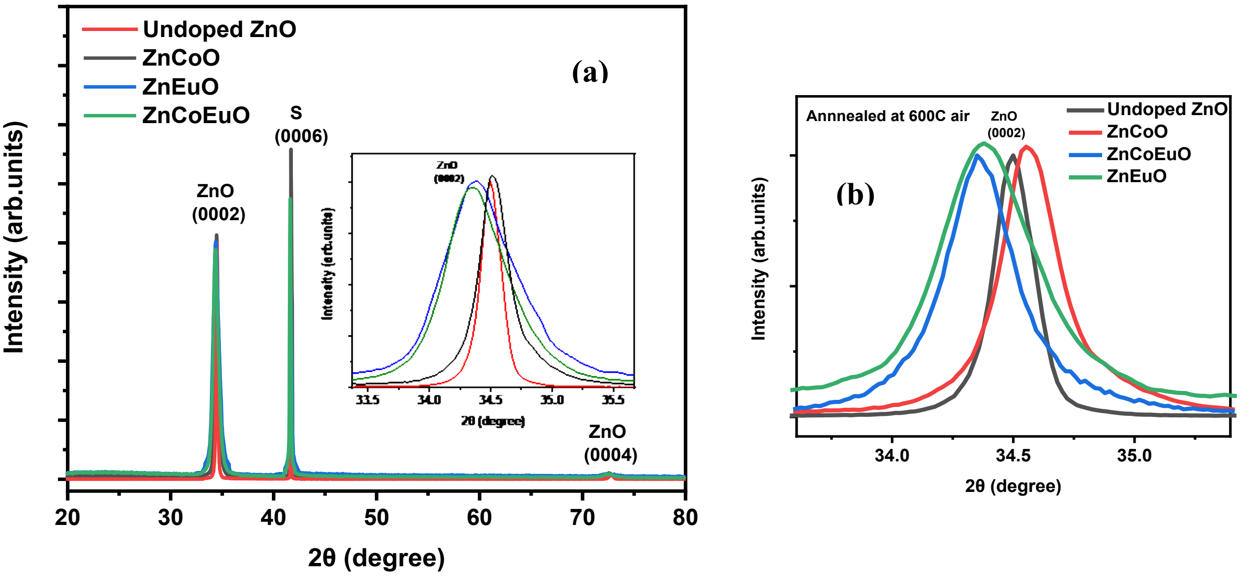

Figure 5.3: (a) XRD data of undoped ZnO films and Co, Eu and CoEu implanted ZnO films, where S stands for the sapphire peak (0006). The inset shows the (0002) peak for implanted films, **(b)** the (0002) peak for the implanted films which were annealed at 600° C.

Table 5.1: The summary of the calculated strains implanted ZnCoO, ZnEuO, and ZnCoEuO and after annealing at 600° C in air.

Samples	**Condition**	**Strains %**
ZnCoO	As implanted	- 0.07
ZnEuO	As implanted	0.23
ZnCoEuO	As implanted	0.34
ZnCoO	After annealed	-0.13
ZnEuO	After annealed	0.15
ZnCoEuO	After annealed	0.30

However, the introduction of Eu ions into the ZnO film causes the (0002) peaks to shift towards a lower diffraction angle. In this case, the *c* lattice parameter expands from 5.205 Å in ZnO to 5.217 Å in ZnEuO as implanted and it further shifted to 5.213 Å after annealing at 600 ºC in air. The incorporation of both Co and Eu ions in the ZnO lattice causes the ZnO (0002) peak to shift to a lower angle, indicating a net *c* axis expansion from 5.205 Å to 5.223 Å and it further shifts to 5.221 Å after annealing at 600 ºC in air. It is understandable that the addition of large Eu ions into ZnCoO can result in a larger *c* lattice parameter than that of Co-implanted ZnO. This suggests that the substitution of large Eu ions on to the small Zn ion sites in ZnO induces considerable lattice distortion within the grains [23]. This is due to the much larger ions of Eu^{2+} and Eu^{3+}, which have radii 1.17 Å and 1.03 Å respectively [24] when compared to Zn^{2+}, 0.60 Å.

The increase of the FWHM (0002) peak of ZnEuO and ZnCoEuO samples, when compared to the undoped ZnO (0002) peak, gives clear evidence for direct substitution of Eu on Zn sites. The expansion of the FWHM increases when ZnO is implanted with Eu and CoEu and small grain size is observed in ZnCoO, ZnEuO, and ZnCoEuO, as shown in Table 5.1. This suggests that a large number of these atoms were implanted into the grains rather than being confined to the grain boundaries, similar results were observed previously in Chapter 4 when Kr was implanted in ZnO thin films. The FWHM of the (0002) peak of all the annealed films decreased. This indicates that ion implantation was responsible for the damage in the ZnO host material and that the ordered crystal structure of the damaged region might be recovered by annealing at 600º C in air for 1 hour.

The FWHM of the (0002) peak in the ZnCoEuO film decreases compared to that of the ZnEuO film. This might suggest that Eu and Co ions couple in order to compensate for inhomogeneous strain implying that some subtle interaction between Co and Eu ions in the codoped materials might exist. This combination of tensile and compressive strain resulting from the individual doping of Co and Eu minimises the system energy [17].

Table 5.2: The summary of the information obtained from the XRD measurements such as the lattice parameter, FWHM of ZnO (0002) and the grain size for all the films: undoped ZnO, as implanted films ZnCoO, ZnEuCo, and ZnCoEuO and after annealing. The observed shifts of the XRD reflections due to the implantation should be regarded as an underestimate of the effects of implantation.

Samples	**The lattice constant (±0.002 Å)**				**FWHM(±0.005 degree)/Grain size ((±4 nm)**			
	undoped	**ZnCoO**	**ZnEuO**	**ZnCoEuO**	**undoped**	**ZnCoO**	**ZnEuO**	**ZnCoEuO**
As implanted	5.205	5.201	5.217	5.223	0.22/40	0.31/36	0.67/12	0.59/14
Annealed at 600^{0}C in air	-	5.198	5.213	5.221	0.22/40	0.27/32	0.49/18	0.33/26

5.3.3.2 X-ray Absorption Fine Structure Measurements; XANES and EXAFS

XANES measurements for the films were taken to investigate the ionisation state of the Co and Eu ions since this measurement can detect the existence of metallic Co and any secondary oxide phases. First, the percentage of the metallic Co in the films with Co ions present is investigated. Secondly, the ionization state of Eu is investigated in order to determine whether it is in the Eu^{2+} or Eu^{3+} state in the films. Finally, EXAFS measurements were taken to check if Eu was substituted on Zn sites in ZnO.

Fig 5.4 (a) shows a typical comparison of XANES data of the standard valence states of pure metallic Co, annealed ZnCoO, ZnCoEuO films, and one sample that has Co fully substituted on Zn sites as a reference. The peaks of ZnCoO and ZnCoEuO films are similar to the fully substituted sample. However, all the samples have some Co metal as indicated by the arrow near edge region ~ 7712 eV which is the most sensitive to the metal. The increased signal in the area means that the films contain some fraction of metallic contributions. This can be estimated using the Athena and Artemis interfaces program package[25]. For ZnCoO and

ZnCoEuO films as implanted, the percentage of metallic Co is estimated to be ~ 18 and 27 respectively. In addition, after annealing these films at 600ºC in a vacuum, the percentage of metallic Co increased to 29% ±2 and 45% ±2 respectively. On the other hand, the ZnCoO and ZnCoEuO samples, which were annealed at 600 ºC in air, have no metallic Co so that all the Co substituted on Zn sites. The ZnCoO sample that was annealed at 500 ºC in air contained a small amount of metallic Co. Since a large increase of metallic Co was observed in these films after annealing at 600 ºC in a vacuum, no further investigation in these films was required. This is because all the magnetisation would be due to the metallic cobalt. The result of Lee *et al* [1] is not reproducible. After an extensive literature search, it appeared that no other groups had reproduced similar results to those of Lee *et al.* However, there was no detection of Co metal after annealing the films in air at 600 ºC in the samples described here and therefore the magnetic properties were investigated further.

Fig 5.4 (b) shows a typical comparison of Eu XANES data of ZnEuO, ZnCoEuO films, and $EuTiO_3$, where the Eu in the latter should be all in Eu^{2+}. The measurement shows that ZnEuO and ZnCoEuO films as implanted indicate a mixture of Eu^{2+} and Eu^{3+}, where the Eu valence was estimated by assuming the Eu^{2+} signal is the same as for the $EuTiO_3$ standard. For as implanted films, a mixture of 35% Eu^{2+} and 65% Eu^{3+} was found for ZnEuO film and similarly for ZnCoEuO film a mixture of 31% Eu^{2+} and 69% Eu^{3+}. For films that were annealed at 600 ºC in vacuum, it was determined that the ZnEuO film contained a mixture of 22% Eu^{2+} and 78% Eu^{3+} and similarly the ZnCoEuO film contained a mixture of 19% Eu^{2+} and 81% Eu^{3+}. However, both ZnEuO and ZnCoEuO films that were annealed at 600 ºC in air were in the Eu^{3+} state and this was also observed by Sakaguchi *et al* [26]. The films were annealed in air in order to attempt to increase the oxygen level to that required for a stoichiometric film. Annealing at high temperature is likely to also have undesirable effects of causing aggregation of Co ions and migration of the Eu to the grain boundaries. The ZnEuO film that was annealed at 200 ºC in air had some Eu^{2+} contribution. The result is in good agreement with that of Sakaguchi and it implies that the temperature of the post annealing of Eu implanted ZnO plays an important role in ionisation state of Eu in ZnO sites [26].

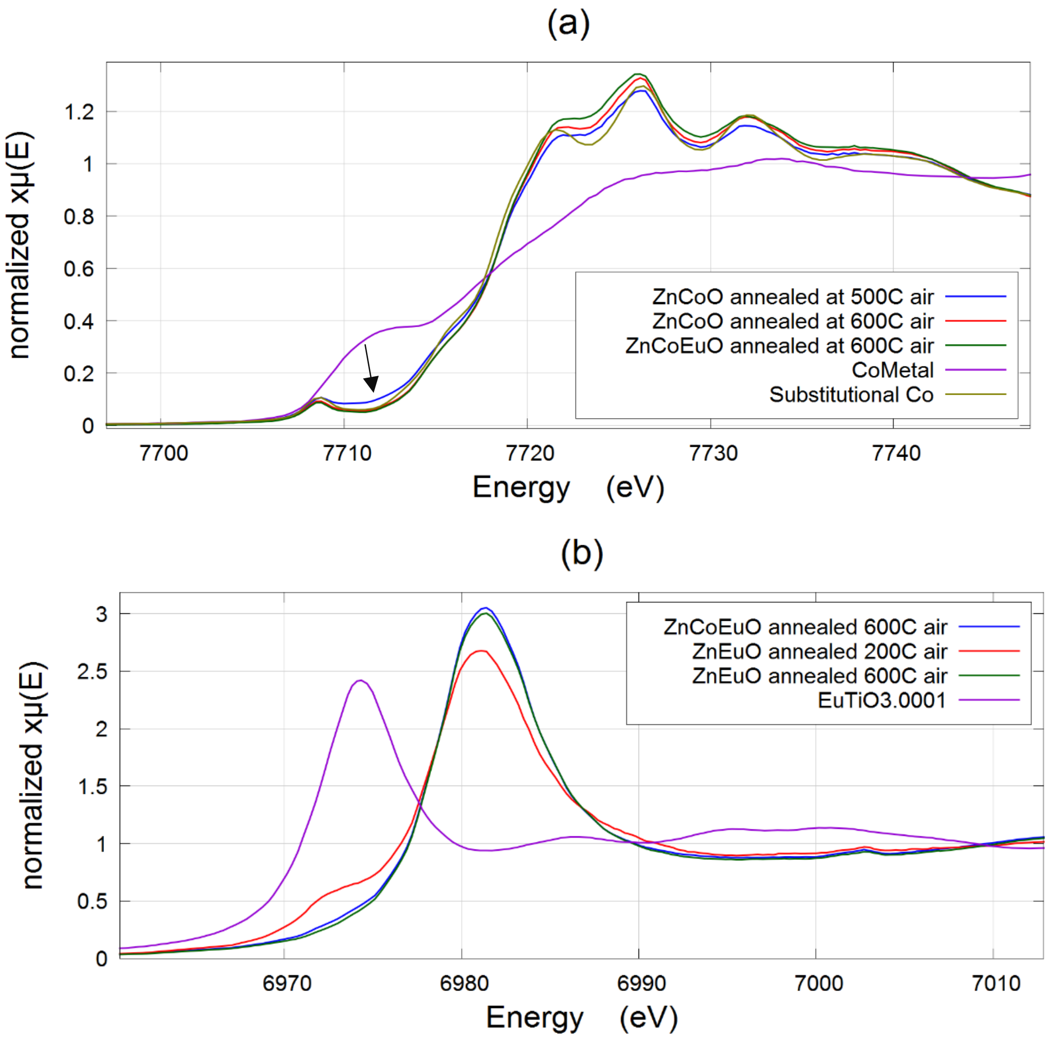

Figure 5.4: (a) Eu XANES data of pure metallic Co, and a model that has Co2+ fully substituted on Zn sites, which is used as a reference to compare with ZnCoO, ZnCoEuO films annealed at 500 oC and 600 oC in air for 1 hour. The near edge region ~ 7712 eV, which is indicated by the arrow, is the most sensitive to the Co metal. (**b**) XANES data of $EuTiO_3$, which has all Eu in the form of Eu^{2+} compared with annealed ZnEoO and ZnCoEuO at 200 ºC and 600 ºC in air, data was taken by Steve Heald.

The EXAFS measurement of the ZnEuO film as implanted was fitted with Eu substituted on Zn sites in ZnO as shown in Fig 5.5. The result shows there is a good fit with a lot of expansion in the lattice. The Eu-O distance increased to 2.28 Å from 1.98 Å in ZnO, and the Eu-Zn distance increased to 3.36 Å from 3.21 Å. This makes sense due to the larger size of the Eu ion is in good agreement with the XRD data (in table 5.2), which shows a large expansion of the *c* lattice parameter. There was also a lot of disorder around Eu sites, which is as expected given the size mismatch and small grain size, implying that a substitutional fraction of the Eu ions sit at the grain boundaries.

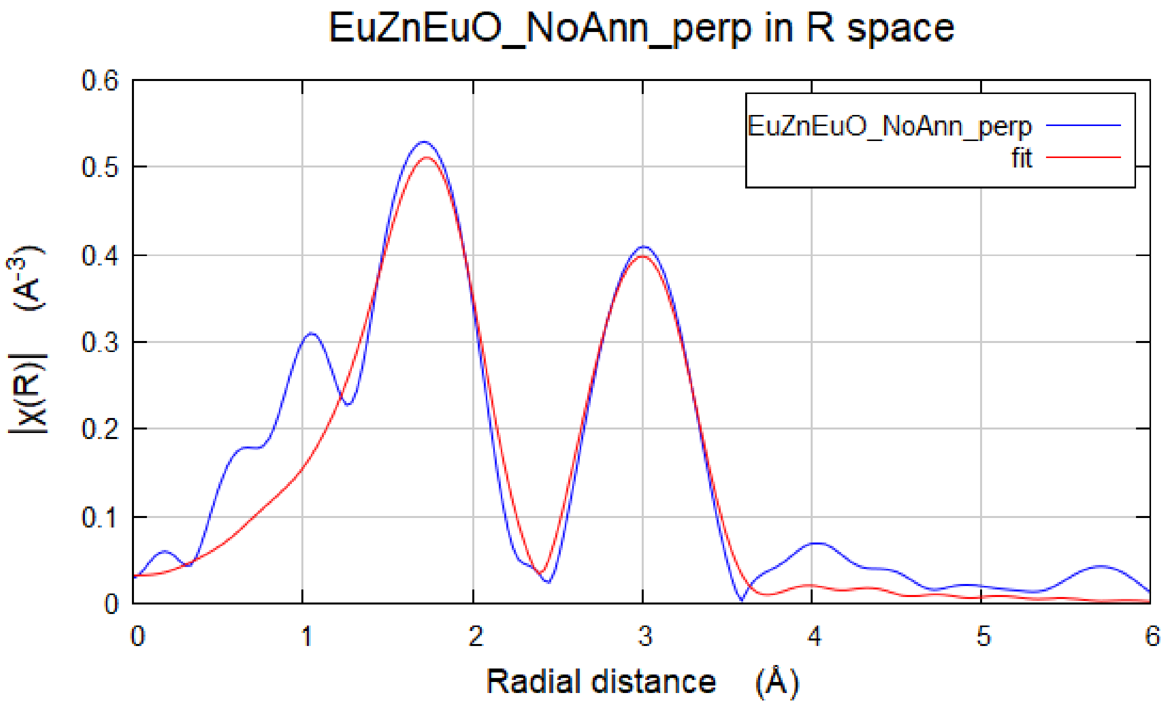

Figure 5.5: Eu EXAFS data for ZnEuO that was fitted with a model that has Zn site in ZnO, data taken by Steve Heald.

5.3.3.3 Raman Spectroscopy

Raman Spectroscopy was used to find out more about the microstructure of lattice defects in these ZnCoO, ZnEuO, and ZnCoEuO films as implanted and after annealing, and to further detect if there are any secondary phases. The primary focus here is concerned with the relation between the strong peaks arising at 580 cm^{-1} and the high broad signal appearing at about 100 cm^{-1} after annealing at various temperatures.

Two undoped ZnO films, with thickness 100 nm and 300 nm, were investigated using Raman Spectroscopy in order to understand the effect of film thickness on the well-known Raman signals at 101 cm^{-1} and 437 cm^{-1}. This measurement was performed on all the samples for wavelengths ranging from 50 to 800 cm^{-1}.

Fig 5.6 shows a selection of peaks, as discussed previously in Chapter 4, at 380 cm^{-1}, 418 cm^{-1}, 578 cm^{-1} and 752 cm^{-1}, marked S for the sapphire substrate. The two well-known peaks of ZnO are shown for undoped ZnO films, the low-frequency mode is marked E_2 (L) at 101 cm^{-1} and the second high-frequency mode is marked E_2 (H) at 439 cm^{-1}. These peaks were present in films with a thickness of 300 nm and could not be resolved in the other films with a reduced thickness of 100 nm. The undoped ZnO films show no peaks, which concludes that no secondary phases can be found within the detection limit.

All the ZnCoO, ZnEuO, and ZnCoEuO films as implanted give a higher response for all peaks in comparison to undoped ZnO but also an additional high broad signal at around 100 cm^{-1} and a second strong peak arising at ~ 580 cm^{-1}, as seen in Fig 5.7. The two signals, corresponding to the undoped ZnO film at 101 cm^{-1} and 438 cm^{-1}, are not strong enough to be seen as discussed earlier because our ZnO film is 100 nm thick as shown in Fig 5.7.

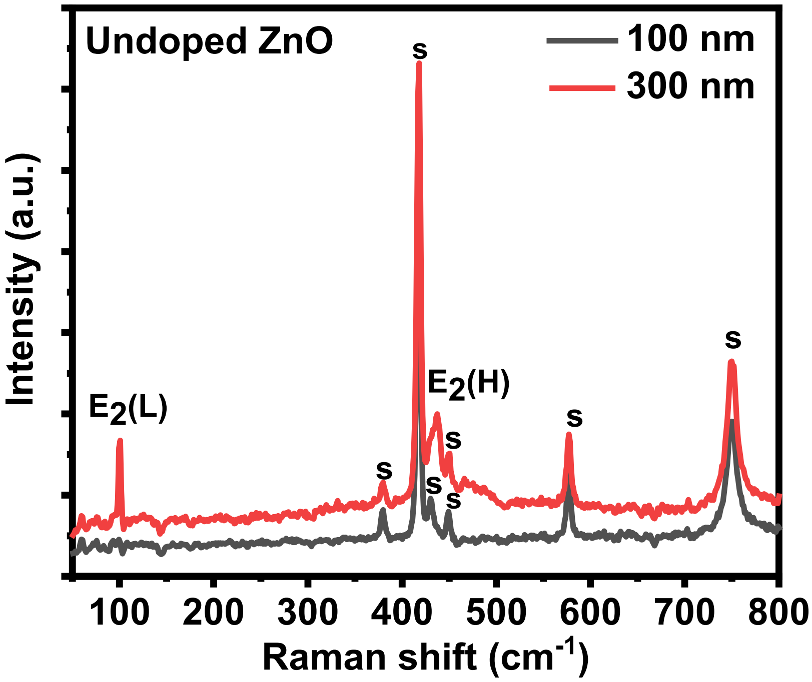

Figure 5.6: Peaks of the Raman spectra measurements for undoped ZnO films with a thickness of 100 nm and 300 nm.

The peak arising at 580 cm^{-1} has been observed in several other studies which were made on nanoparticles [27,28] and can be associated to the two Raman peaks A_1(LO) at 584 cm^{-1} and E_1(LO) at 595 cm^{-1} but not in the case of undoped film samples in the $z(xx)\bar{z}$ geometry. At 540 cm^{-1} the broadened signal, which corresponds to multi-phonon scatting, can be attributed to defects. The disorder-active A_1(LO) phonons that originate from the high density of phonon states are due to intrinsic defects in the ZnO host such as Vo or Zn_i [29,30]. The results are similar to the ones observed previously for the Kr implanted ZnO film and discussed in Chapter 4. These results indicate there are a large number of defects in our implanted films. In addition, the presence of any other vibrational modes from secondary phases was not observed.

Fig 5.7 shows the Raman Spectra measurements of all films as implanted, both ZnCoO (red) and ZnEuO (blue) gave a large response signal in comparison to pure ZnO (black) but the largest response corresponded to ZnCoEuO (green). It was noticed that implanting Co in ZnO films resulted in a larger disordering of the film, more than 60 times that of the undoped ZnO. However, implanting Eu in ZnO caused a further increase in the disordering compared to that made by the cobalt alone. This is because the mass of ^{59}Co is much less than the mass of ^{152}Eu and thus Eu will have much higher scattering.

As was mentioned earlier Co ions were implanted into ZnO thin films first and then Eu ions were implanted into ZnCoO thin films. At the range 50 cm^{-1} to 290 cm^{-1}, the effect of Eu implantation in the already disordered ZnCoO films is small. The disorder created by both Co and Eu is not equal to the sum of the disorders made by mono Co and Eu as shown in Fig 5.7. This results from the defects formed in the structure and local distortions in the lattice, which are brought about from the differing radii of Eu and Co ions and their incorporation into the ZnO wurtzite structure.

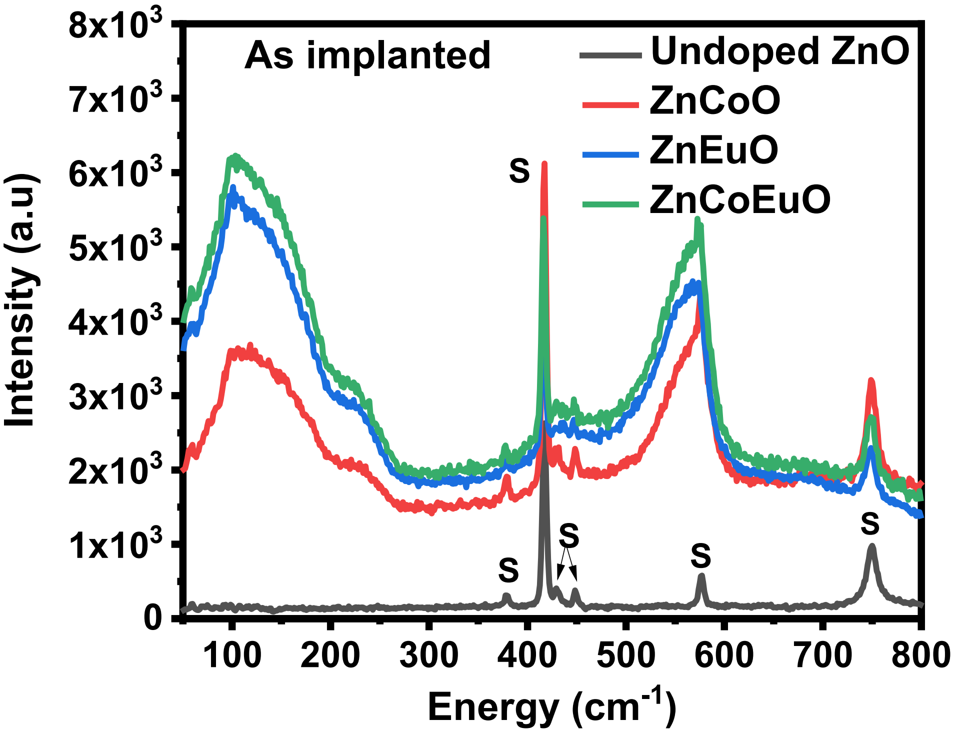

Figure 5.7: Raman spectra for the undoped ZnO and as implanted ZnCoO, ZnEuO, and ZnCoEuO.

It is interesting to compare the relative sizes of the scattering near 150 cm^{-1} with that near to 580 cm^{-1} from films containing Eu and Co. The scattering near to 580 cm^{-1}, which is due to point defects, is rather similar for all the films whereas the scattering near to 150 cm^{-1} is significantly larger for the films that contain Eu. The grain size for the implanted films containing Eu is significantly smaller than that for ZnCoO and this causes the larger scattering intensity near 150 cm^{-1} for the films that contain Eu.

The strong peak arising at ~ 580 cm^{-1} on the shoulder of the sapphire peak clearly decreases with each incremental annealing temperature as per the following 200^{o} C, 300^{o} C, 400^{o} C, 500^{o} C and 600^{o} C. For example at 600^{o} C, as seen in Fig 5.8 (a) and (b), the strong peak arising at ~ 580 cm^{-1} due to structural disorder from the amorphous region, does not appear. This suggests that the crystal structure is recovered and that there is a significant reduction in the density of defects. Also, there were no vibration modes that had not already been seen which would indicate that no secondary phases were formed after annealing for the 4% dopant level in ZnCoO, ZnEuO and ZnCoEuO films.

The largest peaks for all the films appeared at ~580 cm^{-1} and in the range between 50 cm^{-1} and 290 cm^{-1} but the biggest response was seen for ZnCoO, ZnEuO and ZnCoEuO as implanted without annealing. This must mean that the films crystalline structure was damaged during the ion implantation and the Raman spectra measurements support this since they reveal that both these peaks are reduced as the annealing temperature is increased. The two peaks are still present in ZnCoO and ZnEuO samples that were annealed at a temperature up to 500^{o} C, indicating that the thermal energy provided at the annealing stage is not enough to rid the structure of point defects produced in the ion implantation process. As the annealing temperature is increased to 600^{o} C, the disorder-active A_1(LO) phonon peaks at ~ 580 cm^{-1}, created by ion implantation, vanish which suggests a strong recovery of defects for all the ZnCoO, ZnEuO and ZnCoEuO films.

The scattering in the low energy regions ~150 cm^{-1} was reduced most strongly for the ZnCoEuO film where the XRD had indicated that annealing had caused a large increase in the grain size from 14 to 26 nm as given in Table 5.2.

Fig 5.8 (a) and (b) show the Raman spectra peaks ranged from 50-800 cm^{-1} for different films of ZnCoO and ZnEuO as implanted and post annealing at a series of different temperatures 200 ºC,300 ºC,400 ºC,500 ºC, and 600 ºC. Fig 5.8 (c) shows the Raman spectra for the ZnCoEuO film as implanted and as annealed at 600 ºC in comparison to undoped ZnO.

The element Co is known to be highly soluble, up to 40% for ZnO films, largely due to its comparable size to that of Zn^{2+}ions [31]. In a study by Jang *et al* [32] it was reported that, even at the low deposition temperature of 100 ºC, it was possible to achieve full diffusion of Co ions into the ZnO lattice. The resulting annealing treatment allowed the Co ions to be implanted throughout the entirety of the ZnO epilayer as opposed to being trapped at the damaged sites. For Eu ion, the picture is somewhat different because its solubility in ZnO is strongly limited by its much larger radius and subsequent lattice distortion. Thus, both the lattice distortions and the magnetic interactions from local impurities which result from these elements are significant factors which affect the atomic structures in these materials.

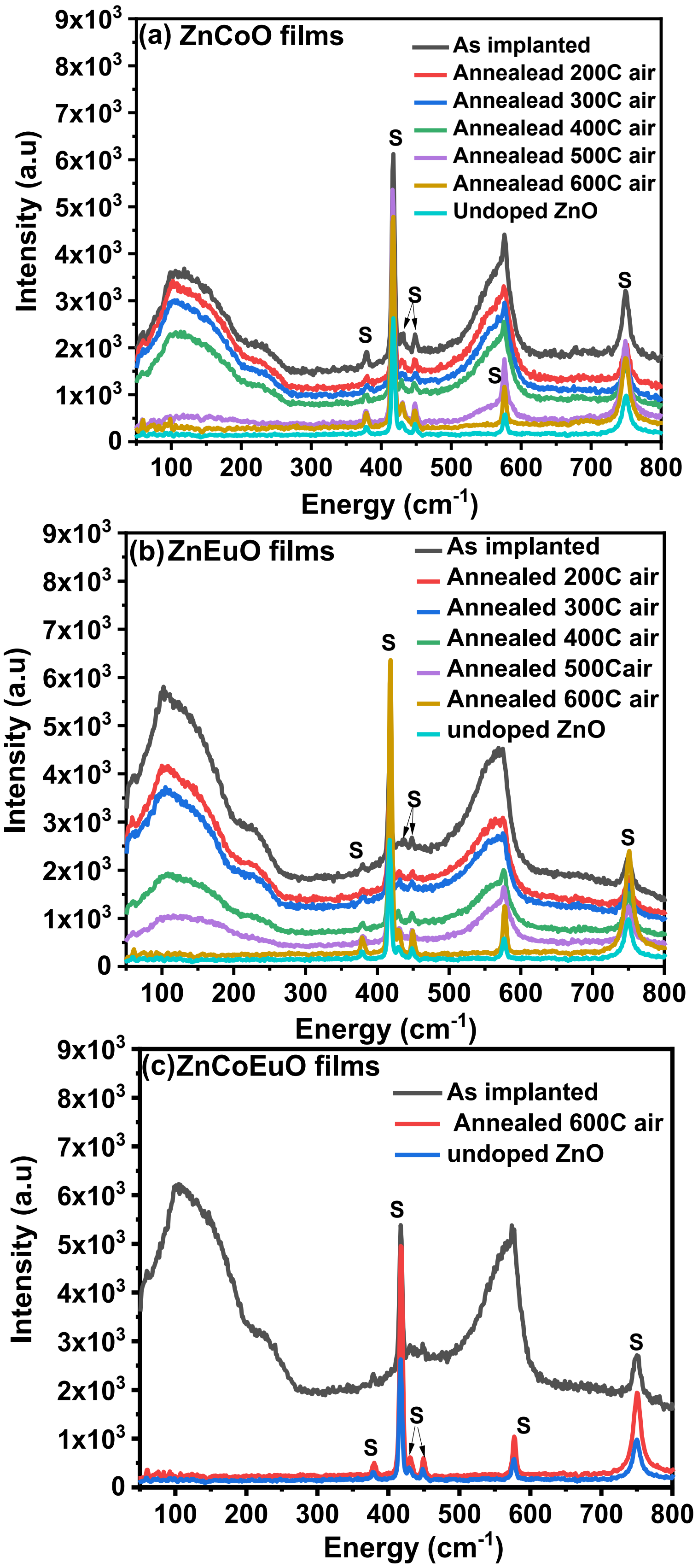

Figure 5.8: Room temperature Raman scattering spectra of undoped ZnO film and (**a**) ZnCoO, (**b**) ZnEuO, and (**c**) ZnCoEuO films annealed in air at various temperatures for 1 hour.

5.4 Magnetic Properties

Magnetic hysteresis loop measurements were taken using the superconducting quantum interference device (SQUID) at 5 K and 300 K for all implanted films before and after annealing by assuming that it was all due to the 15nm thick implanted layer. For ZnCoO, ZnEuO, and ZnCoEuO films as implanted, large ferromagnetism has been obtained which is weakly dependent of temperature, with saturation magnetisation, *Ms*, of 57, 78, and 105 emu cm^{-3} at 300 K respectively, and 60, 84, and 110 emu cm^{-3} at 5 K respectively, as summarised in Table 5.2. The *Ms* value of the ZnCoO thin film is 60 emu cm^{-3}, which is equivalent to 3.9 μ_B/Co and is larger than the theoretical values for either metallic Co or Co^{2+} of 1.74 μ_B/Co and 3 μ_B/Co respectively. The *Ms* value of the ZnEuO thin film is 84 emu cm^{-3}, which is equivalent to 5.5 μ_B/Eu. The theoretical values of the magnetic moment of Eu^{2+} and Eu^{3+} are 7μ_B and 0μ_B respectively. According to XANES, the Eu ion states are a mixture of 35% Eu^{2+} and 65% Eu^{3+}. The magnetisation is estimated due to Eu ions in our ZnEuO films to be:

$$M_{Eu} \approx 0.35 \times 7 + 0.65 \times 0 \approx 2.45\ \mu_B \quad (5.1)$$

The result of 2.45 μ_B is much smaller than the observed 5.5 μ_B, both results imply that the ferromagnetism may result from defects.

The largest *Ms* value of the ZnCoEuO thin film is 105 emu cm^{-3} at 300 K, which is lower than that observed for the highest doped concentration of Kr implanted ZnO which was 184 emu cm^{-3} as seen previously in Chapter 4. The large saturation magnetisation for ZnEuO, and ZnCoEuO as observed at room temperature are shown in Fig 5.9. This corresponds to a large magnetic moment per ion, as shown in Table 5.3. Such results imply that the observed magnetisation is due to the implantation process instead of the local moment derived from the Co, Eu-doped and codoped CoEu in the ZnO lattice, similar to the previously observed in Kr implanted ZnO. Hence, the observed magnetisation was weakly dependent on temperature, and the coercive field was low for ZnCoO and ZnEuO and ZnCoEuO, as shown in Table 5.3. Both characteristics are consistent with those caused by defects [34-36].

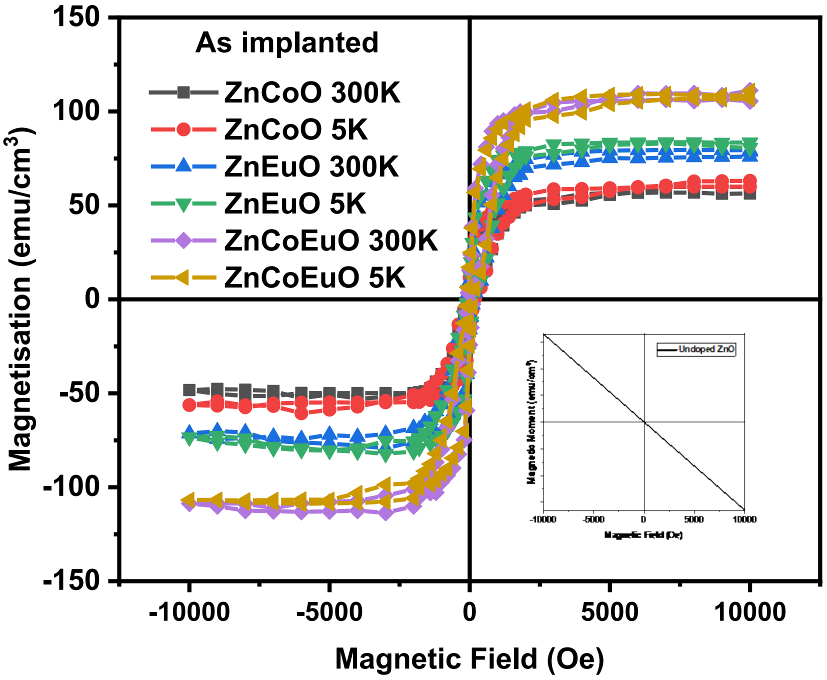

Figure 5.9: Magnetisation data, found after subtracting the diamagnetic contribution from undoped ZnO for ZnCoO, ZnEuO, and ZnCoEuO as implanted at 300 K and 5 K. The inset shows the *M/H* plot for a film of pure ZnO on sapphire.

Table 5.3 gives the value of the magnetic saturation and the magnetic moment per implanted ion for as implanted ZnCoO, ZnEuO, and ZnCoEuO films at 5 K and 300 K.

Samples	***Ms*** **(emu/cm³)**		***Ms*** **(μB/implanted atom)**		***Hc*** **(Oe)**	
	5 K	**300 K**	**5 K**	**300 K**	**5 K**	**300 K**
ZnCoO	60 ± 10	57 ± 10	3.9 ± 0.5	3.7± 0.5	110 ±11	90 ±10
ZnEuO	84 ± 10	78 ± 10	5.5 ±0.6	5.2 ±0.6	112 ±11	110 ±10
ZnCoEuO	110 ± 10	105 ± 10	7.2 ± 0.6	6.9 ± 0.6	120 ±12	100 ±10

Both XRD and EXAFS provide information about the structural characteristics of ZnCoO, ZnEuO, and ZnCoEuO films and the results show that the grain size decreased after implantation, indicating that the implanted atoms of Co and Eu were combined in the lattice.

Raman spectra clearly showed the scattering of the point defects for the implanted films, which is similar to that observed previously in Kr, implanted ZnO films. The relative size of Eu in comparison to Zn or O leads to strain in the lattice, this causes fractured grains and grain boundaries, producing the resulting magnetism [20,37]. Our result demonstrates that the observed magnetisation is almost independent of temperature, indicating that the magnetism emerged from the polarised electrons in a narrow defect band [38]. Therefore, it is likely that defect states are responsible for the observed magnetisation and that they form a band when there are near to each other and other isolated localised defects can be ignored. It is at the grain boundary that complex defects arise and grain boundary defect model theory also suggests that zinc vacancies reside there; in order to compensate for the oxygen vacancies that extend into the neighbouring grains [38,39].

For ZnCoO, ZnEuO, and ZnCoEuO films, annealed at 600 ºC in air, ferromagnetism has been obtained with saturation magnetisation, *Ms*, of 10, 12, and 20 emu cm^{-3} at 300 K respectively, and 13, 15, and 23 emu cm^{-3} at 5 K respectively, as Fig 5.10 is shown. The average coercive field is 100 Oe for all the annealed films. Raman spectra clearly showed that the scattering of the point defects, for the implanted films, decreases with increasing annealing temperature. This shows that the crystal structure is recovered, as shown previously in Fig 5.8. According to XANES, the films that were annealed at 600 ºC in air had no metallic Co or any other oxides. The observed ferromagnetism in the ZnCoEuO film is less than the sum of that from the ZnCoO and ZnEuO films. Thus, there is no evidence of interaction between the substitutions of the implanted Co (3*d*) and Eu (4*f*) electrons in the ZnO thin film, in contrast to that suggested by Lee *et al* [1]. Hence, the magnetisation is due to the substituted Co and Eu in the films.

Table 5.4: provides the magnetic saturation *Ms* for as implanted ZnCoO, ZnEuO, and ZnCoEuO and annealed at 600 °C in air.

Samples	**As implanted**				**Annealed 600 °C in air**			
	Ms **(emu/cm^3)**		***Ms*** **(μ_B/implanted atom)**		***Ms*** **(emu/cm^3)**		***Ms*** **(μ_B/implanted atom)**	
	5K	300K	5K	300K	5K	300K	5K	300K
ZnCoO	60± 10	57± 10	3.9± 0.5	3.7± 0.5	13± 3	10± 3	0.84± 0.2	0.65± 0.2
ZnEuO	84± 10	78± 10	5.5±0.6	5.2±0.6	15± 3	12± 3	0.97± 0.2	0.77± 0.2
ZnCoEuO	110± 10	105± 10	7.2± 0.6	6.9± 0.6	23± 3	20± 3	1.49± 0.2	1.08± 0.2

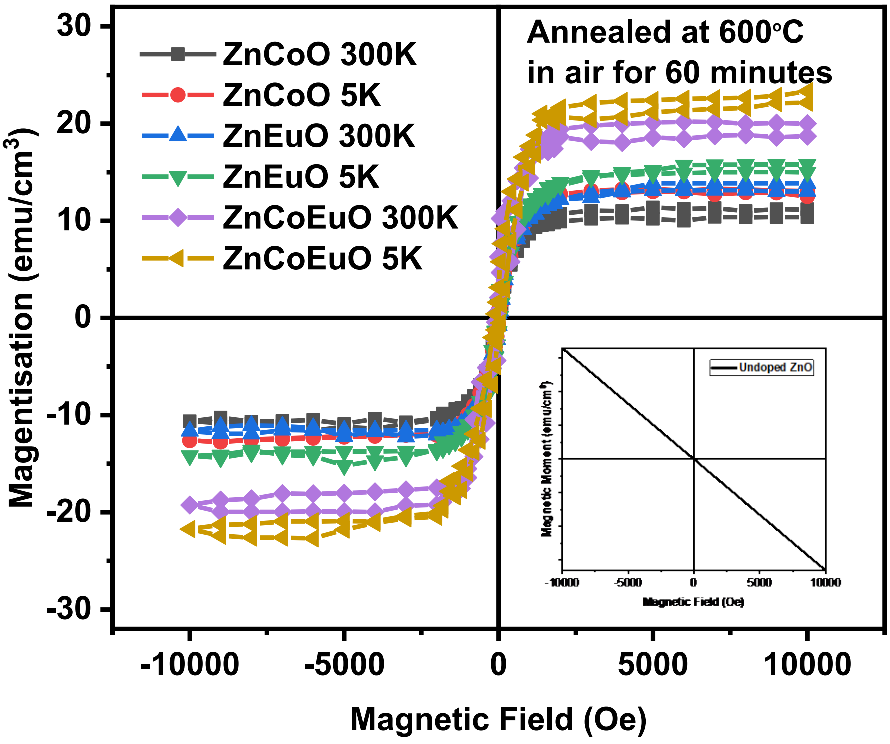

Figure 5.10: Magnetisation data, the diamagnetic contribution from the undoped ZnO, as shown in the inset, has been subtracted for annealed ZnCoO, ZnEuO, and ZnCoEuO samples at 600 °C in air at 300 K and 5 K.

5.5 Conclusions

In this chapter, the investigation of the structural and magnetic properties of all ZnCoO, ZnEuO and ZnCoEuO films as implanted and after annealing at various temperatures both in air and in vacuum is described. ZnO films have been implanted with ^{59}Co and/or ^{152}Eu ions. In order to achieve the required implantation depth of 15 nm, the accelerated energies of 30 KeV and 45 KeV for ^{59}Co and ^{52}Eu ions respectively was used. This differed from the ^{84}Kr ion implantation, where the four accelerated energies 200 KeV, 150 KeV, 80 KeV, and 30 KeV were used to create a 70 nm implantation depth. The fluence of implanted ^{59}Co and ^{52}Eu ions in ZnO was regulated at 3.3×10^{15} Co/cm^2 and 2.2×10^{15} Eu/cm^2 in order to achieve a nominal concentration of 4% of both Co and Eu respectively. Using more than one accelerated implantation energy, like that used in Kr, leads to a higher number of defects than single implantation energy and as a consequence, a much larger magnetism is induced.

Firstly, the aim of this work is to reproduce the result of by Lee *et al* [1] by following carefully the procedure outlined for investigating the interaction of codoping Co 3*d* and Eu 4*f* electrons in ZnO. They discovered a substantial coercive field, much larger than that previously reported for dilute magnetic oxides [1], with no detection of metallic Co. This was a good starting platform. However, the results of Lee *et al* [1] are not reproducible because the films that were annealed in vacuum at 600° C contained metallic Co, which dominated the magnetisation and therefore were of no interest. For the best of our knowledge, no one has reproduced such work until writing this thesis. Secondly, for the films that were annealed at 600° C in air, both defects and metallic cobalt were not detected. Thus, by annealing at a series of different temperatures, the minimum temperature needed to eliminate the defects can be investigated. These defects are seen through the damaged region, created during ion implantation, and are ultimately responsible for the observed magnetism.

Two kinds of magnetism were observed. The first and largest RTFM was observed in all the films as implanted similarly to that for Kr implanted ZnO as discussed earlier in Chapter 4 [20]. The high saturation magnetisation and Raman spectroscopy measurements revealed that the origin of the magnetisation is due to defects. The second largest RTFM was observed in the ZnCoEuO film, after annealing at 600 ºC in air for 1 hour, in which the value of *Ms* was less than the sum of both *Ms* values of the ZnCoO and ZnCoEuO annealed films. It is clearly evident that there are no strong interactions between Co (3*d*) electrons and localised carriers induced by Eu^{3+} ions, in contradiction with the results of Lee *et al* [1].

The measured magnetisation after implantation is therefore due to defects produced during the ion implantation process. Thermal annealing is essential in order to recover the damage caused to the crystalline structure during ion implantation and this can be achieved by annealing at 600 ºC in air.

The magnetisation observed for the ZnCoO and ZnEuO films annealed in air was higher than those obtained previously. The results for ZnCoO were comparable to those obtained by pulsed laser deposition. Hence, this procedure is a reliable technique for making thin layers of magnetic films. The results obtained for the ZnCoEuO films were disappointing as the results obtained in previous works [1] could not be reproduced.

5.6 References

[1] J. Lee, G. Xing, J. Yi, T. Chen, M. Ionescu, and S. Li, *Applied Physics Letters* **104**, 012405 (2014).

[2] H. Ohno, *Science* **281**, 951 (1998).

[3] D. Karmakar, T. Rao, J. Yakhmi, A. Yaresko, V. Antonov, R. Kadam, S. Mandal, R. Adhikari, A. Das, T. Nath, N. Ganguli, I. Dasgupta, and G. Das, *Physical Review* B **81**, 184421 (2010).

[4] V. Ney, S. Ye, T. Kammermeier, A. Ney, H. Zhou, J. Fallert, H. Kalt, F. Lo, A. Melnikov, and A. Wieck, *Journal of Applied Physics* **104**, 083904 (2008).

[5] J. Qi, Y. Yang, L. Zhang, J. Chi, D. Gao, and D. Xue, Scripta Materialia **60**, 289 (2009).

[6] D. Wang, Q. Chen, G. Xing, J. Yi, S. R. Bakaul, J. Ding, J. Wang, and T. Wu, *Nano Letters* **12**, 3994 (2012).

[7] S. Dhar, O. Brandt, M. Ramsteiner, V. F. Sapega, and K. H. Ploog, *Physical Review Letters* **94**, 037205 (2005).

[8] J. Das, D. Mishra, D. Sahu, and B. Roul, *Physica B-Condensed Matter* **407**, 3575 (2012).

[9] M. Schumm, M. Koerdel, S. Mueller, H. Zutz, C. Ronning, J. Stehr, D. Hofmann, and J. Geurts, *New Journal of Physics* **10**, 043004 (2008).

[10] Y. Heo, M. Ivill, K. Ip, D. P. Norton, S. J. Pearton, J. G. Kelly, R. Rairigh, A. F. Hebard, and T. Steiner, *Applied Physics Letters* **84**, 2292 (2004).

[11] N. Akdogan, H. Zabel, A. Nefedov, K. Westerholt, H. W. Becker, S. Gok, R. Khaibullin, and L. Tagirov, *Journal of Applied Physics* **105**, 8, 043907 (2009).

[12] S. Ogale, *Advanced Materials* **22**, 3125 (2010).

[13] B. Straumal, A. Mazilkin, S. Protasova, P. Straumal, A. Myatiev, G. Schutz, E. Goering, T. Tietze, and B. Baretzky, Philosophical Magazine **93**, 1371 (2013).

[14] R. Borges, J. Pinto, R. da Silva, A. P. Goncalves, M. Cruz, and M. Godinho, *Journal of Magnetism and Magnetic Materials* **316**, E191 (2007).

[15] D. Norton, M. Overberg, S. Pearton, K. Pruessner, J. Budai, L. Boatner, M. Chisholm, J. Lee, Z. Khim, Y. Park, and R. Wilson, *Applied Physics Letters* **83**, 5488 (2003).

[16] J. Wikberg, R. Knut, A. Audren, M. Ottosson, M. K. Linnarsson, O. Karis, A. Hallen, and P. Svedlindh, *Journal of Applied Physics* **109**, 083918 (2011).

[17] P. Photongkam, Y. B. Zhang, M. H. N. Assadi, S. Li, D. Yu, M. Ionescu, and A. V. Pan, *Journal of Applied Physics* **107**, 033909 (2010).

[18] M. Assadi, Y. Zhang, P. Photongkam, and S. Li, *Journal of Applied Physics* **109**, 013909 (2011).

[19] M. Ying, W. Cheng, X. Wang, B. Liao, X. Zhang, Z. Mei, X. Du, S. Heald, H. Blythe, M. Fox, and G. Gehring, *Materials Letters* **144**, 12 (2015).

[20] M. Ying, A. M. A. Saeedi, M.Yuan, X. Zhang, B.Liao, X. Zhang, Z. Mei, X. Du, S. Heald, and M. Fox and G. Gehring, Journal of Materials Chemistry C **7**, 1138 (2019).

[21] Y. Adachi, N. Ohashi, I. Sakaguchi, and H. Haneda, *Physica Status Solidi B-Basic Solid State Physics* **250**, 2122 (2013).

[22] A. Risbud, N. Spaldin, Z. Chen, S. Stemmer, and R. Seshadri, *Physical Review* B **68**, 205202 (2003).

[23] Y. Tan, Z. Fang, W. Chen, and P. He, *Journal of Alloys and Compounds* **509**, 6321 (2011).

[24] R. Shannon, *Acta Crystallographica Section* A **32**, 751 (1976).

[25] B. Ravel and M. Newville, *Journal of Synchrotron Radiation* **12**, 537 (2005).

[26] I. Sakaguchi, T. Ohgaki, Y. Adachi, S. Hishita, N. Ohashi, and H. Haneda, *Journal of the Ceramic Society of Japan* **118**, 1087 (2010).

[27] P. Chand, A. Gaur, and A. Kumar, *Journal of Alloys and Compounds* **539**, 174 (2012).

[28] R. Kumari, A. Sahai, and N. Goswami, *Progress in Natural Science-Materials International* **25**, 300 (2015).

[29] J. Ye, S. Tripathy, F. Ren, X. Sun, G. Lo, and K. Teo, *Applied Physics Letters* **94**, 011913 (2009).

[30] F. Friedrich and N. Nickel, *Applied Physics Letters* **91**, 001903 (2007).

[31] B. Straumal, A. Mazilkin, S. Protasova, A. Myatiev, P. Straumal, and B. Baretzky, *Acta Materialia* **56**, 6246 (2008).

[32] J. Yang, Y. Cheng, Y. Liu, X. Ding, Y. Wang, Y. Zhang, and H. Liu, *Solid State Communications* **149**, 1164 (2009).

[33] J. Thakur, G. Auner, V. Naik, C. Sudakar, P. Kharel, G. Lawes, R. Suryanarayanan, and R. Naik, *Journal of Applied Physics* **102**, 093904 (2007).

[34] J. Coey, M. Venkatesan, and C. Fitzgerald, *Nature Materials* **4**, 173 (2005).

[35] T. Tietze, P. Audehm, Y. Chen, G. Schuetz, B. Straumal, S. Protasova, A. Mazilkin, P. Straumal, T. Prokscha, H. Luetkens, Z. Salman, A. Suter, B. Baretzky, K. Fink, W. Wenzel, D. Danilov, and E. Goering, *Scientific Reports* **5**, 8871 (2015).

[36] Q. Feng, W. Dizayee, X. Li, D. Score, J. Neal, A. Behan, A. Mokhtari, M. Alshammari, M. Al-Qahtani, H. Blythe, R. Chantrell, S. Heald, X. Xu, M. Fox, and G. Gehring, *New Journal of Physics* **18**, 113040 (2016).

[37] M. Yuan, X. Zhang, A. M. A. Saeedi, W. Cheng, C. Guo, B. Liao, X. Zhang, M. Ying, and G. Gehring, *Nuclear Inst. and Methods in Physics Research*, B **455**, 7 (2019).

[38] C. Song, F. Zeng, K. Geng, X. Liu, F. Pan, B. He, and W. Yan, *Physical Review* B **76**, 045215 (2007).

[39] T. Gupta and W. Carlson, *Journal of Materials Science* **20**, 3487 (1985).

Chapter 6 **Thin Films of Cobalt-Doped ZnO Made by PLD**

6.1 Introduction

Most of the authors who report work on films grown by PLD have used a ceramic target of ZnCoO that has been fabricated using solid-state reaction techniques. In most cases the Co has been introduced by using Co_3O_4 as the precursor [1,2]; however, CoO and metallic Co have also been used [3,4]. In this chapter, a comparison of the structural, magnetic, and magneto-optical properties of 5% Co-doped ZnO thin films grown by PLD using different targets is described. The Co-doped ZnO films were grown from three different targets that had been made with Co, CoO, or Co_3O_4 precursors. These targets each contain different quantities of oxygen, the target made from metallic Co has the minimum and Co_3O_4 target has the maximum. The films produced from these different targets were grown at several different oxygen pressures; at a base pressure of 2×10^{-5} and four additional higher oxygen pressures of 1×10^{-4}, 1×10^{-3}, 1×10^{-2}, and 1×10^{-1} Torr. This enabled us to study to what extent adding oxygen to the target is equivalent to adding oxygen in the PLD chamber. The main purpose of this work is to extend the work was done by Ying *et al* [5]. All of our sample's thicknesses were between 100 – 130 nm compared to 100-730 nm in [5]. This was to remove any thickness dependence of the magnetic properties in these films. In addition, the origin of the magnetisation was investigated for additional films made from Co metal, CoO and Co_3O_4, precursors with a wider range of oxygen pressures, in order to have a complete study of the magnetic circular dichroism (MCD). The magnetisation of powder samples taken from each of the targets was also measured. In the following, the previous work of Co-doped ZnO is described and then the current work is discussed.

6.2 Previous Works in Co-doped ZnO

One of the first theorists to motivate the study of transition metal oxides (TMO), specifically TM-doped ZnO, was Dietl *et al* [6], who suggested that Mn can utilise holes in the valence band to produce an indirect exchange mechanism in which RTFM could be observed in Mn-doped ZnO p-type systems. Sato *et al* [7] also suggested the DMS materials could exhibit RTFM in n-type ZnO. Many researchers have reported RTFM TM-doped ZnO systems experimentally [1,8-39]. However, the origin of this ferromagnetism is still controversial even though there have been many studies of ZnO doped with transition metals (TM). Co-doped ZnO materials are among the most intensively studied DMS candidates [40]. Due to the magnetisation present in metallic Co, it is difficult to separate the intrinsic magnetic properties from those arising from Co nanoparticles. In particular, for films grown in an oxygen deficient atmosphere, metallic Co is more likely present. Annealing at high temperatures increases the cobalt mobility which leads to a further increase in the amount of metallic Co [41,42].

Various conflicting theoretical predictions have also suggested that ZnCoO can be ferromagnetic in both p-type [6,43] and n-type cases, with the n-type case resulting from oxygen deficiency or aluminium dopants [44]. The relevance of magnetic polarons, based on Co^{2+} ions, has already been discussed [36], but XMCD measurements demonstrate that Co^{2+} ions can be paramagnetic even though the sample is ferromagnetic [45]. Conflicting experimental results are likely due to differing environmental and control parameters during the production stage; these include the percentage of Co-dopants, preparation techniques and growth conditions.

As it was mentioned in Chapter 3 the films can be made by PLD, reactive sputtering, annealed sol-gel and ultrasonic assisted solution chemical vapour deposition [1,11,16,21,39]. There have been studies of the effect of changing the carrier concentration on the magnetic properties, by co-doping with Al or Ga and by growing with various amounts of oxygen [9,39,46,47]. The majority of samples have been grown such that they were n-type conductors and it was reported that the magnetism disappeared as the amount of oxygen in the films was increased, thus supporting the hypothesis that oxygen vacancies, or Zn interstitials, were necessary for the observation of RTFM [2,16]. However, there have also been reports of substantial magnetism being observed when the films were grown oxygen-rich [9,11]. The studies of Co-ZnO films are still ongoing in order to investigate the origin of ferromagnetism. Here some of the previous works, reporting the observation of RTFM in Co-doped ZnO films produced with different Co doping percentages, preparation techniques, growth conditions and post annealing are discussed.

Promising results of RTFM were observed with a 5-25% Co and 1% Al-doped ZnO system with no detections of secondary phases by Ueda *et al* [48]. Further studies show that adding Al to Co-doped ZnO films, with existing Co nanoparticles, is essential to enhance not only the magnetisation but also the magneto-optical properties. This could be achieved by using larger nanoclusters which in return provide a sufficient concentration for an exchange-coupling to occur [3,9,49,50]. Ferromagnetic moments of 5 μ_B and 3 μ_B per TM ion were observed by carefully manipulating the Al dopant and oxygen deficiency in n-type ZnMnO and ZnCoO respectively by Xu *et al* [2]. Al doping produces free electrons that facilitate magnetism in ZnO.

Several groups have reported that RTFM, in Co-doped ZnO systems, is observed due only to metallic cobalt clusters [41,51-53]. This indicates that metallic Co nanoparticles might play an important role in determining ferromagnetism in DMS. For instance, 5% Co-doped

ZnO thin films were ablated at 400°C and 500°C by Opel *et al* [53]. These films were ablated by PLD using a KrF excimer laser (248 nm) at a repetition rate of 2 Hz on single crystalline ZnO substrate. SQUID magnetometry, X-ray magnetic circular dichroism (XMCD) and AC susceptibility were used to measure the magnetic properties. The ZFC/FC hysteresis loops at a temperature of 300K and a magnetic field of 100 Oe were measured and fitted by Langevin functions indicating superparamagnetic particles as predicted in Fig 6.1 [53]. Fig 6.1 (a) shows the data of the loops after the linear diamagnetic contributions of the substrate were subtracted and the inset shows the coercive field is zero for both samples. ZFC/FC magnetisation was measured for both samples resulting in different curves as predicted in Fig 6.1 (b). According to the ZFC curves, blocking temperatures of metallic Co nanoparticles occurred at 15 K and 38 K for films deposited at 400°C and 500°C, respectively [53].

Kaspar *et al* [54] observed a small RTFM in CoO-doped ZnO epitaxial thin films with high structural quality. The samples were deposited at an oxygen pressure of 10 mTorr oxygen pressure and temperature of 550°C on a *c*-plane oriented substrate using the PLD technique. X-ray absorption spectroscopy measurements revealed that Co ions were substituted for Zn in the ZnO matrix without any resultant secondary phases. The samples have been produced in a variety of growth conditions such as post-annealing in a vacuum, and/or adding Al while ablated. The magnetic properties of the films were measured using a vibration sample magnetometer (VSM). X-ray photoelectron spectroscopy (XPS) and high-resolution transmission electron microscopy (TEM) techniques study the details of the microstructure of the film, where no spin states near the conduction band were found. The electronic structure of the films remained unchanged, according to the optical MCD spectra measurements. Despite the high concentration of the magnetic dopant in high structural quality Co-doped ZnO epitaxial films, the RTFM accomplished was low which indicated that the itinerant electron in the band was not enough to produce magnetism. They suggested that some appropriate defects in the structure of the sample are essential to facilitate the coupling between Co dopants and roving electrons in the ZnO conduction band [54].

Removed
by the author
for copyright reasons

Figure 6.1: (**a**) RTFM hysteresis magnetisation loops from $Zn_{0.95}Co_{0.05}O$ thin films grown at 400°C and 500°C where (green squares) and (blue circles) respectively with the magnetic field applied parallel to the film plane. The inset demonstrates the region around zero fields. (**b**) ZFC (open symbols) and FC (closed symbols) magnetisation measurements, where the magnetic field applied $H = 100$ Oe. The two samples show super magnetic blocking temperature at T_B = 15K and 38K respectively. The inset shows the zero-field-cooled magnetisation vs $\mu_0 H/T$ for one sample for temperatures up to 375K. The data follows a Curie law (straight line) for temperatures well above T_B taken from [53].

The origin of FM in three different samples made of 5% Co-doped ZnO layers thin films was also investigated using XMCD spectroscopy and SQUID magnetometry by Tietze *et al* [45]. The target used was a mixture of ZnO and Co_2O_3 powders, and the PLD technique was used to ablate these films with an excimer laser of KrF with a wavelength of 248 nm. The resulting signal from Co, Zn, and O ions of XMCD indicated that all of the core ions were paramagnetic and that no metallic Co was present meaning that all the Co^{2+} ions moved into the substitutional sites. Therefore, the FM observed was due to defects created in the material such as oxygen vacancies, which is in agreement with Barla *et al* [55].

Other studies claim that the observed RTFM is due to defects of the materials without TM ion doping [18,56-58] as was previously discussed in chapter 4. However, some studies have indicated the necessity of both carriers and defects in the observed RTFM in TM doped ZnO [59]. One study using MCD by Neal *et al* [18], investigated the origin of magnetism in ZnO thin films containing a concentration of up to 5% Co_3O_4. A film thickness of 200 nm was used and was ablated on a *c*-cut sapphire substrate by PLD. The films were grown at an oxygen pressure of 1× 10^{-2} Torr in the PLD chamber. The optical MCD spectrum measurements at 10 K in both undoped ZnO and ZnCoO films are presented in Fig 6.2. The authors deduced that the observed FM is due to defects resulting from the electrons in the ZnO band being polarised.

Removed

by the author

for copyright reasons

Figure 6.2: MCD spectrum at 10K in a field of 0.45 T for an undoped ZnO film Vs. $Zn_{98}Co_{02}O$ films, both grow on a sapphire substrate. The arrows show the d-d transition and ZnO band edge at 2 eV and 3.4 eV respectively [18].

In another study by Ivill *et al* [1], a high concentration of up to 30% Co_3O_4-doped ZnO films grown by PLD at different growth conditions was investigated. Films made with a low percentage of Co dopant exhibited paramagnetic and ferromagnetic behaviours at RT. RTFM was achieved in films doped with 30% Co ablated in a vacuum but this was reduced with increasing oxygen pressure. Therefore, defects due to oxygen vacancies, which were created during the vacuum growth, are vital for obtaining RTFM which was also claimed by Xu *et al* [2]. The films growth parameters such as TM concentration, substrate temperature, and oxygen pressure affect both the structural and magnetic properties of TM doped in ZnO [1].

ZnCoO films were grown from Co_3O_4 targets in two separate laboratories using PLD by Heald *et al* [41]. The aim was to investigate the different growth conditions of films with excessive Zn versus films ablated at low oxygen pressures. The first set of films, which are n-type conductive, were annealed at 600°C for 5 hours in the Zn vapour environment. This created Zn interstitials and the films SQUID measurements show weak RTFM [42]. The amount of metallic Co in each sample was detected by XANES and EXAFS measurements. The results show a lack of metallic Co present in the films in comparison to the other set of Co-doped ZnO films, which were grown epitaxially on sapphire substrates at an oxygen pressure of 1×10^{-2} Torr. The result also shows that the films contain a secondary phase of metallic Co, which is responsible for only part of the observed ferromagnetism [41].

In recent work by Ying *et al* [5] 5% Co-doped ZnO thin films were grown from targets made from metallic Co, CoO, or Co_3O_4 precursors, via PLD, to investigate the effect of the precursor on the magnetism. For all samples, the deposition time was kept the same, and as a result, the films varied in thickness from 100 nm to 730 nm. The growth condition such as oxygen pressure was varied with only the films made from the metallic target. These films were produced at base pressure and two additional oxygen pressures. However, the films made of CoO and frequent Co_3O_4 targets were made only at base pressure. The interesting result was obtained for the films made of the metallic Co target, large RTFM was observed only with rich oxygen environment during ablation in the absence of the metallic Co. However, all films made at base pressure contain metallic Co that is responsible fully or partially for the magnetism. Table (6.1) shows a summary of the growth conditions of the films including the precursor of the target, the oxygen pressure while ablated in the chamber, the thickness of the films, the concentration of Co, grain sizes, Co metal, and magnetisations at 300 K and 5 K [5]. The magnetic properties were measured using a SQUID magnetometer. The energies of the spin-polarised electron were investigated by MCD spectra measurement as shown in Fig 6.3.

Table 6.1: The films parameters are shown such as the precursor of the target, the pressure in PLD chamber, the films thickness, the concentrations of Co, the c lattice and grain sizes, fraction of Co atoms as Co metal. Both the *Ms* value of the saturation magnetisation at 5 K and 300 K, and the *Ms* value of the saturation magnetisation from the Co nanoparticles contribution taken from [5].

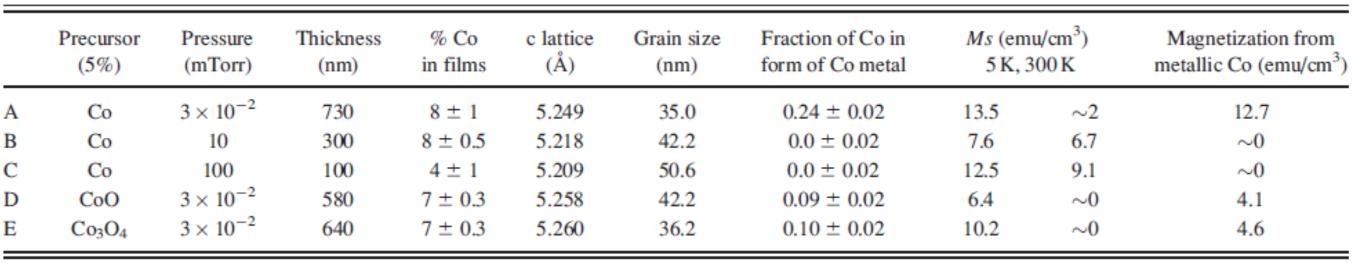

	Precursor (5%)	Pressure (mTorr)	Thickness (nm)	% Co in films	c lattice (Å)	Grain size (nm)	Fraction of Co in form of Co metal	*Ms* (emu/cm^3) 5 K, 300 K		Magnetization from metallic Co (emu/cm^3)
A	Co	3×10^{-2}	730	8 ± 1	5.249	35.0	0.24 ± 0.02	13.5	~2	12.7
B	Co	10	300	8 ± 0.5	5.218	42.2	0.0 ± 0.02	7.6	6.7	~0
C	Co	100	100	4 ± 1	5.209	50.6	0.0 ± 0.02	12.5	9.1	~0
D	CoO	3×10^{-2}	580	7 ± 0.3	5.258	42.2	0.09 ± 0.02	6.4	~0	4.1
E	Co_3O_4	3×10^{-2}	640	7 ± 0.3	5.260	36.2	0.10 ± 0.02	10.2	~0	4.6

The films grown from the metallic cobalt precursor at different oxygen pressures, exhibited magnetic hysteresis loops at 5K and 300K as shown in Fig 6.3 (a). The magnetisation measured at 300K increases with increasing oxygen pressure. All the films were grown from all the co-doped ZnO precursors at base pressure as shown in Fig 6.3 (b). The investigation energies of the spin-polarised electron states were measured by MCD spectra as shown in Fig 6.4. MCD was used to measure the spectral region up to the band gap of 3.4 eV, where the magnetically polarised defect occurs. The authors found that the films grown from a metallic cobalt target were different from all other films because these films had large RTFM in an oxygen environment.

Removed
by the author
for copyright reasons

Figure 6.3: The magnetic hysteresis loops measurements from the squid at both temperatures 5 K and 300 K (the diamagnetic contribution from the substrate and temperature dependent paramagnetic contributions from the film have been subtracted from the raw data) for **(a)** films A, B, and C, and **(b)** films A, D, and E. The figure is taken from [5].

Removed
by the author
for copyright reasons

Figure 6.4: The MCD spectra measurements for Co-doped ZnO thin films **(a)** made at base pressure with different types of targets and films that were **(b)** made from metallic Co target at different oxygen pressure**,** taken from [5].

6.3 Sample Preparation

High-purity pure ZnO powder was combined with either metallic Co, CoO, or Co_3O_4 powders to produce three different targets for PLD, with the same nominal composition of 5% Co-doped ZnO using the solid-state reaction technique which is the same method used by Ying *et al* [5]. All the powders were purchased from *Alfa Aesar* and have purities of 99.999% for ZnO, 99.998% for metallic Co 99.998% for CoO, and 99.998% for Co_3O_4. Different targets of metallic Co-doped ZnO, CoO-doped ZnO, and Co_3O_4-doped ZnO were produced by taking the precise stoichiometric amounts of the target components required and weighing them out using an electrical balance. These powders were then mixed and ground with a mortar and pestle for no less than 25 minutes. This step was essential to ensure the proper mixing of all components. Next, this powder was placed in a high-quality alumina crucible and annealed for 12 hours at 300^o C in air in a furnace. These powders were then ground in the mortar and pestle for 25 minutes and reannealed for 12 hours at a higher temperature of 600^o C. The powder mixture was again re-ground and reannealed for 12 hours at 900^o C. Repeatedly increasing the temperature, sintering and grinding were essential, not only to make the desired oxide component but also to eliminate the impurity phases of un-reacted powders.

The three different targets have different oxygen contents, where metallic Co target has the minimum and Co_3O_4 target has the most. However, the annealing targets in the air during fabrication might lessen this effect. A commercial Specac die of internal diameter 25 mm was used in conjunction with a manual, hydraulic bench-press with a capability to compress the powder to a pressure of 25 kPa. This was a necessary step to produce a cylindrical, dense pellet 25 mm in diameter and 5 mm in thickness. This target was then finally sintered at 900^o C for 13 hours in order to produce a target with a smooth surface. The procedure ensured that the targets would have high density and therefore would be ideal for ablation.

All the targets made of Co, CoO and Co_3O_4 appeared to have the same green colour despite the different amount of oxygen in each target. This indicates that similar amounts of the Co^{2+} had been incorporated into the ZnO lattice during the solid-state reaction to form the compound $Zn_{1-x}Co_xO$, which is known as cobalt green.

For future reference, ZnO powder combined with powders of metallic Co, CoO, and Co_3O_4 targets are referred to T_1, T_2, and T_3 respectively. These targets were used to produce Co-doped ZnO films by PLD. These films were grown at a range of oxygen pressures. Many films were produced, each with different deposition times in the beginning in order to obtain the desired thickness of ~120 nm. This is associated with five different pressures; a base pressure of 2×10^{-5} Torr and four higher oxygen pressures of 1×10^{-4}, 1×10^{-3}, 1×10^{-2}, and 1×10^{-1} Torr as a result five films were made of each precursor. All the films were deposited on a sapphire substrate with a temperature of 450°C. The sapphire substrate was purchased from PI-KEM Ltd and was double-sided polished, single-crystal *c*-cut Al_2O_3 as was discussed in Section 3.6.

6.4 Experimental Results and Discussion

This section will focus on the discussion of the structural, magnetic, and magneto-optical properties of films made from T_1, T_2, and T_3 at different oxygen pressures. XRD, XANES, and EXAFS measurements were used to investigate the structural characteristics of all films. Finally, SQUID and MCD measurements were used to investigate the magnetic and magneto-optics properties respectively for all the films made produced from T_1, T_2, and T_3.

The XRD measurements were carried out in The Department of Materials Science and Engineering at The University of Sheffield. The XANES and EXAFS measurements were taken by Steve Heald at the Advanced Photon Source in the Argonne National Laboratory, USA. All the SQUID and MCD measurements for all the films were carried out at the Department of Physics and Astronomy at the University of Sheffield. Some of the magnetic properties and the annealing process of the only targets T_1, T_2, and T_3 (not the films) were performed by our collaborator Dr Marzook Alshammari at King Abdulaziz City for Science and Technology, KACST.

6.4.1 Structural Properties

Structural properties were analysed for all the films made of T_1, T_2, and T_3 targets at a range of oxygen pressures. The structure of the crystal lattice, the *c* lattice constant, and the grain sizes were obtained from the XRD measurement**.**

All the X-ray measurements were taken using the apparatus described in Section 3.3.1 using CuK_α radiation (λ=1.5406 Å). An XRD plot of typical films made from T_3 at different oxygen pressures is shown in Fig 6.5. All the films exhibit a single phase with a typical wurtzite ZnO structure, showing a *c*-axis out of plane orientation with only (002) and (004) ZnO diffraction peaks as expected [13,60]. The (006) diffraction peak is from the sapphire substrate. No secondary or defect phases were detected within the detection limit of $\leq$ 10% of the XRD of any of the films. In this study, the XRD is not used to detect the secondary phases, however, the extended x-ray absorption fine structure (EXAFS) is much better technique, which is used to detect the secondary phases in the films.

The *c* lattice constants measured from XRD of the films made of T_1, T_2, and T_3 at a different range of oxygen pressures is shown in Fig 6.6 (a). The result shows that the *c* lattice constant of the films made from T_1 is larger than the accepted ranges of bulk ZnO, which is found to be in the range between 5.2042 and 5.2075Å [60], whereas the *c* lattice constant for the films made from T_2 and T_3 is smaller than the lattice constant for pure bulk ZnO. This decrease of the *c* lattice parameters is consistent with the substitution of Co^{2+} for Zn^{2+} ions as the ionic radius of Co^{2+} is 0.58 Å which is slightly smaller comparing to 0.60 Å for the ionic radius of Zn^{2+} [2,61].

The lattice constant is expected to contract as the concentration of vacancies rises and, conversely, to expand with increasing numbers of interstitials [16]. Hence, the value of 2θ shifted towards smaller angles as the oxygen pressure increased as shown in the inset of Fig 6.5. This implies that the *c* lattice constant increases as oxygen is added to the PLD chamber for the films made from T_2 and T_3 targets. This is consistent with the film having a large amount of oxygen vacancies when grown at low oxygen pressure and that these vacancies are removed at higher oxygen pressure causing the lattice to expand [2,62]. The results for the lattice constant imply that the extra oxygen that is present, due to using Co_3O_4 in the target, compared with CoO is very roughly equivalent to increasing the oxygen pressure in the PLD chamber by a factor of 10. The same equivalence of additional oxygen in the target to that in the chamber was seen for films of $(InFe)_2O_3$ [63]. However, very different behaviour is observed for the film made from T_1 as the *c* lattice constant decreased when the oxygen pressure was increased as is shown in Fig 6.5 (b) and 6.6 (a). This effect was observed previously and was attributed to an increasing concentration of Zn vacancies with increasing oxygen in the PLD chamber [5,16].

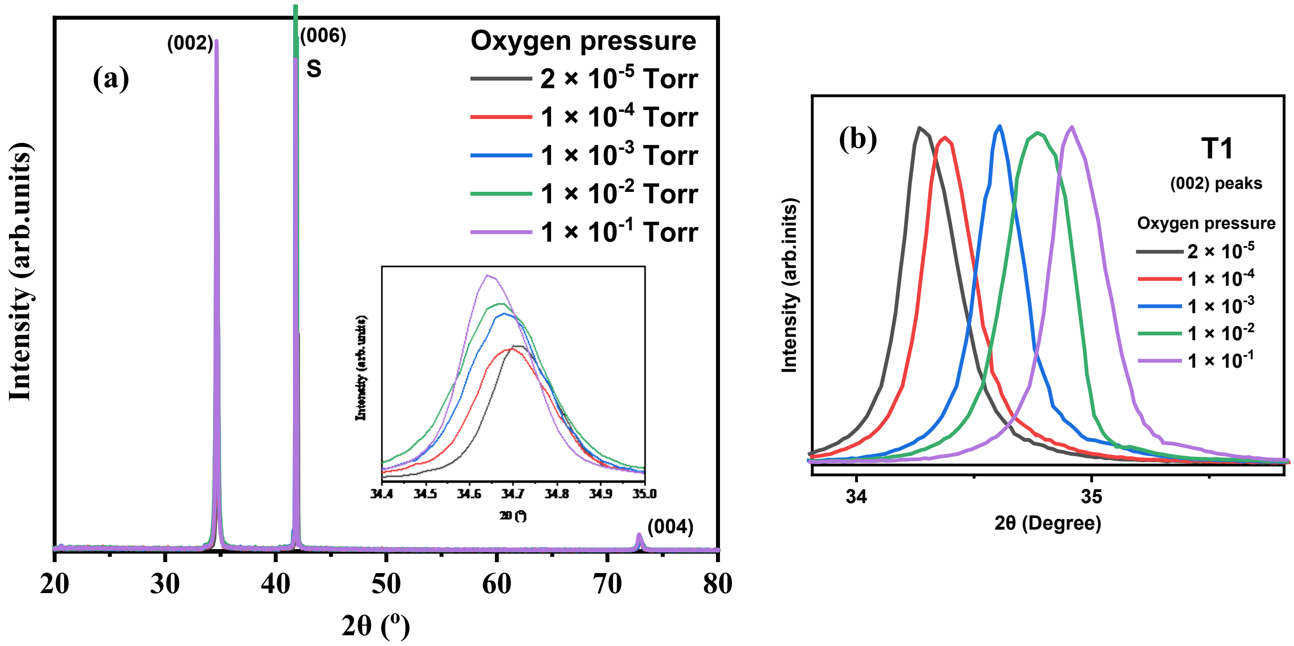

Figure 6.5: XRD data of the films made from Co_3O_4 target at a base pressure of 2× 10^{-5}Torr, and four different oxygen pressures of 1× 10^{-4}, 1 × 10^{-3}, 1 × 10^{-2}, and 1 × 10^{-1} Torr. The inset demonstrates the shifting of the (002) peak towards smaller 2θ with increasing oxygen content in the chamber. S stands for the sapphire peak (006). (b) the (002) peaks for the films made of Co target shown the peaks has shifted towered higher 2θ with increasing the oxygen content in the chamber.

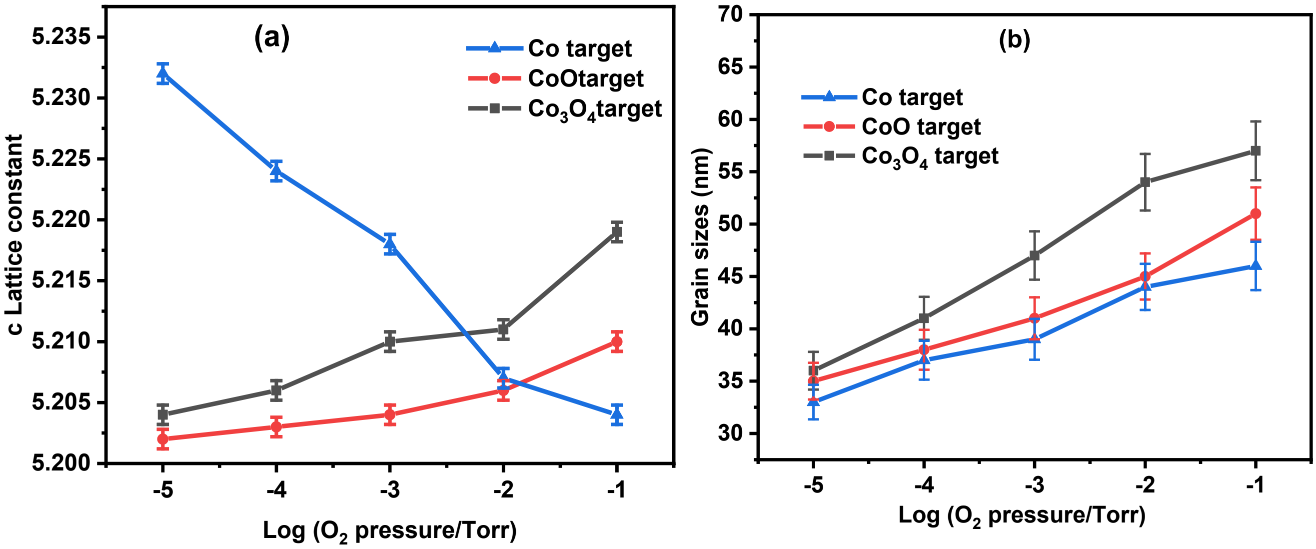

Figure 6.6: (**a**) The *c* lattice constant for the films made from Co, CoO, and Co_3O_4 targets at a different range of oxygen pressures. (**b**) The grain sizes for the films made from T_1, T_2, and T_3 at a different range of oxygen pressures.

The enlarged ZnO (002) diffraction peaks are shown in Fig 6.5, which used the FWHM and Debye-Scherrer equation to make an estimate of the grain sizes, as explained in Section 3.3.1. Fig 6.6 (b) shows the grain sizes the films made of T_1, T_2, and T_3 at a different range of oxygen pressures. The ranges of the grain sizes were found to be between 33 nm and 57 nm, which are in the acceptable range where magnetism might occur as predicted from this mechanism [64]. The grain sizes increased with the amount of oxygen pressures in the chamber for all the films, as shown in 6.6 (b). The largest grains were obtained for the films ablated/made from the Co_3O_4 target.

XANES spectra were performed to determine the ionisation (chemical) state of the Co ions in all films grown from T_1, T_2, and T_3. In such a measurement, the amount of metallic Cobalt in films can be estimated, and the presence of any oxide precursors can be detected. Therefore, it can detect any potential existence of metallic Co and any secondary oxide phases. All these measurements were performed at the Advanced Photon Source in the Argonne National Laboratory in the USA by our collaborator Steve Heald.

Fig 6.7 (a) shows a comparison of XANES data of the films grown from T_1, T_2, and T_3 which were deposited at a base pressure of 2×10^{-5} Torr, and the standard valence states of pure metallic Co and a sample of ZnCoO which is known to be fully Co substitutional in the Zn^{2+} sites; which is used as reference. The near edge region ~ 7712 eV, which is indicated by the arrow, is the most sensitive to the metal [41]. The increased signal in the area means that the films contain some metallic contributions. The quantity of metallic Co was analysed and estimated using the Athena and Artemis interfaces program package [41,65] by Steve Heald. The percentage of metallic Co contribution is approximately ~ 28, 16, and 14% for Co-doped ZnO thin films grown at base pressure from T_1, T_2, and T_3 respectively, as shown in Table 6.2. On the other hand, Fig 6.7 (b) shows a comparison between the standard valence states of pure metallic Co, CoO, Co_3O_4, and ZnCoO sample which has the Co substituted in the Zn^{2+} sites and the films that were grown from T_1, T_2, and T_3. All the films were deposited at an oxygen pressure of 1×10^{-3} Torr as typical which are applied for all the films that were grown in an oxygen pressure of 10^{-4} Torr or any higher pressure. The comparison shows no metallic cobalt or secondary phases were detected, indicating all the Co ions were substitutional. The films made from T_1 have the most metallic cobalt when grown at base pressure, which is not surprising. It was significant that none of the films produced at higher oxygen pressures showed any evidence for the presence of cobalt oxides CoO or Co_3O_4. The variation of the lattice constant with pressure is the most revealing of the structural measurements as it shows that the films grown from a target formed from metallic Co cobalt are significantly different from those grown from a CoO or Co_3O_4 target.

The EXAFS measurement was used to investigate the structural environment around the Co ions to find out if either of the oxide precursors, CoO or Co_3O_4 is present in the films. Fig 6.8 shows typical films grown from T_1, T_2, and T_3 at a base pressure of 2×10^{-5} Torr with the peaks of Co_3O_4 and CoO, and metallic Co. The spectra of peaks shown in Fig 6.8 demonstrates that any residual concentration of CoO or Co_3O_4 is below the detection limit.

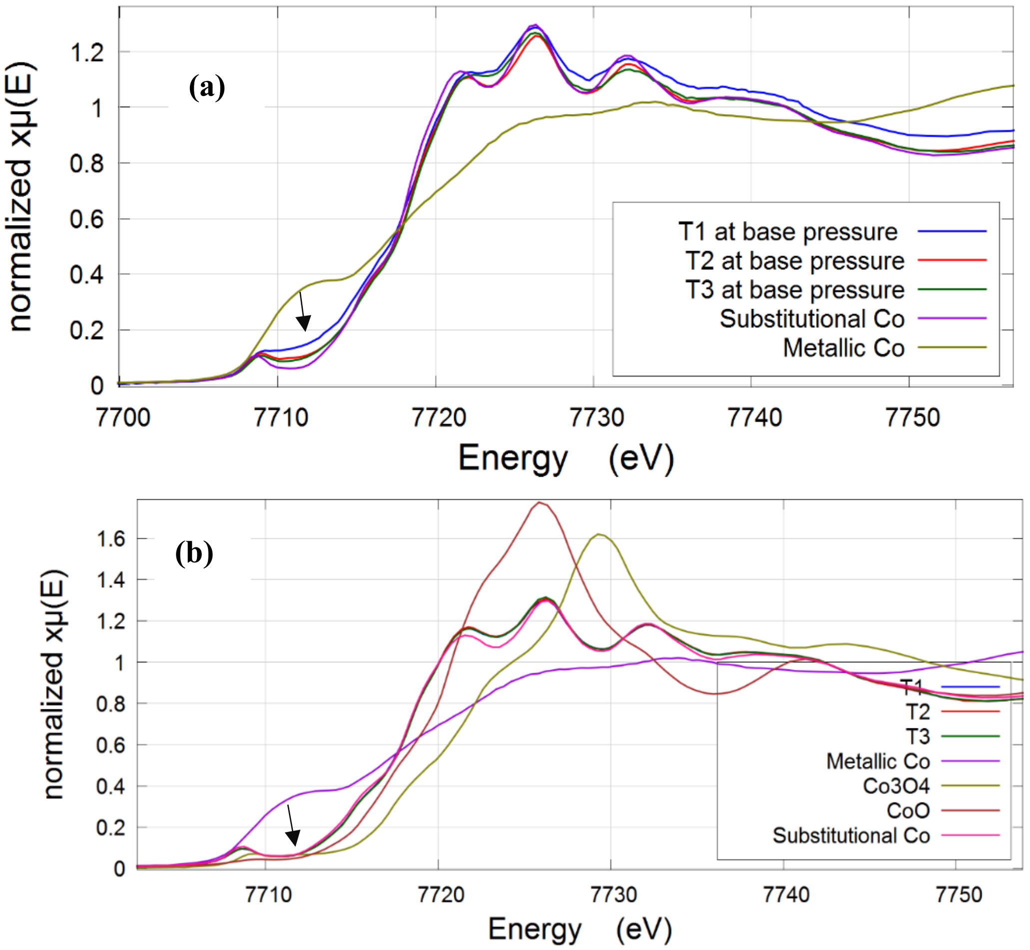

Figure 6.7: XANES data of pure metallic Co, CoO, and Co_3O_4 which were used as reference to compare with the films grown from T_1, T_2, and T_3 at (**a**) a base pressure of 2×10^{-5} Torr; and (**b**) at an oxygen pressure of 1×10^{-3} Torr. Measurements were taken by Steve Heald.

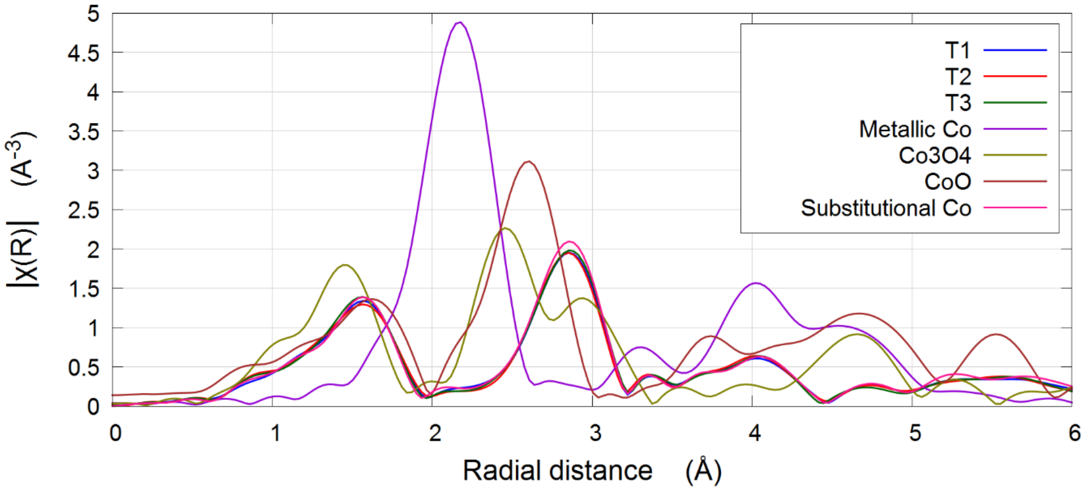

Figure 6.8: The Fourier transform of the EXAFS of the films from T_1, T_2, and T_3 targets taken at base pressure of 2×10^{-5} Torr and the reference signal (these all superpose) compared with the signals from metallic cobalt, bulk CoO and Co_3O_4 which are quite distinct. Measurements were taken by Steve Heald.

6.4.2 Magnetic Properties

The magnetic properties have been studied for both films and targets. This is to learn how the magnetisation of the films made of these different targets T_1, T_2, and T_3 at a different range of oxygen pressures varies. The study of the magnetic properties was investigated by using the SQUID magnetometer, which can measure the magnetisation at 5K, and 300K with a field of up to 1 T. This was already discussed earlier in detail in the experimental see Subsection 3.5.1

Measurements were made of the magnetisation as a function of temperature in field cooled (FC) and zero field cooled (ZFC) conditions. The magnetic hysteresis loop measurements were taken at 5 K and 300 K for all films made from T_1, T_2, and T_3 that had been deposited at different pressures. To remind the reader that is at a base pressure of 2×10^{-5} Torr and four higher oxygen pressures of 1×10^{-4}, 1×10^{-3}, 1×10^{-2}, and 1×10^{-1} Torr. The linear diamagnetic contribution from the sapphire substrate and the paramagnetic contribution have been subtracted from all measurements shown in the subsequent figures.

The magnetisation of a small amount of the powder was taken from each of the targets and measured. Since the films were deposited at high oxygen pressure in the PLD chamber, the magnetism of these samples was also measured after these powders had been annealed in air for 6 hours at 600 °C. This allowed us to investigate the effects of the annealing on the magnetisation of the targets and to compare this with the properties of the films.

6.4.2.1 Measurements of Field Cooled and Zero Field Cooled Magnetisation (FC/ZFC)

FC- ZFC measurements were carried out to investigate if there is a superparamagnetic blocking temperature. The size of any cobalt nanoparticles can be estimated. FC and ZFC magnetisation data, which is temperature-dependent, has been obtained for all the targets and the films grown from T_1, T_2, and T_3 deposited at a base pressure of 2×10^{-5} Torr. This measurement was made in a magnetic field of 100 Oe and was performed for T_1, T_2, and T_3 targets both as used for the deposition and after annealing in air; the results are shown in Fig 6.9 (a) and (b). The only target to show hysteretic behaviour was the one made with Co_3O_4, this may be because of nanoparticles of CoO and Co_3O_4 which have been found to show weak ferromagnetism at room temperature [66]. The lowest susceptibility was found with films prepared from the Co target and this showed no evidence of Co nanoparticles. Powder from the targets, which was annealed in air at 600° C, was studied in order to investigate if similar behaviour occurred for the targets as was seen for films ablated in an oxygen atmosphere. However, relatively little difference was seen after the annealing as shown in figure 6.9 (a), (b).

There is a clear separation between FC and ZFC peaks around 55 K for the film that was made with T_1 at a base pressure of 2×10^{-5} Torr, as illustrated in Fig 6.9 (c), which is also close to where the irreversibility sets in. The result is in good agreement with the SQUID measurement at 5 K in which the sample has a large coercive field (*Hc*) as it is shown in Fig 6.12 (b) and Table 6.2. This is a standard plot for a film containing cobalt nanoparticles that are superparamagnetic above 55 K and become blocked below this temperature [51,53,67]. This was confirmed by the XANES data, which concludes a percentage of the fraction of metallic Co was present in the film grown from T_1 deposited at a base pressure of 2×10^{-5} Torr. The Co nanoparticle size can be estimated using the Bean–Livingston equation, $KV \sim 25k_BT_B$, where V is the average volume of the particles, K is the magnetic anisotropy constant, T_B is the blocking temperature, and k_B is Boltzmann's constant [44]. K is ~ 2.7×10^5 J/m^3 for bulk Co metal [50], and the average size of the Co nanoparticles gives d ~ 5.1 nm. In comparison, Ying *et al* [5] did not find large nanoparticles for the films made under similar conditions however their film was much thicker, 730 nm, compared with 120 nm for the films studied here.

Above 55 K the magnetisation shown in Fig 6.9 (c) can be fitted to a Curie Weiss law, M = χH = $\frac{CH}{T+\theta}$ as shown in Fig 6.16 (a) where H = 100 Oe, C = 8.4 emu cm^{-3} Oe^{-1} deg^{-1}, and θ = 229K, indicating antiferromagnetic coupling between the nanoparticles. A better fit can also be achieved by fitting to a modified Curie-Weiss law, M = χ_0H + $\frac{CH}{T+\theta}$, as shown in Fig 6.16 (b), where χ_0 is independent on either the field or the temperature. The fitting parameters are C = 4.4 emu cm^{-3} Oe^{-1} deg^{-1}, θ = 128K, and χ_0= 0.006. However, the poor fit, actually in both cases, means that no great credibility can be accorded to the fitting parameters.

For the two different C parameters, the calculated P_{eff} values are ~ 7.4 and 5.3 respectively. These are bigger values than ~ 3.4 found previously for the films made from T1, T2, and T3.

The difference in the calculated Neel temperatures results from a temperature independent contribution to the observed magnetisation. The Neel temperature obtained from the second fitting is more comparable with that found in the literature [3] in which a Neel temperature of 66K is given for Co-doped ZnO thin films, where the thin films made of powder of ZnO, Co_2O_3 and Al_2O_3 by PLD. The percentage of metallic Co in this sample was 20%.

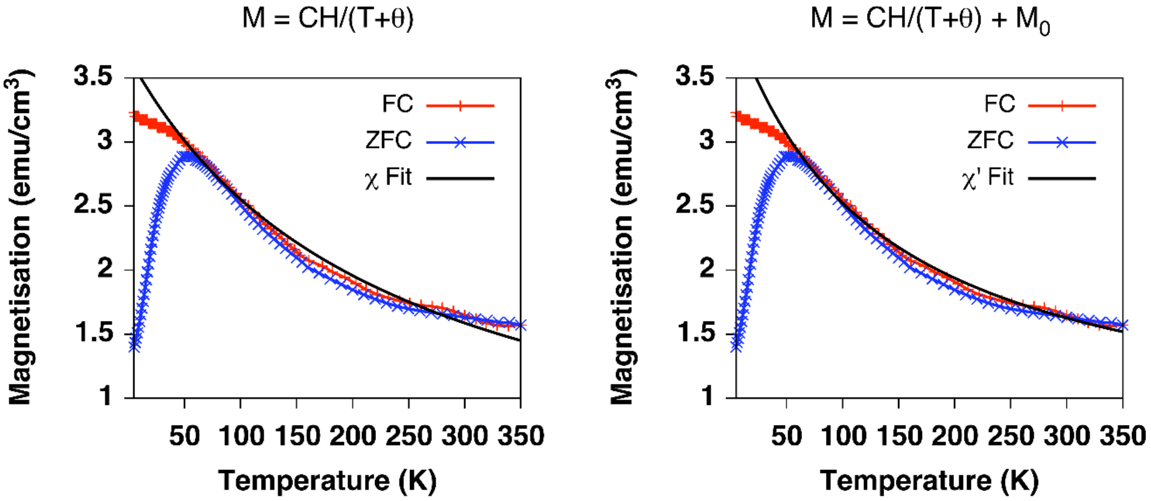

Figure 6.16 (a) The Curie Weiss law fitted line for ZFC above 55K, and **(b)** the modified Curie Weiss law fitted line for ZFC above 55 K.

The FC/ZFC curve magnetisations for the films grown from T_2 and T_3 are much smaller than those for the film grown from the T_1 target and show hysteresis behaviour at low temperatures, as illustrated in Fig 6.9 (d). However, the XANES data confirmed that the films made using targets made from T_2 and T_3 contained some metallic cobalt. The films made of T_2 and T_3 show no sign of blocking, unlike the film made of T_1, which is as expected at low temperatures for samples containing nanoparticles. No such peak is observed which implies that the Co metal nanoparticles cannot be observed if because $T_{\text{blocking}} \leq 10$ K.

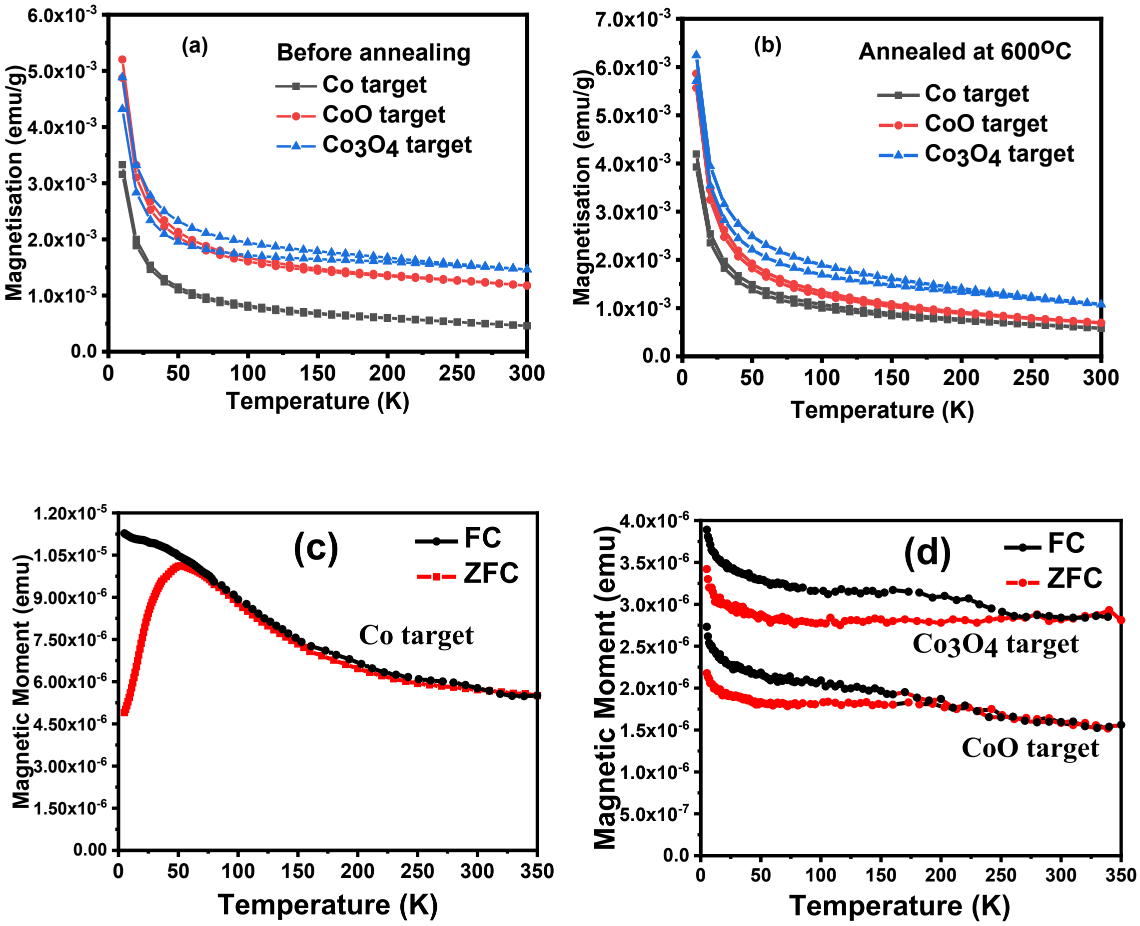

Figure 6.9: FC and ZFC magnetisation plots in an applied field of 100 Oe of the targets (**a**) as grown and (**b**) after a further anneal and of the films grown at base pressure of 2×10^{-5} Torr for (**c**) the film grown from the Co target (T_1) (**d**) films grown from the CoO (T_2) and Co_3O_4 (T_3) targets.

6.4.2.2 Hysteresis Loops from Films and Targets

The magnetic properties of a small quantity of the targets were measured and it was found that they were paramagnetic. The result did not show any evidence of ordered magnetism down to 10 K and the susceptibility increased slightly after annealing as shown in Fig 6.10. A comparison of the susceptibilities measured at 10 K and 300 K indicated that the data could be fitted to a Curie-Weiss law, $\chi = \frac{C}{T+\theta}$.

The value θ was calculated after fitting the magnetisation data as a function of the magnetic field, which is shown in Fig 6.10 (a). All the measured magnetisation of targets show that the magnetisation is linear with the magnetic field. Hence, we have M = χH, we can calculate θ as the susceptibility at temperature T is $\chi(T) = \chi = \frac{C}{T+\theta}$ and we have measured the magnetisation at both tempertures 10K and 300K, then we can have the ratio as following: $r = \frac{\chi(10)}{\chi(300)} = \frac{300+\theta}{10+\theta}$ and then $10r + r\theta = 300 + \theta$, which gives

$$\theta = \frac{300-10r}{r-1} \qquad (6.1)$$

The fitted lines are shown in Fig 6.10 (b) so that we have the susceptibility. The value of θ was calculated using the method above to be ~ 11±2 K for all the targets indicating antiferromagnetic interactions.

.

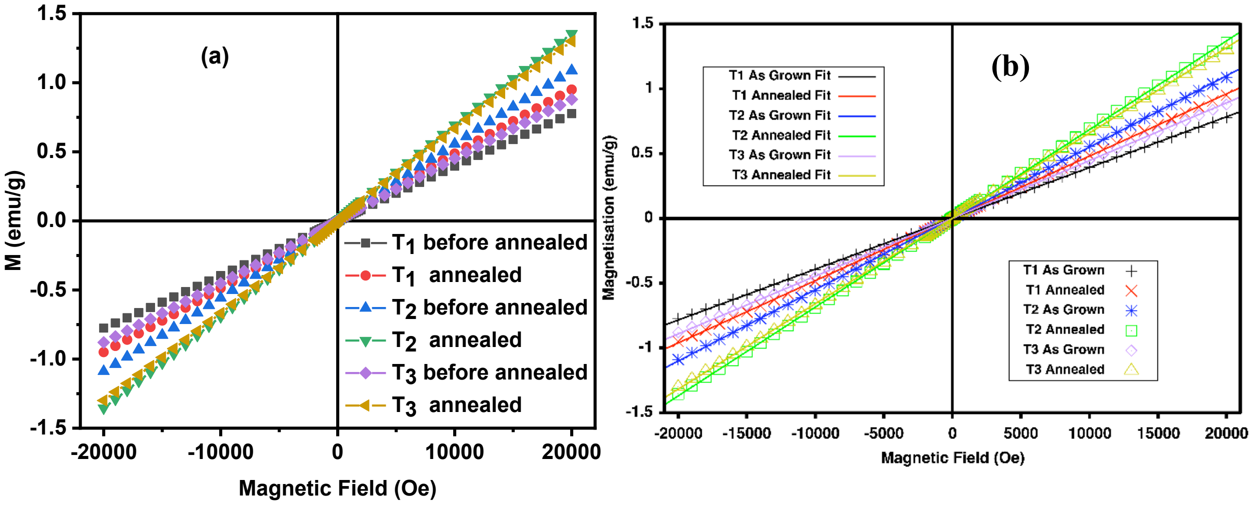

Figure 6.10: (a) The magnetic measurements at 10 K for T_1, T_2, and T_3 before and after annealing at 600° C in air for one hour. (**b**) The linear data fitted to the Curie law to get the susceptibility.

The value of the effective magnetic moment, P_{eff}, was found for all the targets from the Curie constants. The values were small and increased slightly after annealing as indicated in Table 6.3 and there was little difference between the results from different targets. The values of P_{eff}, all increased when the powders from the targets were annealed in air which contrasts strongly with the magnetism observed for different values of films ablated at oxygen pressures shown in Fig 6.13 (b).

Table 6.3: The P_{eff} for all the targets before and after annealing at 600 °C for 1 hour

Samples	P_{eff}		
	Co target	**CoO** target	**Co_3O_4** target
Before annealed	0.8	1.1	0.9
Annealed at 600°C	1	1.4	1.3

Magnetic hysteresis loops measurements at 5 K and 300 K were taken for the films that were deposited at base pressure 2×10^{-5} Torr and the four higher oxygen pressures 1×10^{-4}, 1×10^{-3}, 1×10^{-2}, and 1×10^{-1} Torr. The magnetic data for the films

Fig 6.11 (a) shows the raw data for all the films grown at base pressure of 2×10^{-5} Torr at 5 K, whereas Fig 6.11 (b) shows the raw data for the films grown from T_1, T_2, and T_3, after subtraction of the contribution from the sapphire substrate, and was separated into paramagnetic and ferromagnetic components. This can be represented into two parts: $M = M_1 + M_2$. The first part varies linearly with the magnetic field in the region $0.5 < H < 1$ T, whereas the second part M_2, is the nonlinear component which is the hysteresis loop as shown in Fig 6.12.

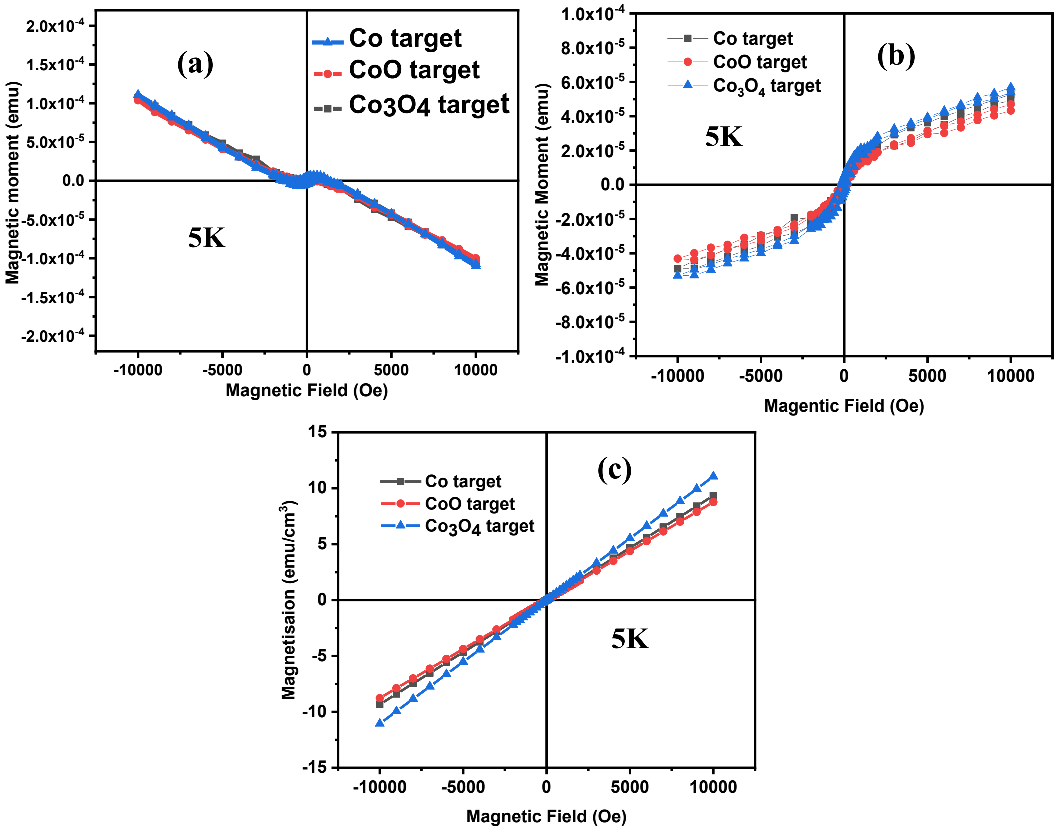

Figures 6.11 The films are grown from T_1, T_2, and T_3 at a base pressure of 2×10^{-5} Torr at 5 K **(a)** the raw magnetisation as a function of the field (**b**) the paramagnetic and ferromagnetic components M_1 and M_2 respectively (**c**) the paramagnetic component M_1.

The slope of the linear part M_l was shown in Fig 6.11 (C), was used to work out the paramagnetic susceptibility (χ), and was in the range $(9 \pm 2)\times 10^{-4}$. Hence, the Curie constant C can be determined. The susceptibility of the paramagnetic sample at 300 K is neglected as it would be too small to detect. Nevertheless, the paramagnetic contribution would still appear at 5 K. Accordingly the Curie law is used to approximately calculate the paramagnetic contribution of the sample at 5 K as shown below:

$$\chi\,(5\text{ K}) - \chi\,(300\text{ K}) = \frac{C}{5} - \frac{C}{300} \approx \frac{C}{5} \tag{6.2}$$

Hence C is the Curie constant which can be determined from the raw data of Co-doped ZnO films as measured by the SQUID at 5 K. The expected magnetic susceptibility from Co ions can be calculated by the equation below:

$$\chi \approx \frac{N x P_{eff}^2 \mu_B^2}{3 k_B T} \tag{6.3}$$

Where N is the number of ZnO ions per unit volume, P_{eff} is the effective number of Bohr magnetons, μ_B is the Bohr magneton, x is the concentration of Co dopant, and k_B is Boltzmann's constant. The theoretical value when $\boldsymbol{L}$ is quenched for Co^{2+} is $P_{eff} = 3.87$ [68]. The experimental P_{eff} values of Co^{2+} ions that are obtained from the previous equation can be compared to the theoretical value. The experimental P_{eff} values of the Co^{2+} ions for the films made from T_1, T_2, and T_3 were calculated to be 3.4±0.3. The result concludes that the orbital moment is fully quenched. The Co^{2+} ions are therefore paramagnetic and do not contribute to the ferromagnetism which is in agreement with Tieze *et al* [45,69], who showed that the $Co^{2+}$are paramagnetic even in samples that are overall ferromagnetic. This can be compared to the value of P_{eff} for all targets that was found to be 1.1±0.3, which is smaller than the value obtained for the films due to antiferromagnetic interactions.

Fig 6.12 (a) shows the magnetic hysteresis loops of films made from T_1 which have been deposited at a base pressure of 2×10^{-5} Torr and a further four different oxygen pressures of 1×10^{-4}, 1×10^{-3}, 1×10^{-2}, and 1×10^{-1} Torr at 300 K. Fig 6.12 (b) shows the magnetic hysteresis loop measurements for films grown from T_1 at base pressure 2×10^{-5} Torr at 300K and 5 K. It can be seen for the films made of T_1 that, when the oxygen pressure is increased from base pressure up to 1×10^{-1} Torr in the chamber during the film deposition, the value of saturation magnetisation of the films is also increased. Fig 6.13 shows the saturation magnetisation as a function of O_2 pressure for all films grown from T_1 at a base pressure of 2×10^{-5} Torr at (a) 5 K and (b) 300 K.

For the films made of T_1, the largest magnetisation at room temperature can be correlated with the highest oxygen pressure as shown in Fig 6.13 (a) at 5 K and Fig 6.13 (b) at 300 K respectively. The average coercivity of 170 Oe, as shown in Table 6.2, was observed at room temperature which is similar to that reported for other DMOs [67,70]. The only exception is that the film made at base pressure has the largest *Hc* at 5 K since the film has Co nanoparticles which were detected by XANES. The formation of Co metallic clusters might contribute to the observed high *Ms* value at 5 K for all the films made at base pressure [3,5,50,67]. The origin of the ferromagnetism of the sample is investigated; the source could either originate from the Co nanoparticles, defects, or grain boundaries. Therefore, it is essential to differentiate the magnetisation caused by the Co nanoparticles when it has been detected in the sample. The following method is used to convert the percentage of the metallic Co, which was detected by XANES, to the total observed magnetisation in the sample in emu/cm^3.

The detected magnetisation arising from Co can be calculated using the percentage of metallic Co detected in the sample, which was estimated by XANES to be 28, 16, and 14%, for the films grown at base pressure from T_1, T_2, and T_3 respectively. The percentage fraction

f of metallic Co and the percentage x of Co that were combined in the target is known. In our samples, the percentage of Co-doped ZnO is 5% and f is the percentage fraction of that which is metallic. The molecular mass of ZnO is 81.4 and the density is 5.61g/cm^3 as mentioned previously in Section 2.7 and the number of Zn (f.u.) per cm^3 is $\frac{N_A \times 5.61}{81.4} = 0.415 \times 10^{23}$, Where N_A is Avogadro's number. The contribution of the metallic Co is estimated by assuming each of these Co carries 1.74 μ_B then the magnetisation emu per cm^3 is

$$4.15 f x \times 1.74 \times 9.27 \times 10^{-21} \times 10^{18} = f x \times 66.94 \times 10^{-3} \text{ emu/cm}^3 \qquad (6.4)$$

Therefore, the equation below was used to calculate the magnetisation from the cobalt metal:

$$\text{Magnetisation from cobalt metal} = (6.69\, f\, x\,) / 10^2 \qquad (6.5)$$

Thus, the magnetisation due from metallic Co was estimated to be 9.4. 5.3, and 4.6 emu/cm^3, for the films grown from T_1, T_2, and T_3 at base pressure respectively, as shown in Table 6.2**.** The observed magnetisation of the metallic Co contribution is less than the total magnetisation, but it believed that this contribution plays an important role in enhancing the magnetisation of the films [3]. The values of the saturation magnetisation Ms and the coercive field Hc are summarised in Table 6.2.

The observed RTFM from the films made of T_1 increases when the oxygen pressure increases to 1×10^{-1} Torr; the value of Ms obtained here was higher than the result observed by Ying *et al* [5]. When oxygen is added and increased in the chamber, the magnetisation also increased, which meant that defects were produced explaining the observed magnetism. The possible way is by producing Zn vacancies. This is confirmed using the XRD data, which shows the c lattice constant for these films decreases with increasing oxygen pressure [5,16].

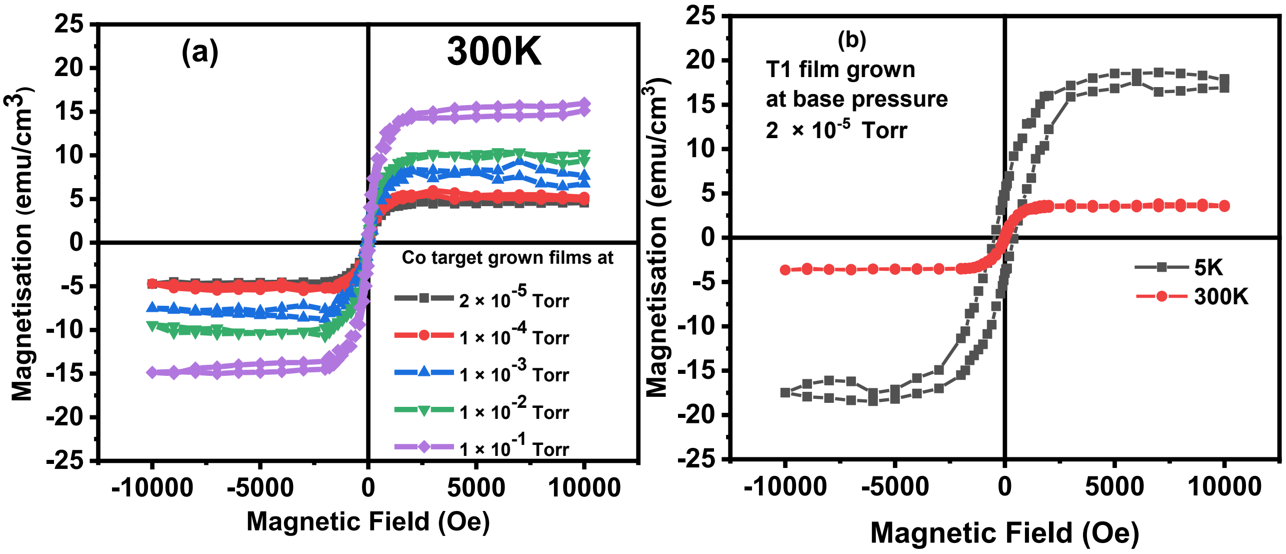

Figure 6.12: (**a**) The magnetic hysteresis loop measurements were taken at 300 K as grown from T_1 at different oxygen pressures of 2×10^{-5}, 1×10^{-4}, 1×10^{-3}, 1×10^{-2}, and 1×10^{-1} Torr. The diamagnetic term has been subtracted. (**b**) The magnetic hysteresis loop measurements at 300 K and 5 K grown from T_1 at a base pressure of 2×10^{-5} Torr.

For the film made at base pressure, the magnetisation is dependent on temperature since there is a higher magnetisation at 5 K with high H_c~500 Oe as cobalt nanoparticles are blocked [3,67,71]. For the rest of the films that were deposited at higher oxygen pressures, the magnetisation is increased with increasing oxygen pressures. In comparison, it can be seen that the *Ms* values for the films grown from T_2 and T_3 decrease when the oxygen pressure increases as shown in Fig 6.13 (a) and summarised in Table 6.2. This result has been seen experimentally and is attributed to the dramatic change caused by reducing the oxygen vacancies at high oxygen pressures [31,33,34]. This is confirmed with the XRD data that showed the *c* lattice constant for these films increased with increasing oxygen pressures. This indicates that the oxygen vacancies decrease and therefore the magnetisation decreases as the oxygen pressure is increased [2,62].

The saturation magnetisation of the samples deposited at base pressure was strongly dependent on temperature because of the existence of small nanoparticles that contributed to the magnetisation at 5 K but not at 300 K. The saturation magnetism for the films grown in oxygen showed little temperature dependence, $M(300K)/M(5K) \geq 0.8$, for all the samples except those grown at base pressure indicating that donor band states rather than local moments may be involved.

A comparison between the magnetic data for the films grown from the T_2 and T_3 targets show that the oxygen in the PLD chamber is adding to that in the target. The grain size increased with oxygen pressure as indicated in Fig 6.6 (b), so the reduction in the magnetisation of the samples made with an oxide precursor could be due to the reduction in the volume of the sample in grain boundaries, as well as the reduction of the density of oxygen vacancies. The magnetism of the sample grown with Co as the precursor was dramatically different from the others indicating a different origin. For further information about the origin of the observed magnetisation, the MCD spectra were measured for these films in the subsequent section.

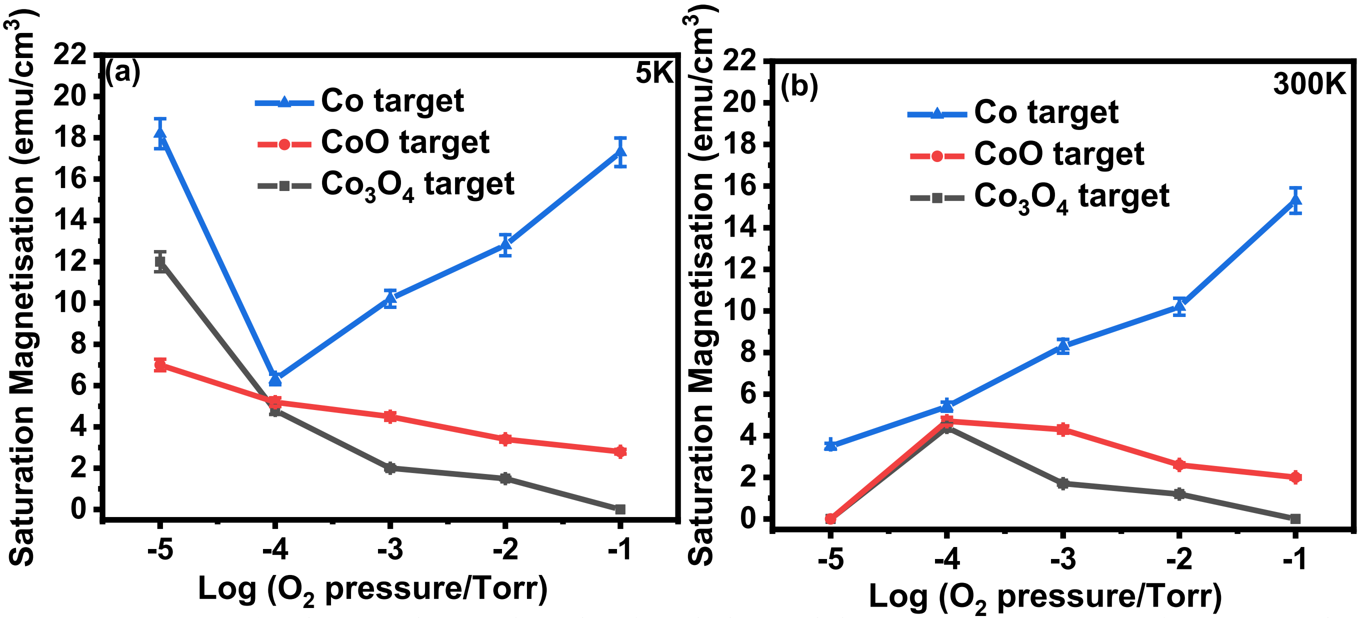

Figure 6.13: (**a**) The magnetic saturation values from the hysteresis loop measurements as grown from T_1, T_2, and T_3 at different oxygen pressures of 2×10^{-5}, 1×10^{-4}, 1×10^{-3}, 1×10^{-2}, and 1×10^{-1} Torr at 5 K (**b**) at 300 K.

6.4.3 Magnetic-Optical Properties

The Magnetic Circular Dichroism spectra (MCD) measurements were carried out for all samples grown from T_1, T_2, and T_3 in the energy range between 1.5 and 3.5 eV with an applied magnetic field of 1.8 T at RT. The MCD technique is discussed in Section 3.7 and can provide additional information about the exchange interaction between the Co nanoparticles and oxide magnetism, previously investigated by Score *et al* [72].

Table 6.2: A summary of the precursor, the pressure in PLD chamber during film deposition, the film thickness, the saturation magnetisation *Ms*, the coercive field *Hc,* and the fraction of Co atoms present as Co metal.

Precursor (5%) (Target)	**Oxygen pressure (Torr)**	**Thickness (nm)**	***Ms* (emu/cm^3)**		***Hc* (Oe)**		**The fraction of Co in metallic Co**	***Ms* due to metallic Co (emu/cm^3)**
			300K	**5K**	**300K**	**5K**		
Co (T_1)	2×10^{-5}	120	3.5±0.1	18.2±0.7	50±3.5	500±35	0.28±0.02	~9.4
	1×10^{-4}	120	5.4±0.3	6.3±0.3	132±9	150±11	0±0.02	~0
	1×10^{-3}	130	8.3±0.4	10.2±0.4	143±10	165±12	0±0.02	~0
	1×10^{-2}	130	10.2±0.5	12.8±0.5	150±11	173±12	0±0.02	~0
	1×10^{-1}	125	15.3±0.6	17.3±0.7	162±12	190±14	0±0.02	~0
CoO (T_2)	2×10^{-5}	100	~0	7±0.3	0±	440±31	0.16±0.02	~5.3
	1×10^{-4}	120	4.7±0.4	5.2±0.2	100±7	160±11	0±0.02	~0
	1×10^{-3}	130	4.3±0.4	4.5±0.2	95±7	110±8	0±0.02	~0
	1×10^{-2}	130	2.6±0.5	3.4±0.1	87±6	105±7	0±0.02	~0
	1×10^{-1}	100	2±0.5	2.8±0.1	50±3	100±7	0±0.02	~0
Co_3O_4 (T_3)	2×10^{-5}	120	~0	12.1±0.5	0	420±30	0.14±0.02	~4.3
	1×10^{-4}	130	4.4±0.4	4.8±0.2	72±5	150±11	0±0.02	~0
	1×10^{-3}	125	1.7±0.7	2±0.6	51±3	120±8	0±0.02	~0
	1×10^{-2}	130	1.2±0.9	1.5±0. 4	40±3	100±7	0±0.02	~0
	1×10^{-1}	125	~0	~0	~0	~0	0±0.02	~0

Fig 6.14 shows the MCD of the films grown at base pressure and made of T_1, T_2, and T_3 showing the negative broad signal of the metallic Co. All the MCD signals of films consist of the expected dispersive signal between 1.9eV and 2.1eV which is characteristic of the d to d* transition for Co^{2+} ions [73]. This is superimposed on the broad negative signal from metallic cobalt embedded in ZnO [3,72]. The MCD signal from metallic cobalt nanoparticles is so strong that it dominates the spectrum even where there are other, larger, contributions to the total magnetisation. The negative signal of the presence of metallic Co nanoparticles is dominating the spectrum at 2.5eV which is similar to that already seen by others [72,74,75]. The magnitude of this signal is plotted in the inset to Fig 6.14 as a function of the fraction of the Co ions that were found to be in a metallic environment by XANES. The observed linear dependence confirms that this signal from the metallic is dominant as expected.

The MCD spectra of the films that were grown in an oxygen-rich environment are very different because they did not include a signal from metallic cobalt. Fig 6.15 (a) shows the MCD spectrum for the films grown with metallic cobalt as the precursor. Previous work on the MCD in which the sample had a spin polarised donor band had given a negative signal [18]. The films were grown at base pressure and have a negative value as metallic cobalt gives a negative signal, whereas all the films made of higher oxygen pressures have replaced the negative value by a positive one as no metallic Co was detected. The positive sign observed here indicates that the transition is from a partially occupied spin polarised *acceptor* band.

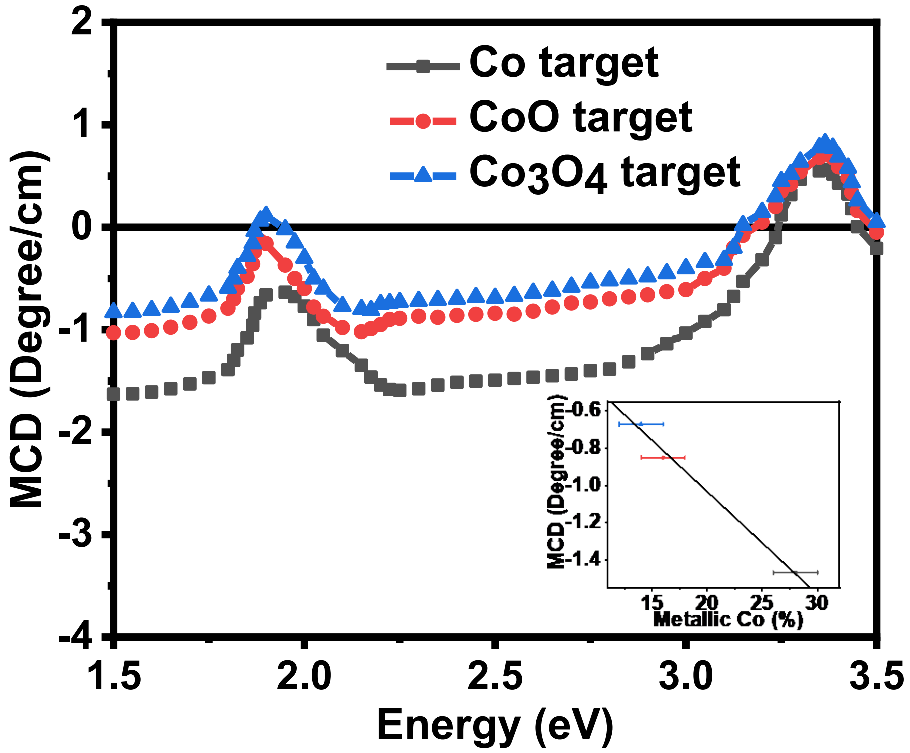

Figure 6.14: The MCD of the films grown at base pressure showing the negative broad signal of the metallic cobalt nanoparticles; the inset shows a plot of the magnitude of the MCD at 2.5eV plotted as a function of the fraction of the Co atoms in a metallic environment as estimated by XANES.

The films grown at the highest oxygen pressure of 1×10^{-1} Torr had the largest grains thus the positive signal at 2.5eV could not have arisen from grain boundaries, nor could it come from oxygen vacancies which would give a negative signal [76]. Such a positive signal is expected from Zn vacancies, which are deep acceptors, to correspond with that seen in photoluminescence [5,56]. The electronic state due to Zn vacancies has been reported to be ~ 2.6 eV below the conduction band, and hence the MCD signal arises when the single electron vacancy state is excited to the conduction band. The density of Zn vacancies is expected to increase as the oxygen pressure is increased. The last noticeable signal is a sharp negative dip at E > 3.3 eV near the band edge, which is due to a split conduction band, where the effect is strongly enhanced if there are some occupied states in the conduction band [5,9,18].

The magnitude of the MCD spectra at 2.5eV for all the films made from T_1, T_2, and T_3 is shown in Fig 6.15 (b). There is a similarity between the dependence of the magnetisation measured at room temperature at oxygen pressure with values greater than 10^{-4} Torr as shown in Fig 6.13 (b) and the MCD shown in Fig 6.15 (b) on the oxygen pressure.

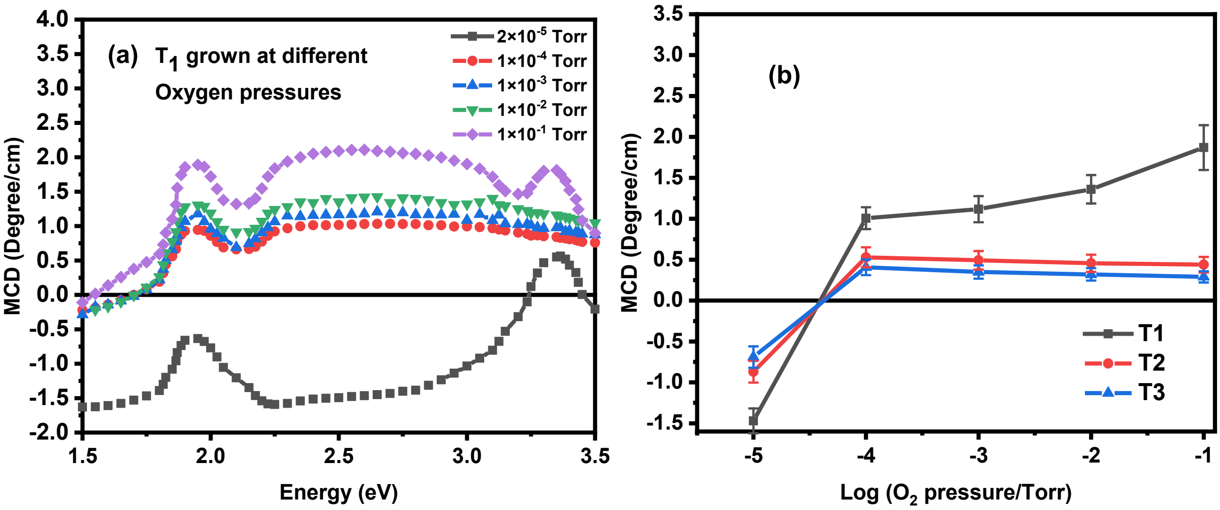

Figure 6.15: (**a**) The MCD spectra for the samples grown with the Co precursor for different amounts of oxygen in the PLD chamber (**b**) the MCD signal intensity at 2.5eV for all the samples plotted as a function of oxygen pressure, the negative signal from metallic cobalt is only seen at base pressure.

The results obtained demonstrate that, for the targets T_2 and T_3, the effect of having extra oxygen from the T_3 precursor, has added to the effect of adding oxygen in the PLD chamber as might have been expected from the similar work by Hasan *et al* [63]. This study investigated the magnetic property of Fe-doped In_2O_3 films by PLD as a function of oxygen pressures. Targets with a fixed concentration of iron are fabricated from indium oxide and iron metal or one of the oxides of iron, FeO, Fe_3O_4 and Fe_2O_3. It was found that when the amount of the oxygen was increased, the number of defect phases and the saturation magnetisation was reduced [63]. In our study, the effect was seen clearly in measurements of both the lattice constant and the saturation magnetisation. The effects of adding oxygen have been to reduce the fraction of oxygen vacancies and it was this that caused the lattice constant to increase and the magnetisation to fall. It seemed surprising that the effects of the precursor in the targets should be so important even though the constituent powders were ground and sintered in air prior to being compressed into targets. The results obtained from T_1 were dramatically different compared to T_2 and T_3 in spite of the fact that there were very little differences in the properties of the targets.

6.5 Conclusion

In this chapter, the investigation of the structural, magnetic, and magneto-optic properties of 5% Co-doped ZnO thin films made with either metallic Co, CoO or Co_3O_4 precursors are described. All the films have been prepared by PLD. The work aims to extend that was done by Ying *et al* [5], where all of the thicknesses in this study were kept constant to avoid any dependence of the magnetic properties on thickness. Also, additional films were produced from metallic Co, CoO or Co_3O_4 precursor targets at a wider range of oxygen pressures in order to compare them with each other and to have a complete study of the magnetic circular dichroism (MCD).

The measurements taken here indicate some of the subtleties of the PLD process. The physical properties and the magnetisation of the films depended on the precursor cobalt material used with ZnO to make the target. This occurred in spite of the fact that there was no evidence for either of the oxide precursors, CoO and Co_3O_4, in the films and no evidence of metallic cobalt in any of the films, including the one made with metallic Co on the target, provided that they were ablated in oxygen pressure of 10^{-4} Torr or higher. In addition, the magnetic properties of the targets were similar, but the films made of these targets and under similar conditions were different. The magnetic susceptibility of the powders taken from the bulk targets, which were annealed at 600° C for 6 hours in air, were increased slightly. This must have been a surface effect since the whole target had previously been sintered at 1,000° C for 12 hours during fabrication. However, the effect of the exposure of the target powders to air during the annealing did not affect the target material in a way that bore any relation to the effects of adding small quantities of oxygen to the PLD chamber.

Any intrinsic magnetism that is observed in ZnCoO occurs due to the presence of Co ions and defects. Native defects that are discussed most widely in the context of magnetism are O and Zn vacancies. Their properties have been studied extensively [77] and briefly in Subsection 2.7.5. In this chapter, it has been shown that the defects occurring in both oxygen-poor and oxygen-rich samples give rise to magnetic properties for ZnCoO but that the type of defect magnetism observed is highly depended on the precursor used to fabricate the target. In both cases, there is some evidence supporting the view that the magnetisation is due to correlated electrons in narrow defect bands rather than local moments associated with the Co or other defects. Furthermore, the type of defect in the films depends in a subtle way on the preparation of the target used for the PLD. A possible reason for the different behaviour of the films is that it is more likely that Co-O ion pairs are present in the laser-plumes of targets made from the oxides CoO and Co_3O_4, rather than for the films ablated from the Co target, where single ions of Co, Zn and O predominated.

This anomalous magnetic and structural behaviour was seen for films made from metallic Co-doped ZnO target and was highly unusual since such behaviour did not occur for a target made from metallic Fe (iron)-doped In_2O_3 [63]. It is sensible then to conclude that this is related to the fact that pure ZnO is unique among the oxides in becoming magnetic when it is grown either oxygen-rich or oxygen-poor.

Our work shows that there are considerable advantages in using metallic Co as the precursor in targets to be used for the fabrication of ZnCoO films by PLD. The role of the Co precursor is to facilitate the production of a narrow defect band based on Zn vacancies in films that were ablated in an oxygen atmosphere.

6.6 References

[1] M. Ivill, S. Pearton, S. Rawal, L. Leu, P. Sadik, R. Das, A. Hebard, M. Chisholm, J. Budai, and D. Norton, *New Journal of Physics* **10**, 10 (2008).

[2] X. Xu, H. Blythe, M. Ziese, A. Behan, J. Neal, A. Mokhtari, R. Ibrahim, M. Fox, and G. Gehring, *New Journal of Physics* **8**, 135 (2006).

[3] Q. Feng, W. Dizayee, X. Li, D. Score, J. Neal, A. Behan, A. Mokhtari, M. Alshammari, M. Al-Qahtani, H. Blythe, R. Chantrell, S. Heald, X. Xu, M. Fox, and G. Gehring, *New Journal of Physics* **18**, 113040 (2016).

[4] E. Bellingeri, S. Rusponi, A. Lehnert, H. Brune, F. Nolting, A. Leveratto, A. Plaza, and D. Marre, *Scientific Reports* **9**, 149 (2019).

[5] M. Ying, H. Blythe, W. Dizayee, S. Heald, F. Gerriu, A. Fox, and G. Gehring, *Applied Physics Letters* **109**, 5, 072403 (2016).

[6] T. Dietl, H. Ohno, F. Matsukura, J. Cibert, and D. Ferrand, *Science* **287**, 1019 (2000).

[7] K. Sato and H. Katayama-Yoshida, J*apanese Journal of Applied Physics Part 2-Letters* **39**, L555 (2000).

[8] Q. Wang, Q. Sun, G. Chen, Y. Kawazoe, and P. Jena, *Physical Review B* **77** (2008).

[9] A. Behan, A. Mokhtari, H. Blythe, D. Score, X. Xu, J. Neal, M. Fox, and G. Gehring, *Physical Review Letters* **100**, 047206 (2008).

[10] R. Janisch, P. Gopal, and N. A. Spaldin, *Journal of Physics-Condensed Matter* **17**, R657 (2005).

[11] C. Song, F. Zeng, K. W. Geng, X. J. Liu, F. Pan, B. He, and W. S. Yan, *Physical Review* B **76** (2007).

[12] X. Liu, S. Bao, H. Zhang, C. Ma, X. Xu, and Q. Zhang, *Journal of Inorganic Materials* **27**, 369 (2012).

[13] H. Lee, S. Jeong, C. Cho, and C. Park, *Applied Physics Letters* **81**, 4020 (2002).

[14] M. Patra, K. Manzoor, M. Manoth, S. Vadera, and N. Kumar, J*ournal of Physics and Chemistry of Solids* **70**, 659 (2009).

[15] S. Kumar, S. Basu, B. Rana, A. Barman, S. Chatterjee, S. N. Jha, D. Bhattacharyya, N. Sahoo, and A. Ghosh, *Journal of Materials Chemistry* C **2**, 481 (2014).

[16] J. MacManus-Driscoll, N. Khare, Y. Liu, and M. Vickers, *Advanced Materials* **19**, 2925 (2007).

[17] S. Guner, O. Gurbuz, S. Caliskan, V. Nuzhdin, R. Khaibullin, M. Ozturk, and N. Akdogan, *Applied Surface Science* **310**, 235 (2014).

[18] J. Neal, A. Behan, R. Ibrahim, H. Blythe, M. Ziese, M. Fox, and G. Gehring, *Physical Review Letters* **96**, 4, 197208 (2006).

[19] J. Chen, M. Yu, W. Zhou, K. Sun, and L. Wang, *Applied Physics Letters* **87**, 173119 (2005).

[20] S. Yang, A. Pakhomov, S. Hung, and C. Wong, *Ieee Transactions on Magnetics* **38**, 2877 (2002).

[21] Z. Lu, H. Hsu, Y. Tzeng, F. Zhang, Y. Du, and J. C. Huang, *Applied Physics Letters* **95**, 102501 (2009).

[22] T. Dietl, T. Andrearczyk, A. Lipinska, M. Kiecana, M. Tay, and Y. H. Wu, *Physical Review B* **76**, 5, 155312 (2007).

[23] M. Gacic, G. Jakob, C. Herbort, H. Adrian, T. Tietze, S. Brueck, and E. Goering, *Physical Review B* **75**, 205206 (2007).

[24] L. Li, Y. Guo, X. Cui, R. Zheng, K. Ohtani, C. Kong, A. Ceguerra, M. Moody, J. Ye, H. Tan, C. Jagadish, H. Liu, C. Stampfl, H. Ohno, S. Ringer, and F. Matsukura, *Physical Review* B **85**, 174430 (2012).

[25] A. Ney, V. Ney, S. Ye, K. Ollefs, T. Kammermeier, T. C. Kaspar, S. A. Chambers, F. Wilhelm, and A. Rogalev, *Physical Review B* **82**, 041202 (2010).

[26] Q. Wang, J. Wang, X. L.Zhong, Q. Tan, Z. Hu, and Y. Zhou, *Applied Physics Letters* **100**, 132407 (2012).

[27] H. Lee, H. Nam, Y. Cho, S. Kim, C. H. Park, C. Cho, and S. Jeong, *Epl* **78**, 4, 17001 (2007).

[28] J. Kim, H. Kim, D. Kim, Y. Ihm, and W. Choo, J*ournal of Applied Physics* **92**, 6066 (2002).

[29] A. Aravind, K. Hasna, M. Jayaraj, M. Kumar, and R. Chandra, *Applied Physics Materials Science & Processing* **115**, 843 (2014).

[30] N. Akdogan, A. Nefedov, K. Westerholt, H. Zabel, H.-W. Becker, C. Somsen, R. Khaibullin, and L. Tagirov, *Journal of Physics D-Applied Physics* **41**, 165001 (2008).

[31] S. Guo and Z. Du, *Journal of Magnetism and Magnetic Materials* **324**, 782 (2012).

[32] F. Pan, C. Song, X. Liu, Y. Yang, and F. Zeng, *Materials Science & Engineering R-Reports* **62**, 1 (2008).

[33] S. Chen, H. Xu, S. Wang, and K. Suzuki, *Integrated Ferroelectrics* **144**, 1 (2013).

[34] H. Hsu, J. Huang, Y. Huang, Y. Liao, M. Lin, C. Lee, J. Lee, S. Chen, L. Lai, and C. Liu, *Applied Physics Letters* **88**, 242507 (2006).

[35] S. Pearton, W. Heo, M. Ivill, D. Norton, and T. Steiner, *Semiconductor Science and Technology* **19**, R59 (2004).

[36] C. Fitzgerald, M. Venkatesan, J. Lunney, L. Dorneles, and J. Coey, *Applied Surface Science* **247**, 493 (2005).

[37] A. Behan, "*Characterisation of doped ZnO thin films for spintronic applications*", PhD thesis, University of Sheffield, (2008).

[38] T. Dietl, *Nature Materials* **9**, 965 (2010).

[39] Z. Kayani, R. Ishaque, B. Zulfiqar, S. Riaz, and S. Naseem, *Optical and Quantum Electronics* **49**, 223 (2017).

[40] S. Ogale, *Advanced Materials* **22**, 3125 (2010).

[41] S. Heald, T. Kaspar, T. Droubay, V. Shutthanandan, S. Chambers, A. Mokhtari, A. Behan, H. Blythe, J. Neal, M. Fox, and G. Gehring, *Physical Review B* **79**, 11, 075202 (2009).

[42] T. Kaspar, T. Droubay, S. Heald, M. Engelhard, P. Nachimuthu, and S. Chambers, *Physical Review B* **77**, 201303 (2008).

[43] N. Spaldin, *Physical Review B* **69**, 125201 (2004).

[44] K. Sato and H. Katayama-Yoshida, *Japanese Journal of Applied Physics Part 2-Letters* **40**, L334 (2001).

[45] T. Tietze, M. Gacic, G. Schuetz, G. Jakob, S. Brueck, and E. Goering, *New Journal of Physics* **10**, 055009 (2008).

[46] S. Yin, M. Xu, L. Yang, J. Liu, H. Rosner, H. Hahn, H. Gleiter, D. Schild, S. Doyle, T. Liu, T. Hu, E. Muromachi, and J. Jiang, *Physical Review* B **73**, 224408 (2006).

[47] Q. Xu, L. Hartmann, H. Schmidt, H. Hochmuth, M. Lorenz, R. Schmidt-Grund, C. Sturm, D. Spemann, and M. Grundmann, *Physical Review* B **73**, 205342 (2006).

[48] K. Ueda, H. Tabata, and T. Kawai, *Applied Physics Letters* **79**, 988 (2001).

[49] Z. Lu, W. Miao, W. Zou, M. Xu, and F. Zhang, *Journal of Alloys and Compounds* **494**, 392 (2010).

[50] Z. Quan, X. Zhang, W. Liu, X. Li, K. Addison, G. Gehring, and X. Xu, *Acs Applied Materials & Interfaces* **5**, 3607 (2013).

[51] H. Bardeleben, N. Jedrecy, and J. Cantin, *Applied Physics Letters* **93**, 142505 (2008).

[52] Y. Shapira and V. Bindilatti, *Journal of Applied Physics* **92**, 4155 (2002).

[53] M. Opel, K. Nielsen, S. Bauer, S. Goennenwein, J. Cezar, D. Schmeisser, J. Simon, W. Mader, and R. Gross, *European Physical Journal* B **63**, 437 (2008).

[54] T. Kaspar, T. Droubay, S. Heald, P. Nachimuthu, C. Wang, V. Shutthanandan, C. A. Johnson, D. Gamelin, and S. Chambers, *New Journal of Physics* **10**, 055010 (2008).

[55] A. Barla, G. Schmerber, E. Beaurepaire, A. Dinia, H. Bieber, S. Colis, F. Scheurer, J. Kappler, P. Imperia, F. Nolting, F. Wilhelm, A. Rogalev, D. Mueller, and J. Grob, *Physical Review B* **76**, 125201 (2007).

[56] G. Xing, Y. Lu, Y. Tian, J. Yi, C. Lim, Y. Li, G. Li, D. Wang, B. Yao, J. Ding, Y. Feng, and T. Wu, *Aip Advances* **1**, 022152 (2011).

[57] M. Kapilashrami, J. Xu, V. Ström, K. Rao, and L. Belova, *Applied Physics Letters* **95**, 033104 (2009).

[58] M. Ying, A. M. A. Saeedi, M. Yuan, X. Zhang, B. Liao, X. Zhang, Z. Mei, X. Du, S. Heald, and M. Fox and G. Gehring, *Journal of Materials Chemistry C* **7**, 1138 (2019).

[59] A. Tuan, J. Bryan, A. Pakhomov, V. Shutthanandan, S. Thevuthasan, D. McCready, D. Gaspar, M. Engelhard, J. Rogers, K. Krishnan, D. Gamelin, and S. Chambers, *Physical Review* B **70**, 054424 (2004).

[60] U. Ozgur, Y. Alivov, C. Liu, A. Teke, M. A. Reshchikov, S. Dogan, V. Avrutin, S. Cho, and H. Morkoc, *Journal of Applied Physics* **98**, 041301 (2005).

[61] J. Lee, G. Xing, J. Yi, T. Chen, M. Ionescu, and S. Li, *Applied Physics Letters* **104**, 012405 (2014).

[62] M. Venkatesan, C. Fitzgerald, J. Lunney, and J. Coey, *Physical Review Letters* **93**, 177206 (2004).

[63] H. Albargi, M. Alshammari, K. Museery, S. Heald, F. Jiang, A. M. A. Saeedi, A. M. Fox, and G. Gehring, *Coatings* **9**, 381 (2019).

[64] B. Straumal, A. Mazilkin, S. Protasova, P. Straumal, A. Myatiev, G. Schutz, E. Goering, T. Tietze, and B. Baretzky, *Philosophical Magazine* **93**, 1371 (2013).

[65] B. Ravel and M. Newville, *Journal of Synchrotron Radiation* **12**, 537 (2005).

[66] N. Fontaina-Troitino, S. Liebana-Vinas, B. Rodriguez-Gonzalez, Z. A. Li, M. Spasova, M. Farle, and V. Salgueirino, *Nano Letters* **14**, 640 (2014).

[67] I. Djerdj, Z. Jaglicic, D. Arcon, and M. Niederberger, *Nanoscale* **2**, 1096 (2010).

[68] C. Kittel, *Introduction to solid state physics* (Wiley, Hoboken, NJ, 2005).

[69] M. Kobayashi, Y. Ishida, J. Hwang, T. Mizokawa, A. Fujimori, K. Mamiya, J. Okamoto, Y. Takeda, T. Okane, Y. Saitoh, Y. Muramatsu, A. Tanaka, H. Saeki, H. Tabata, and T. Kawai, *Physical Review* B **72**, 201201 (2005).

[70] J. Furdyna, *Journal of Applied Physics* **64**, R29 (1988).

[71] S. Zhou, K. Potzger, J. von Borany, R. Groetzschel, W. Skorupa, M. Helm, and J. Fassbender, *Physical Review* B **77**, 035209 (2008).

[72] D. Score, M. Alshammari, Q. Feng, H. Blythe, M. Fox, G. Gehring, Z. Quan, X. Li, and X. Xu, in *International Conference on Magnetism (ICM 2009)* Karlsruhe, Germany, 2009).

[73] K. Kittilstved, J. Zhao, W. Liu, J. Bryan, D. Schwartz, and D. Gamelin, *Applied Physics* Letters **89**, 062510 (2006).

[74] C. Clavero, G. Armelles, J. Margueritat, J. Gonzalo, M. Garcia del Muro, A. Labarta, and X. Batlle, *Applied Physics Letters* **90**, 182506 (2007).

[75] Y. Fukuma, H. Asada, J. Yamamoto, F. Odawara, and T. Koyanagi, *Applied Physics Letters* **93**, 142510 (2008).

[76] M. Ying, W. Dizayee, Z. Mei, X. Du, M. Fox, and G. Gehring, *Journal of Physics D-Applied Physics* **48**, 255502 (2015).

[77] A. Janotti and C. Van de Walle, *Physical Review B* **76**, 22, 165202 (2007).

Chapter 7 **Conclusion and Future Work**

In this chapter, we first summarise the most important results from Chapters 4, 5 and 6 and draw conclusions from all the studies taken together, for different DMS materials. Secondly, some potential future extensions of the work undertaken so far will be outlined.

7.1 Conclusions

The research described in this thesis has been concerned specifically with different DMS materials, in order to improve and understand the origin of RTFM. In this work, the structural, magnetic and magneto-optical properties of ZnO thin films were investigated when doped with different materials involving non-TM, TM and RE dopants such as Kr, Co and Eu respectively. The magnetic properties of the materials that were investigated throughout this thesis have revealed that such properties are sensitively affected by different parameters. We have found that ZnO is an important candidate for d^0 DMS. Particularly, O-polar thin films play an important role in producing defects that facilitate large magnetism after being implanted with either TM or Non TM materials. The magnetisation of Co-doped ZnO thin films however, have been found to be advantageous because of the large magnetisation produced. Particularly when the films are produced via PLD with metallic Co as a precursor at different oxygen pressures.

The effects of Kr-doping in ZnO, using the ion implantation method on the structural and magnetic properties were studied. Two different sets of samples, wafers and thin films, were prepared. Both samples had one O-polar and one Zn-polar face, to compare the difference of polarity on the resulting magnetisation. The wafers were outsourced and the thin films were produced *via* MBE and were deposited on a sapphire substrate. The Kr-doped ZnO O-polar thin films, among the rest of the Kr-doped ZnO Zn-polar films and both O and Zn-polar wafers, exhibit large magnetisation at room temperature. The largest magnetisation of 185 emu cm^{-3}, corresponded to a moment of ~ 40 Bohr magnetons per implanted Kr ion and was found for the highest Kr doping concentration. This observation is higher than the previous work of As-doped ZnO thin films, produced by ion implantation, by Ying *et al* [8]. No magnetism was observed for concentrations below 5×10^{19} cm^{-3}.

We have shown that the Kr-doped ZnO O-polar films have an increased lattice spacing accompanied by a decreased grain size, using XRD and EXAFS measurements, which indicates that full inclusion of the Kr atoms into the lattice had been achieved. This means that a large amount of Kr was ultimately implanted into the grain and this led to an increased sample volume taken up by the grain boundaries. However, in the case of the Kr-doped ZnO Zn-polar film, there was almost no change to the lattice spacing nor the grain size after being implanted, which suggested that the vast majority of Kr atoms would be found in art the boundary of the grains.

Raman spectra revealed a strong scattering in the O-polar films originating from the grain boundaries, this indicated that the films are inherently susceptible to the formation of amorphous regions [1], which can be linked to strongly magnetic grain boundaries. On the other hand, the Zn-polar, which was non magnetic, the film presents a strong case for scattering due to point defects.

This work clearly demonstrates how the resulting magnetism is strongly influenced by the boundary region and the grain surface ultimately produced there. Magnetism was found not to result from the surface of nanoparticles and the Raman spectra obtained did not correspond to that usually found for implanted crystals [2]. In our case, the RTFM observed was due to grain boundaries caused by ion implantation and is much larger than that of previous studies [3-5]. In conclusion, defective O-polar ZnO thin films, produced by ion implantation, have the capability to exhibit large magnetisation.

The structural and magnetic properties of Co, Eu mono-doped and codoped ZnO thin films that were prepared by ion implantation, were investigated. ZnO thin films were deposited on the sapphire substrate by PLD. The films were found to be O-polar and two main results were obtained. The first result, derived from both structural and magnetic properties of implanted films without annealing, shows that ion implantation plays an important role in the production of defects, which cause large magnetism in the films. The magnetisation value observed for the ZnCoO thin film was 60 emu cm^{-3}, which is equivalent to 3.9 μ_B/Co and is much larger than that attributed to either metallic Co or Co^{2+}. This is in good agreement with the previous finding of Kr-doped ZnO O-polar films.

The second result illustrates that implanted films are sensitive to annealing temperature and environment. Annealing at 600° C in vacuum leads to an enormous increase of metallic Co in the films and the observed magnetisation was subsequently dominated by the metallic Co, which is useless in application. However, annealing the films at 600° C in air leads to an almost full recovery of the damaged region created during ion implantation and no metallic Co. After annealing at several different temperatures, we found that the minimum temperature treatment required to recover the damaged region and eliminate the metallic Co introduced during implantation, was 600°C in air for one hour. This was supported by Raman spectroscopy measurements that showed the crystal structures of the films were recovered as well as the XANES measurements which showed no detection of metallic Co. The magnetisation found for ZnCoEuO was less than to the sum of that observed feromagentism in ZnCoO and ZnEuO films, which shows there is no interaction between Co (3*d*) and Eu (4*f*) as it Lee *et al* suggested [6].

Co-doped ZnO thin films were deposited by PLD from three different targets: metallic Co, CoO, and Co_3O_4. The films produced from these different targets were grown at several different oxygen pressures; at a base pressure of 2×10^{-5} and four additional higher oxygen pressures of 1×10^{-4}, 1×10^{-3}, 1×10^{-2}, and 1×10^{-1} Torr. The structural, magnetic, and magneto-optic properties on these films were investigated. The subtleties of the PLD process are revealed by the measured structural and magnetic properties. These properties were dependent on the Co precursor material doped into ZnO when making the target. This result occurred even though there was no detection of any of the oxide precursors, CoO and Co_3O_4. There is also no detection of metallic Co in the films when produced at an oxygen pressure of 10^{-4} Torr or higher. Furthermore, the magnetic properties of the targets were almost the same, however, the magnetic properties of the films show very different behaviours. The measured susceptibility of the targets (powders) show a small increase after annealing at 600° C for 1 hour in air. This can be attributed to the surface effect because the target had been already annealed at 1,000° C in air for 12 hours during fabrication. Nevertheless, the effect of exposing the target powders to air later had a small effect on the target material and could not be related in the same way to adding small quantities of oxygen to the PLD chamber.

It was found that the observed results for the films made of CoO and Co_3O_4 targets differed little. The Co_3O_4 precursor compounded the effect of adding oxygen in the PLD chamber as seen in previous studies in In_2O_3 [7] and can be seen clearly in measurements of the lattice constant and saturation magnetisation. Additional oxygen caused a reduction in the number of oxygen vacancies leading to an increase in the lattice constant and decrease in magnetisation. The results for the metallic Co precursor are in stark contrast to both films produced from CoO and Co_3O_4 targets, as seen in previous works [8]. It is therefore surprising that the precursor in the target should have such a large impact, even though the constituent powders were ground and sintered in air prior to compression into the targets.

The structural and magnetic properties of the films made of different precursors have similar behaviour. Firstly, they all only contain metallic Co at base pressure and this metallic Co disappears at high oxygen pressure. Secondly, the grain size increases with increasing oxygen pressure and finally the magnetic properties of the targets are almost the same before annealing and after annealing at 600 ° C in air.

However, the structural and magnetic properties of the films made of different precursors have contrasting behaviour. Firstly, the *c* lattice constant, corresponding to the films made from the metallic cobalt target decreased with increasing oxygen pressure but the *c* lattice constant, corresponding to the films made from CoO and Co_3O_4 targets, increased with increasing the oxygen pressure. Secondly, the magnetism increases proportionally with increasing oxygen pressure for the films made from metallic cobalt target but the magnetisation decreases with increasing oxygen pressure for films grown from CoO and Co_3O_4 targets.

The magnetisation observed in Co-doped ZnO thin films made by PLD arises due to the type of defects, O or Zn vacancies, which depend subtly on the way the target is prepared. This could be due to the increased likelihood of Co-O ion pairs present in the laser plume for targets containing oxides (CoO and Co_3O_4) in comparison to those films ablated from Co targets, where single Co, Zn and O ions predominate. The observed structural and magnetic properties from the films made of Co targets was not seen for the films made of metallic Fe targets in In_2O_3 [7]. We believe that this might be due to undoped ZnO, which is unique among TMOs in that it is magnetic when produced at high or low oxygen pressures.

7.2 Future work

Whilst studying the effects of doping in ZnO thin films undertaken in this thesis, we found that the magnetic, magneto-optical and structural properties are sensitive to the growth techniques used, such as ion implantation and PLD, and conditions under which the films are grown, examples include the dopant concentration, oxygen pressures, polarity of the ZnO films and post annealing treatment. The previous works report that, for both doped and undoped ZnO thin films, their behaviour is affected by several additional growth techniques and conditions including MBE, Sol gel and substrate temperature and the environment in which they are grown [1,8-15].

The results from Kr-doped ZnO samples demonstrate the importance of the polarity of ZnO thin films, on the resulting magnetisation since the O-polar face is more likely to exhibit large magnetisation after implantation due to defects. Other interesting findings by Xu *et al* [13] showed that adding Al in ZnCoO and ZnMgO thin films enhanced the magnetisation greatly. It would, therefore, be beneficial to investigate the effects of Kr-doped ZnO O-polar thin films with additional Al. We would suggest differing concentrations of Kr and only 1% of Al in order to prevent the breakup of the crystal structure of ZnO resulting from Al. We could then investigate the structural and magnetic properties and ultimately whether Al would enhance the magnetisation for this system.

The results from Co-doped ZnO thin films demonstrate that the magnetisation increases with increasing oxygen pressure, up to 100 mTorr, for films made from Co targets doped into ZnO *via* PLD. It would be useful to make different films from the same target but with even higher oxygen pressures of 200, 300, 400, and 500 mTorr and to investigate the structural and magnetic properties for these films.

The main difficulty of DMSs, specifically for ZnO doped with TMs, is the reproducibility of growth samples between labs. It is not necessarily guaranteed that the same properties will be reproduced under the same growth conditions. A huge number of parameters have been investigated, including a variety of TM dopants, different compositions, preparation techniques and growth conditions and post-growth processing. These issues surrounding reproducibility are likely due to insufficient characterisation, the different growth techniques involved and the lack of a clear description of the sample preparation process. We suggest that other researchers pay attention to these issues with the aim of achieving better reproducibility and subsequently an improved understanding of how ferromagnetism originates DMSs.

7.3 References

[1] M. Ying, A. M. A. Saeedi, M.Yuan, X. Zhang, B.Liao, X. Zhang, Z. Mei, X. Du, S. Heald, and M. Fox and G. Gehring, *Journal of Materials Chemistry C* **7**, 1138 (2019).

[2] P. Chand, A. Gaur, and A. Kumar, *Journal of Alloys and Compounds* **539**, 174 (2012).

[3] B. Straumal, S. G. Protasova, A. Mazilkin, E. Goering, G. Schutz, P. Straumal, and B. Baretzky, *Beilstein Journal of Nanotechnology* **7**, 1936 (2016).

[4] T. Tietze, P. Audehm, Y. Chen, G. Schuetz, B. Straumal, S. Protasova, A. Mazilkin, P. Straumal, T. Prokscha, H. Luetkens, Z. Salman, A. Suter, B. Baretzky, K. Fink, W. Wenzel, D. Danilov, and E. Goering, *Scientific Reports* **5**, 8871 (2015).

[5] B. Straumal, A. Mazilkin, S. Protasova, A. Myatiev, P. Straumal, G. Schutz, P. van Aken, E. Goering, and B. Baretzky, *Physical Review B* **79**, 205206 (2009).

[6] J. Lee, G. Xing, J. Yi, T. Chen, M. Ionescu, and S. Li, *Applied Physics Letters* **104**, 012405 (2014).

[7] H. Albargi, M. Alshammari, K. Museery, S. Heald, F. Jiang, A. M. A. Saeedi, M. Fox, and G. Gehring, *Coatings* **9**, 381 (2019).

[8] M. Ying, H. Blythe, W. Dizayee, S. Heald, F. Gerriu, M. Fox, and G. Gehring, *Applied Physics Letters* **109**, 5, 072403 (2016).

[9] M. Ying, S. Wang, T. Duan, B. Liao, X. Zhang, Z. Mei, X. Du, F. Gerriu, M. Fox, and G. Gehring, *Materials Letters* **171**, 121 (2016).

[10] M. Yuan, X. Zhang, A. M. A. Saeedi, W. Cheng, C. Guo, B. Liao, X. Zhang, M. Ying, and G. Gehring, *Nuclear Inst. and Methods in Physics Research*, B **455**, 7 (2019).

[11] S. Zhou, K. Potzger, Q. Xu, G. Talut, M. Lorenz, W. Skorupa, M. Helm, J. Fassbender, M. Grundmann, and H. Schmidt, *Vacuum* **83**, S13 (2009).

[12] N. Hong, J. Sakai, N. Poirot, and V. Brize, *Physical Review B* **73**, 132404 (2006).

[13] X. Xu, H. Blythe, M. Ziese, A. Behan, J. Neal, A. Mokhtari, R. Ibrahim, M. Fox, and G. Gehring, *New Journal of Physics* **8**, 135 (2006).

[14] S. Mal, T. Yang, C. Jin, S. Nori, J. Narayan, and J. T. Prater, *Scripta Materialia* **65**, 1061 (2011).

[15] S. Aravindh, U. Schwingenschlogl, and I. Roqan, *Journal of Chemical Physics* **143**, 224703 (2015).